INTERNATIONAL ATOMIC ENERGY AGENCY
UNITED NATIONS EDUCATIONAL, SCIENTIFIC AND CULTURAL ORGANIZATION

INTERNATIONAL CENTRE FOR THEORETICAL PHYSICS
34100 TRIESTE (ITALY) - P.O.B. 586 - MIRAMARE - STRADA COSTIERA 11 - TELEPHONE: 2240-1
CABLE: CENTRATOM - TELEX 460392-I

SMR/208 - 11

SPRING COLLEGE IN MATERIALS SCIENCE

ON

"METALLIC MATERIALS"

(11 May - 19 June 1987)

DISLOCATIONS

J.Th.M. DE HOSSON
Department of Applied Physics
University of East Anglia
Norwich NR4 7TJ
U.K.

CHAPTER 32

Dislocations in Solids Investigated by means of Nuclear Magnetic Resonance

J. Th. M. De HOSSON

Department of Applied Physics, Materials Science Centre
University of Groningen
9747 AG Groningen, The Netherlands

O. KANERT

Institute of Physics
University of Dortmund
46 Dortmund 50, FRG

and

A. W. SLEESWYK

Physical Laboratory
University of Groningen
9718 CM Groningen, The Netherlands

Dislocations in Solids
Edited by F. R. N. Nabarro

Contents

1. Introduction

When in 1934 Orowan [1], Polanyi [2] and Taylor [3] independently introduced the concept of a dislocation as a lattice defect moving under relatively low stress ($\sim E/1000$), it remained only a theoretical construction for some two decades. There were no experimental methods available at that time for observing and studying the physical properties of dislocations, or even for proving their existence.

In the past three decades, research workers were able to observe and to study dislocations by a number of techniques. Hedges and Mitchell [4] introduced a decorating technique to make dislocations visible in silver halide crystals. The etch-pit technique was explored by Gilman and Johnston [5]. Transmission electron microscopy was used first by Hirsch et al. [6] and by Bollman [7] for studying dislocations, a technique that is now commonly used for observing dislocations. However, either these require transparency of the crystals studied and immobile dislocations, or they allow only investigation of dislocations near free surfaces, where the existence of image forces may cause their behaviour to be very different from that in the interior of the material. These drawbacks make it especially difficult to interpret the results of experimental dislocation studies in terms of plasticity of solids, and there is consequently a real need for techniques of investigating dislocations and their movement which are free of such limitations.

It has been well established that the strengthening of solid materials is brought about by obstructing the movement of dislocations. A description of the dislocation motion on a microscopic scale is essential for the understanding of the macroscopic plasticity of crystals. A few years ago, we showed that pulsed nuclear magnetic resonance is a useful tool to study dislocation motion. The technique and results obtained for alkali halides and polycrystalline metals will be the subject of this chapter. It turned out that three sets of microscopic information about the dislocation motion can be deduced in principle from these pulsed nuclear magnetic resonance experiments: (i) the mean free path of moving dislocations; (ii) the mean time of stay between two consecutive jumps of a mobile dislocation; and (iii) the mobile dislocation density as a fraction of the total dislocation density.

Prior to our investigation, the nuclear magnetic resonance technique had proved to be a means of determining "static" characteristics of defects in solids such as the total dislocation density. Pioneer work was done by Watkins [8] about the effect of dislocations on the nuclear magnetic resonance, but he considered merely the stress field of an edge dislocation and further simplified by assuming that the electric field gradients arise only from the shear strain. His calculation of the angular distribution of dislocation lines and its effects on the broadening of signals of ^{79}Br in K Br is based on the assumption that a crystal is an ideal continuum, neglecting the preferred orientation of a dislocation line. In 1957 the nuclear magnetic resonance of ^{127}I was

investigated by Otsuka and Kawamura [9–11] in plastically deformed crystals of KI. The broadened signals of ^{127}I showed considerable anisotropy with respect to the direction of the external magnetic field. The anisotropy was interpreted as arising both from the specific orientation of a dislocation line in a crystal and from the second-order quadrupole perturbation. The experiments were analyzed in terms of the electric field gradient tensor introduced by Shulman et al. [12], who applied elastic stresses to InSb single crystals to decrease the crystalline symmetry, thereby producing quadrupole broadening of the nuclear magnetic resonance lines. In this chapter, the underlying theory for obtaining total dislocation densities from the resulting quadrupole broadening will also be explained.

The method of obtaining total dislocation densities from quadrupole broadening and that of determining mobile dislocation densities are both essentially based on the interaction between nuclear electric quadrupole moments and electric field gradients at the nucleus. If the nuclear environment is cubically symmetric there does not exist any static electric field gradient at the nucleus and interaction does not appear. However, around a dislocation that symmetry is destroyed and interactions between nuclear electric quadrupole moments and electric field gradients arise. When the condition of nonvanishing electric field gradients is fulfilled, line shapes and splittings of transition frequencies in nuclear magnetic resonance measurements are influenced by the quadrupole interaction. In order to apply the NMR technique to studies on dislocations, it is essential to have atomic nuclei with non-zero quadrupole moments; that requirement limits the choice of materials to be studied.

In moving across the interface between two established fields of science, namely dislocation theory and nuclear magnetic resonance concepts, it was found necessary to limit the discussion to a relatively small number of basic ideas and concepts. Furthermore, we have attempted throughout the treatment to keep it understandable by research workers in both fields. The principal emphasis is on the application of nuclear magnetic resonance as a complementary new technique for the study of dislocations in solids. Of necessity, the treatment is rather brief and does not pretend to completeness; accordingly only a few representative materials are discussed, and an attempt was made to focus on the main features of the NMR picture. It is hoped that this approach will be stimulating to the reader and familiarize him with NMR concepts and ideas about dislocations.

The chapter is divided logically into two parts. The first part of the chapter–sects. 3 and 4 – is devoted to the fundamentals of static quadrupole effects in dislocated solids; the second part is mainly a presentation of experimental results and conclusions. Section 3 treats the electric field gradient tensor and the influence of quadrupolar perturbation, and the effect of the dislocation density on the NMR signal. In sect. 4 attention is given to relaxation theory adapted to dislocation motion and in sect. 5 the nuclear spin relaxation experiments on alkali halide single crystals and on polycrystalline aluminium foils are described. The results of these relaxation measurements as functions of strain rate, strain, compression axis, temperature and impurity content are given in sect. 5. In addition, experiments confirming the validity of the nuclear spin relaxation theory used are presented in this section. Finally, in sect. 6 the limitations of the NMR technique with respect to dislocation dynamics are discussed and a number of new ideas on the application of this technique of investigation will be presented.

2. Dislocations in particular structures

2.1. Dislocations in NaCl-type single crystals

In the chapter by Amelinckx [13] in vol. 2 of this series, a review is given of dislocations and slip in the sodium chloride structure. For the plastic deformation of ionic crystals in general the reader is referred to the book by Sprackling [14]. A concise review will be presented here.

The NaCl structure (Fm3m) can be considered as consisting of two interpenetrating f.c.c. lattices of the two types of atoms. Normally slip takes place on {110} planes in ⟨110⟩ directions, but when the ions are highly polarizable as in PbTe, {001} slip planes are found to predominate [15]. The smallest Burgers vector of a perfect dislocation in this structure is $\frac{1}{2}\langle 110\rangle$. Three low-index planes intersect along the ⟨110⟩ direction: {100}, {110} and {111} (fig. 1). The {100} planes are cleavage planes, although they are observed sometimes to act as slip planes as well. In particular, if {110} has only a very low resolved shear stress acting in its plane, and {100} a relatively high one, it is possible for glide to occur on {100} in the ⟨110⟩ direction [15].

The {111} planes contain ions with charges of the same sign. Therefore, although these planes are close packed, glide on these planes seems less favourable because the extra half plane of an edge dislocation on a {111} plane would end in a row of identical atoms with the same charge. The total line energy of such dislocations would be high, and it is therefore less likely that they occur. The common glide planes are the electrically neutral {110} planes.

Huntington et al. [16, 17] calculated the core energies of dislocations in NaCl

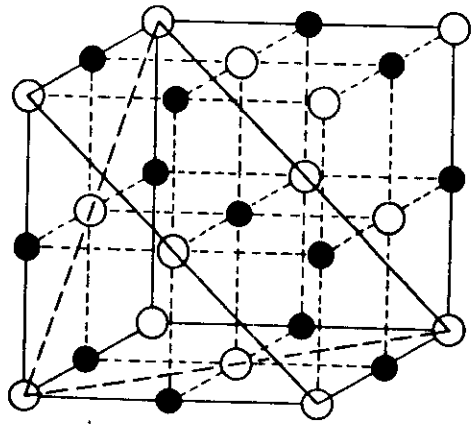

Fig. 1. Unit cell of the Fm3m NaCl structure with {110} and {111} planes indicated.

using a Born model, minimizing the core energies and matching them with the elastic solution at large distances. The core energy of a ⟨110⟩{100} edge dislocation was found to be about three times larger than the core energy of a ⟨110⟩{110} edge dislocation. The core energy of a ⟨110⟩ screw dislocation appeared to be one order of magnitude smaller than that of a ⟨110⟩{100} edge dislocation. Huntington et all. suggested that the Peierls stress is larger than for {100} edge dislocations because of the repulsion between the ions. Therefore it is likely that the glide plane in the NaCl structure is determined by the core structure of the glide dislocations. Similar calculations of the dislocation core energy for NaCl, giving results of the same order of magnitude, have been made by Kurosawa [18], Puls and So [19] and by Granzer et al. [20–22]. The latter applied for the first time nonlinear elasticity theory to atomistic calculations of the core configuration of edge dislocations in NaCl-type crystals. In fig. 2 the atomic configurations of a ⟨110⟩ edge dislocation in NaCl are depicted schematically.

The work-hardening behaviour (increase in resolved shear stress as a function of resolved plastic shear strain) of single crystals of f.c.c. metals and of alkali halides with rocksalt structure show a striking similarity. An example of a stress–strain curve obtained on NaCl compressed along the ⟨100⟩ direction is drawn in fig. 3. Stage I, a region with a low constant work-hardening rate $\theta = (\partial\sigma/\partial\varepsilon)_{\varepsilon,T}$ is followed by stage II with increased constant work-hardening rate. At still higher strains, stage III with a decreasing work-hardening rate appears.

In the past, great attention was paid to the work-hardening mechanism of alkali halides with the rocksalt structure. It has been suggested [20] that the common features of the work-hardening behaviour of single crystals of f.c.c. metals and of

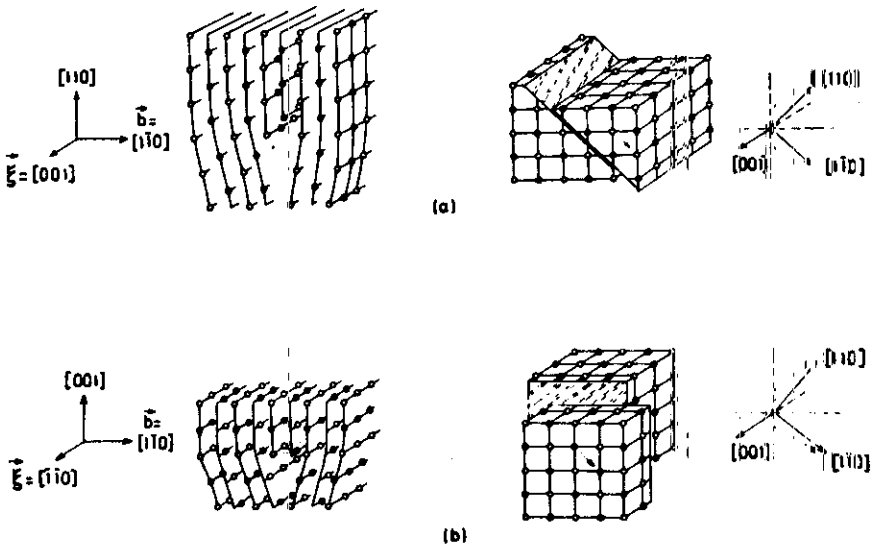

Fig. 2. Dislocations on {110} and {100} glide planes in NaCl and the shear caused by their motion.

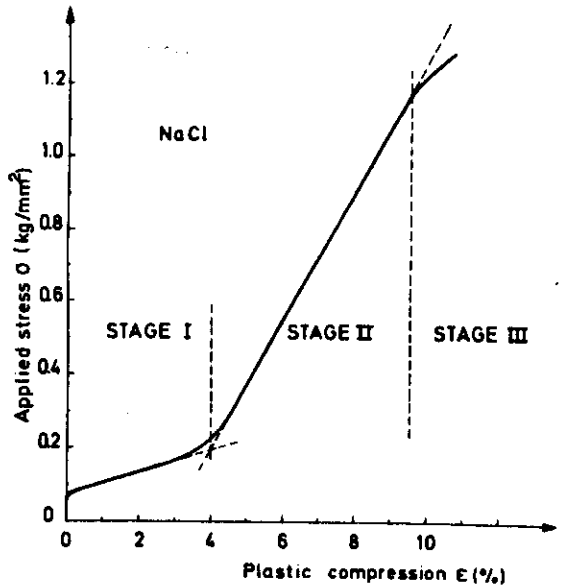

Fig. 3. Stress-strain curve of an NaCl single crystal compressed along the ⟨100⟩ direction [145].

NaCl provide arguments for explanations of the work-hardening curve which are independent of the crystal structure, but that can hardly be correct. In fact, the range of a particular stage and the value of the work-hardening rate are found to depend on a number of parameters such as temperature of testing, strain rate, impurity content and crystal orientation. At present, no well-established complete theory of work-hardening in alkali halide crystals exists. The experimental facts which are established are presented below:

Glide systems. When rocksalt-structured crystals are loaded along the ⟨100⟩ direction, four of the ⟨110⟩{110} glide systems are equally stressed. The Schmid factor ϕ is the same for all four slip systems [13]: $\phi = 0.5$, as indicated in fig. 4. However, in compression tests on NaCl one rarely finds a significant amount of glide on all four systems together. It was observed by Pratt [24], Davidge and Pratt [25], Mendelson [26] and Heidemann [27] that initially in a region of "pre-yield" (up to 0.3% strain) deformation occurs by slip on these four glide systems, but beyond that strain range only one of these four systems is operative in stage I, and the others are blocked.

In the "pre-yield" range of deformation the first dislocation bands are quite isolated. The edge bands are strongly birefringent [25] and they are nucleated at or near the specimen surface. Well-defined tilts are produced on the surface, corresponding to the movement of about 500 dislocations through the surface [25, 28]. Slip then develops by an increase in the number of bands of one system and by band broadening on this system until glide has penetrated the whole crystal at the end of stage I. This broadening has been interpreted in terms of a cross-glide mechanism leading to dislocation multiplication [29] and dislocation multipole formation [30].

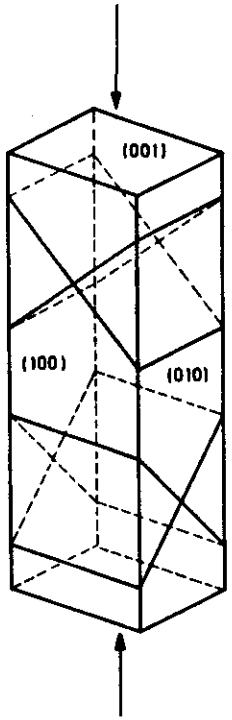

Fig. 4. Principal slip planes in rocksalt-structure crystal loaded along the ⟨100⟩ direction.

That deformation in stage I is dominated by one activated "primary" slip system was found by Davidge and Pratt [25], Hesse and Matucha [31], Hesse [32], Argon et al. [33], Heidemann [27] and Hesse and Hobbs [34]. Some dislocations are trapped by the weak, inactive conjugate slip bands, which results in the formation of kink joints [25] or in local glide polygonization [25, 26]. Generally speaking, the increase of the shear strain takes place by the broadening of the single slip planes into bands of closely spaced parallel planes and by an increase in the number of bands. The inactive secondary slip bands are acting as traps for the dislocations of the major slip system. When stage I is terminated the distance between dislocations in the slip planes approaches the distance of about 1.2 μm between the slip bands [25].

Electron microscopic investigation by Hesse and Matucha [31] of carbon replicas of ⟨110⟩ specimens deformed in stage I confirmed that mainly pure single slip was visible. In addition, a transition was observed from a region with $[\bar{1}10](110)$ single slip to a region with $[110](\bar{1}10)$ single slip. A similar phenomenon was described by Kear et al. [35] as "block slip", i.e. separate primary systems are operative in different parts of the crystal so that mainly single glide occurs. However, near the "block" boundaries of such regions intersections of dislocations on orthogonal systems can occur, giving rise to double slip.

If glide on the preferred {110} planes is impeded in certain experimental conditions,

e.g. compression of ⟨111⟩ oriented crystals – in which the Schmid factor for {110} glide is equal to zero – subsidiary glide on {100} and {111} planes can be expected. Franzbecker [36] indeed observed simultaneous glide on {100} and {111} planes at high stress levels, whereas other research workers [37–40] concluded that glide occurs mainly on {100} planes. Recently, Bhagavan Raju and Strunk [55] carried out a detailed investigation of plastically deformed ⟨111⟩ oriented NaCl single crystals by etching and X-ray topography; the results suggest that glide starting on {111} planes develops at a much lower critical resolved shear stress than glide on {100} planes. The preference of {111} glide over {100} glide has also been concluded from slip-line observations [41] on deformed ⟨110⟩-NaCl crystals; screw dislocations cross slip from {111} onto {100} planes.

In stage II, work hardening increases, especially for compression axes other than ⟨100⟩; slip steps on oblique {110} and on {001} planes become visible in ⟨100⟩ compressed NaCl [41, 25]. The deformation is dominated by slip on the same slip system as is active in stage I [27, 25, 31]. According to Matucha [41], at the end of stage II about 10% of the total slip occurs on oblique {110} and about 1% on {100} planes. Haasen reported a transmission electron microscopic study by Strunk [42] of ⟨100⟩ oriented NaCl crystals compressed at room temperature. In the stage II region of deformation he found dislocations of two {110}⟨110⟩ slip systems which were in oblique orientation to each other.

Stage III is associated with the activation of cross slip on {111} and {100} planes. Franzbecker [36] also observed {112} cross-slip traces on replicas. This was confirmed by Strunk, who also revealed cross-slip planes of higher indices [42].

Dislocation distribution. The distribution of screw dislocations in stage I is fairly random. Near the onset of stage II dislocation walls are formed through polygonization [26, 25]. Strong walls are built up in stage II where polygonization becomes more important. Transmission electron microscopy studies of ⟨100⟩ compressed NaCl single crystals [34] in stage II showed a non-uniform distribution of dislocations. Most of the dislocations appear to have pure edge character with a preferred orientation of the dislocation lines parallel to the ⟨100⟩ direction.

Argon et al. [33] considered that random slip on the conjugate system can increase the hardening rate and thus limit the easy-glide extension of stage I. In stage II of deformation the conjugate dislocation bands accumulate dislocations as a result of glide on the primary system in the interband region. Birefringent secondary dislocation bands are formed, but the internal stresses associated with such secondary slip bands do not appear to affect the flow stress directly.

Hesse and Hobbs [34] observed many pure edge dipoles in stage II. The observed pure edge character of the dipoles is consistent with the forest-intersection model [43, 44] based on the intersection of dislocations of orthogonal ⟨110⟩{110} glide systems, and with the stress-field trapping model [45]. Dipole formation seems to be easier in compression with axis ⟨110⟩ than in compression with axis ⟨100⟩. In the latter, the Schmid factor on {100} planes is zero, so there is no resolved shear stress on the {100} cross-slip planes.

Dislocation density. The relation between the flow stress τ and the total dislocation density ρ for the alkali halide crystals – in particular for NaCl and LiF – has been the

subject of considerable controversy over the past two decades. The density of the screw components of primary glide dislocations may be obtained by sectioning the ⟨100⟩ oriented crystal normal to the Burgers vector and etching, or the projection of this density on {001} planes may be obtained from sections parallel to the axis of the specimen. Let ρ_S^S be the projection of the primary screw dislocation density on {001} surfaces. From etch-pit measurements several authors [32, 46, 25] proposed for stage I of the deformation a proportionality between τ and $(\rho_S^S)^{1/2}$ analogous to what is observed in f.c.c. metals [49, 50], whereas for stage II a linear relation $\tau \approx \rho_S^S$ was suggested. However, a number of other authors [47, 48] suggested that $\tau \approx (\rho_S^S)^{1/2}$ holds for both stages I and II of the deformation. Etch-pit measurements in LiF [51], electron microscopy [52] and the observation of X-ray profiles [53] of NaCl resulted in a unique relationship $\tau = A(\rho_S^S)^{1/2}$ for both stages I and II of work hardening, suggesting a forest-intersection mechanism. More recent results obtained by Hesse and Hobbs [34] using both etch-pit and electron transmission techniques confirmed the parabolic relationship between the flow stress and the density of screw dislocations for NaCl even at high degrees of deformation in stage II at various doping concentrations and for crystals with ⟨100⟩ and ⟨110⟩ orientations. The failure of the earlier workers to observe this relationship in stage II was most likely due to inadequate etch-pit resolution. The flow stress may be written in the form:

$$\tau = \alpha \mu b (\rho_S)^{1/2}, \tag{1}$$

where μ represents the shear modulus, ρ_S represents the screw dislocation density. For compression along ⟨100⟩, over a wide range of temperatures and strain rates [54] the constant α has a value of about 0.4 which is independent of impurity concentration and heat treatment. For compression along ⟨110⟩ there are not as many data, but it is clear that $\alpha_{(110)} < \alpha_{(100)}$ [34].

Davidge and Pratt [25] observed for the ratio of edge to screw dislocation densities the value 5 and Hesse [32] about 3. It is observed that this ratio is a constant in stage I as well as in stage II.

Deformation stages in NaCl single crystals. We review here, as relevant for our investigations, what is known experimentally and theoretically of work hardening in NaCl in stage I and stage II only. Even so, our present knowledge and theoretical insight are not entirely satisfactory; although the broad outline of what happens during hardening in these two stages is fairly well known there is no consensus concerning the details.

In recent years Frank [43, 44], Evans and Pratt [56] and Argon and Padawer [57] have carried out experimental and theoretical investigations of work hardening in these crystals. A decrease of slip-line length is observed with increasing strain in stage I, indicating that blocking obstacles are being formed in increasing density. These obstacles are created by the formation of junctions between dislocations of the primary slip system and those of a secondary slip system on a plane inclined to the primary slip plane. The dislocations of the secondary system taking part in the creation of blocking obstacles have to be locally mobile, but otherwise they act as forest dislocations to the glide on the primary system.

Furthermore, the primary dislocations may cross slip when in the screw orientation, and sessile jogs may be created in these screw dislocations which impede their further progress. Thus, in the view of Evans and Pratt [56], there are at least three components of the stress which contribute to the strain hardening in stage I: the interaction with the forest dislocations results in a term τ_f, the sessile jogs in the screw dislocations give rise to a component τ_j, while the blocking obstacles exert a back stress τ_b on the moving dislocations.

Experimentally, the work-hardening rate is found to depend on strain rate and temperature. As the density of sessile jogs depends on the frequency with which cross slip occurs, which is a thermally activated process, the experimental finding can be interpreted as τ_j being predominant in stage I. In addition, the length of the glide lines in stage I is indicative of a low density of forest dislocations and blocking obstacles [53], i.e. of low τ_b and τ_f values.

At the onset of stage II, glide on secondary systems begins, and although the amount of slip on the secondary system does not approach that on the primary system, the frequency with which blocking obstacles are created on the primary system increases drastically. As a result, the stress components τ_b and τ_f increase much more rapidly with strain than in stage I. On the other hand, since there is no particular reason why cross slip should increase, τ_j should have essentially the same value as in stage I.

According to this description, which follows closely the theory of Evans and Pratt [56], especially as regards the additivity of the three strain-hardening terms, slip on the two planes of one conjugated system takes place in stage II.

Matucha [41] initially reported for stage II slip on two pairs of conjugated systems, and Frank [43, 44] based his work-hardening theory on this fallacious observation. It was later withdrawn, and thus Frank's theory proved fatally flawed; however, a number of his ideas were taken over in later work-hardening theories.

Later on a theory of strain hardening for stages I and II was proposed by Argon et al. [33, 59, 60], which was supported by direct experimental observation. The theoretical description is based on the notion, introduced earlier by Argon, of dislocation flux conductance, which was originally applied to metals. In stage I this conductance decreases as a result of the statistical growth of edge dislocation multipoles. This statistical process of dislocation retention predominates during strain hardening as long as the interference between the primary and secondary systems is minimal.

Argon et al. observed that in stage II long, thin bands of fibrillar birefringence are created, which they explained as being formed by isolated slip on the conjugated secondary slip system. These birefringent bands constitute obstacles to the passage of primary dislocations, causing an increase of the work-hardening rate.

This model predicts a work-hardening rate for stage II which is comparable to the one actually observed, but it also predicts that the work-hardening rate is independent of temperature. The original theory had to be modified by the assumption that at lower temperatures the production of conjugate slip bands is impeded by retained primary dislocations. The model does not take into account glide on oblique secondary slip systems, but probably such glide is not essential to hardening in

comparison with the hardening caused by the glide on the conjugated secondary glide system.

The rather unsatisfactory state of affairs as regards theories of the work hardening of NaCl structures is obvious from the foregoing account; in part it may be due to inaccuracies in the observations reported, and to variations in sample preparation and purity. From the preceding discussion of dislocation density it is clear, however, that the proportionality of τ to $\rho^{1/2}$ should be accounted for in any work-hardening theory.

2.2. Dislocations in f.c.c. metals

The glide system commonly operative in f.c.c. metals is $\langle 110\rangle\{111\}$; stable stacking faults can be formed on the densely packed $\{111\}$ planes. For a review of the various dislocations observed in f.c.c. materials the reader is referred to Amelinckx's article in this series [13]. Some of the properties of dislocation propagation found in polycrystalline f.c.c. materials have been studied in detail in single crystals, but in spite of the microscopic similarities, the macroscopic mechanical behaviour is quite different in the two cases. Single crystals exhibit the "easy glide" phenomenon which is observed in stage I of $\langle 100\rangle$ and $\langle 110\rangle$ NaCl single crystals, and which is absent in polycrystalline material.

The $\langle 110\rangle\{111\}$ dislocations may form Lomer–Cottrell locks [61, 62], which can be an important component of strain hardening. This may come about as follows: a $\frac{1}{2}[01\bar{1}]$ dislocation on (111) is split in two Shockley partial dislocations:

$$\tfrac{1}{2}[01\bar{1}]\rightarrow\tfrac{1}{6}[11\bar{2}]+\tfrac{1}{6}[\bar{1}2\bar{1}]; \tag{2}$$

similarly, a $\frac{1}{2}[101]$ on $(11\bar{1})$ may split. The two glide planes intersect along $[1\bar{1}0]$, and partials of each of the two decomposed perfect dislocations may react along this $[1\bar{1}0]$ line:

$$\tfrac{1}{6}[\bar{1}2\bar{1}]+\tfrac{1}{6}[2\bar{1}1]\rightarrow\tfrac{1}{6}[110]. \tag{3}$$

The two remaining partials lie on the two glide planes and the $\frac{1}{6}[110]$ "stair-rod" dislocation lies on (001); the whole configuration is therefore sessile.

Only if the three dislocations are forced to combine:

$$\tfrac{1}{6}[11\bar{2}]+\tfrac{1}{6}[112]+\tfrac{1}{6}[110]\rightarrow\tfrac{1}{2}[110] \tag{4}$$

can the perfect dislocation which results glide on the (100) plane. The possibility of such glide on $\{100\}$ planes was suggested by Cottrell [61], and earlier, Schmid and Boas [63] had detected by X-ray techniques slip on $\{100\}$ in Al deformed above 480°C. In transmission electron microscopy of Cu Steeds and Hazzledine [64] observed a Lomer–Cottrell dislocation lock slipping out of the foil, indicating glide on $\{100\}$, a result confirmed by the more recent electron microscope studies of Karnthaler [65, 66] on Ag, Al, Cu and Ni. Slip traces observed by Lacombe and Beaujard [67] showed that the phenomenon was not limited to thin foils.

The recombination reaction (3) depends on the stacking-fault energy and the local

stress, which might be produced by piled-up dislocations, as calculated by Stroh [68]. As the number of piled-up dislocations considered in the theory exceeds that observed [69], Karnthaler proposed that mobile constricted nodes must be present in the decomposed sessile $\frac{1}{2}[110](100)$ dislocation.

A second important hardening mechanism is the formation of jogs by dislocation intersection; non-glissile jogs in screw dislocations which have to be dragged along, creating strings of point defects, are especially effective in strain hardening.

Dislocations in f.c.c. single crystals. Slip-line observations in f.c.c. single crystals using electron microscope replica techniques showed that in stage I the slip lines are long, in the order of 100 μm [70]. According to Mader [71] and Seeger et al. [50] the number of dislocations per slip line increases at the end of stage I and remains constant in stage II. Moreover, the heights of slip lines increase with increasing strain. The length of the slip lines and hence the slip distance L_{II} of dislocations of the preferentially operative slip systems in stage II was found to be dependent on the resolved plastic strain a and the strain at the beginning of stage II, a^*, according to

$$L_{II}=\lambda_{II}/(a-a^*), \tag{5}$$

where λ_{II} is a constant. Relation (5) appeared to be valid for Cu [71] and for NaCl [41].

Using transmission electron microscopy, Mughrabi [72, 69] observed in stage I that the majority of the dislocations in Cu are primary dislocations which frequently form dipoles and planar multipoles. In this experiment Cu single crystals oriented for single slip were deformed in tension at 78 K and irradiated with fast neutrons at 20 K before removal of the load in order to pin the dislocations. In stage II dislocation grids (sheets) are observed both in the stress-removed and in the stress-applied states. He concluded that considerable rearrangement occurs upon unloading in stages I and II and that dislocation pile-ups exist in the stress-applied state. Earlier observations in copper [73–75, 64] show that the density of secondary dislocations in stage I is rather low in comparison with that of primary dislocations. In stage II these two densities appeared to be of the same order.

It is generally accepted that the flow stress can be correlated with the average dislocation density through the equation: $\tau\propto\rho^{1/2}$. However, there exists no consensus as regards ρ. A number of research workers state that the flow stress is controlled by the density of the primary dislocations ρ_p, whereas other investigators claim that the forest dislocation density is the controlling factor for the flow stress in stages I and II. (For a review see Basinski and Basinski in this series [76] and Hirsch [77].) As regards the low-temperature flow stress in single f.c.c. crystals it seems either that the flow stress is controlled by the forest dislocations or that the long-range stresses of primary dislocations and forest contributions are in a constant ratio. Furthermore, the low-temperature flow stress is partly temperature dependent. This temperature dependence is usually attributed to the cutting of forest dislocations by the primary dislocations (see Mughrabi for a review [78]). It has generally been concluded that the forest density and therefore the thermal component of the flow stress remain constant in the easy-glide region of deformation. However, recently Argon and East [79] argued, on the basis of their measurements of the obstacle profiles for the intersection of forest dislocations, that this latter conclusion seems to be incorrect, because

it could not have resulted in the observed thermal and athermal components of the flow stress.

Before concluding this subsection we must refer to Hirsch's argument [77] that correlations between the flow stress and the average dislocation density may not be physically significant, since the flow stress will most likely be determined by local interactions between non-uniformly distributed dislocations. The remark highlights the difficulty of interpreting the statistical effects of the various potential contributions to work hardening.

Work hardening of polycrystalline f.c.c. metals. In our NMR experiments we are dealing with polycrystalline Al foils in which the work-hardening phenomenon occurs. For a general discussion of it, including polycrystals, reference should be made to the review by Basinski and Basinski in this series [76] and to the review by Hirsch [77] on the work-hardening theories of single crystals. Nabarro et al. [80] have reviewed the proposed theoretical models for single-crystal work hardening critically; only three appear to survive.

The fundamental difference between the nature of the slip process in polycrystalline material as compared to that in single crystals resides in the fact that at least five slip systems have to be operative in each crystal grain of the polycrystalline material in order to maintain compatibility between the plastic deformations of the individual grains. For this reason easy glide is impossible in polycrystalline material, and, for this reason too, the many attempts made long ago to derive work-hardening curves of polycrystalline materials from those obtained on single crystals could not be successful.

In terms of dislocations the difference can be expressed by the difference between the two categories of dislocations distinguished by Ashby [81]: "statistically stored" dislocations accumulating by self-trapping during plastic deformation, and "geometrically necessary" dislocations which maintain compatibility between crystal grains. The "geometrically necessary" dislocations can pile up against the grain boundaries, and thus cause long-range stress fields in the two adjoining grains; the compatibility between grains is thus maintained by additional elastic deformations. The densities of the statistically stored and geometrically necessary dislocations will be denoted ρ_{st} and ρ_g respectively.

Ashby pointed out that the statistical density ρ_{st} depends on strain and on slip distance Λ_{st} according to

$$\rho_{st} \simeq a/b\Lambda_{st}, \tag{6}$$

and the geometrical dislocation density depends on strain and on grain size d (in the limit of low strains) as:

$$\rho_g \simeq a/4bd. \tag{7}$$

The occurrence of polyslip and of geometrically necessary dislocations constitute the main differences between work hardening in single crystals and in polycrystalline materials. The recent work by Mecking [82, 83] emphasizes that for f.c.c. metals there is some similarity between the work-hardening curves in single crystals and in polycrystals in that in the latter, too, different stages of work hardening may be distinguished (fig. 5) if low-temperature tests are performed. Given this finding, it is useful to distinguish these stages 1, 2 and 3 in the way Mecking does (Arabic numerals differentiate these stages from the ones denoted by Roman numerals in single crystals).

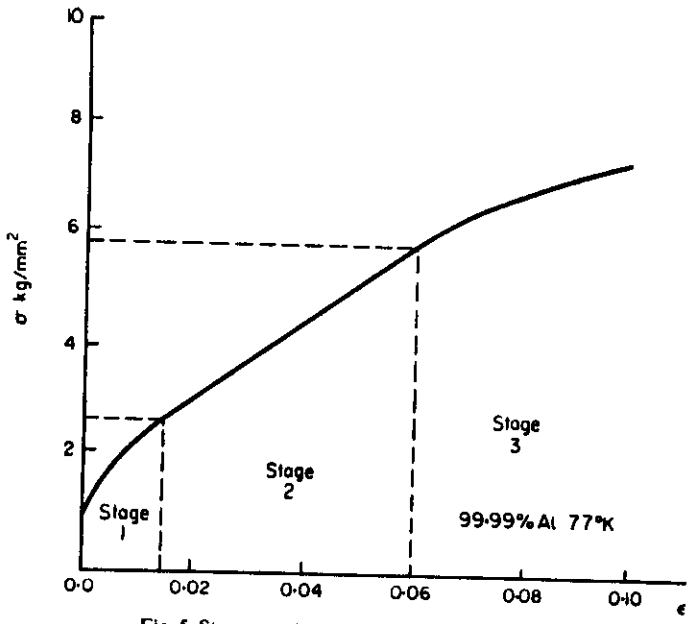

Fig. 5. Stress–strain curve of polycrystalline Al.

The distinguishing characteristic is that the second derivative $d^2\sigma/d\varepsilon^2$ for stage 2 is larger than that either in stage 1 or stage 3, where it is negative, while in stage 2 the value of $d^2\sigma/d\varepsilon^2$ may occasionally approach zero [82]. This type of strain-hardening curve is a marked departure from the common description of the curve by a power law or a parabola, which suggests a single work hardening process; the parabolic hardening was essentially predicted by Taylor's work-hardening theory.

Moreover, it was remarked by Mecking that in stage 2 the hardening rate is athermal, while stage 3 is thermally activated. Mecking draws the parallel with stages I and II and stage III in single crystals, but from our own work on NaCl single crystals it is clear that stage II is not different from stage I as regards thermal activation. We performed [84] a series of stress-relaxation tests at various strains in stages I and II, and found that throughout the range of our tests the strain-rate sensitivity $d\sigma/d \ln \dot{\varepsilon}$ is proportional to σ, which conforms to the Cottrell–Stokes law. No change occurs in this relationship when the strain hardening passes from stage I to stage II. Moreover, as the basic mechanism underlying the change from stage 1 to 2 in polycrystals cannot possibly be the same as that for the change from stage I to II in single crystals, the comparison does not appear justified.

Mecking [82] remarks that the formation of cell walls of dislocations, a process occurring in stages 2 and 3, begins near the grain boundaries. As we saw earlier, most of the geometrically necessary dislocations are piled up near the grain bound-

aries. Accordingly, Kocks and Mecking [85] have extended the Taylor model by assuming that within each grain two different regions may be distinguished, viz. a layer of thickness t near the grain boundary, and the interior of the grain. The density of dislocations in the boundary layer is denoted by ρ_{ext}; there are two contributions to that density, viz. one due to statistically stored dislocations, and one due to geometrically necessary ones.

The derivative of the dislocation density ρ_{ext} with respect to the resolved strain then comprises two terms:

$$\frac{d\rho_{ext}}{da}=\frac{(\rho_{ext})^{1/2}}{\beta b}+\frac{1}{bt}, \tag{8}$$

where β is a constant. For a single crystal only the first term on the right-hand side of the equation would have been present.

Kocks and Mecking assume that for the interior region of the grain the stress–strain dependence of a single crystal in stage II is valid:

$$\tau_{int}=\tau_0+\theta_{II}a, \tag{9}$$

in which θ_{II} is the strain-hardening coefficient in stage II, and τ_0 the shear stress at the onset of that stage. Furthermore, they assume that the local flow stress in a grain is composed of the flow stress of the interior and exterior regions in proportion to their volumes, or

$$\tau=\tau_{int}\left(1-c\frac{t}{d}\right)+\tau_{ext}c\frac{t}{d}, \tag{10}$$

where c is a constant depending on the shape of the grain: for a cube, $c=6$, for a sphere, $c=3$; Kocks and Mecking used $c=4$. The ratio between t and the grain diameter d is assumed to be small.

In spite of the dubious nature of some of its underlying assumptions, the model of Kocks and Mecking has the merit that it predicts at least the right order of magnitude for the effect of grain size on the work hardening in stage 2.

In contrast to stage 2, thermally activated rearrangements of dislocations in ordered patterns occur in stage 3. It is generally believed that the rearrangements at low temperatures are controlled by cross slip and therefore depend on the stacking-fault energy (listed in table 1). At higher temperature the diffusion coefficient plays an additional role of importance. Cell structures are observed on low-temperature deformation and sub-grain boundaries at higher temperatures in stage 3. The grain-size effect in stage 3 has not been investigated thoroughly. However, it can be expected that size effects will play a minor role in stage 3 hardening because the inhomogeneous distribution of dislocations in stage 2 is transformed into more homogeneous sub-boundaries and cell structures in stage 3.

Before concluding this section, it should be noticed that many of the results mentioned were obtained using transmission electron microscopic observations and optical micrographs of slip lines. In particular, slip-line observations are essentially surface observations. Undoubtedly the deformation of the surface layer can be considerably different from that in the interior of the crystal [86], so that slip-line patterns do not necessarily represent the bulk properties. There is without any question also some rearrangement of dislocations occurring during sample preparation [87]. Therefore there still exists in the field of crystal plasticity a need for new techniques which aim at measuring bulk properties on a microscopic scale. Pulsed nuclear magnetic resonance is such a new complementary technique for studying dislocations in solids.

Table 1
Stacking-fault energy of aluminium [88] estimated by various methods.

Methods	γ(erg/cm^2)
Creep data	>200
Absence of tetrahedra	>150
2 × coherent – twin energy	200
Loop annealing	280
Loop annealing	210
Loop annealing	200
Loop annealing	135

3. *Fundamentals of static quadrupole effects in dislocated solids*

3.1. Electric field gradient tensor

Nuclei with spin $I>\frac{1}{2}$ possess an electrical quadrupole moment Q which interacts with the gradient $\{V_{ik}\}$ of an electric field. If the electric field gradient tensor (EFG) $\{V_{ik}\}$ at the site of the nucleus is caused by a surrounding with cubic symmetry it follows that $V_{XX}=V_{YY}=V_{ZZ}$, where (X, Y, Z) is the principal coordinate system of the EFG. Because of the Laplace equation $V_{XX}+V_{YY}+V_{ZZ}=0$, the EFG vanishes. In crystals the individual ions are assumed to have spherical symmetry in a first approximation. Thus the EFGs due to their own electron cloud vanish. Therefore the EFG at a nucleus in the lattice originates from neighbouring ions. In a perfect cubic crystal the EFG at each nucleus caused by the neighbouring atoms is zero owing to the cubic symmetry.

However, lattice defects such as dislocations in the crystal can destroy the cubic symmetry, producing local field gradients which would cause a quadrupolar interaction. The corresponding quadrupole Hamiltonian $\hat{H}_Q$ in an arbitrary coordinate system (x, y, z) can be written [89–91] as:

$$\hat{H}_Q=\sum_{i=1}^{N}\sum_{q=-2}^{+2}V_{-q}^{i}\hat{Q}_q^i, \tag{11}$$

where

$$\hat{Q}_0=\alpha[3I_z^2-I(I+1)],$$
$$\hat{Q}_{\pm1}=\alpha[I_zI_\pm+I_\pm I_z],$$
$$\hat{Q}_{\pm2}=\alpha I_\pm^2,$$

and

$$V_0 = V_{zz},$$
$$V_{\pm 1} = (V_{xz} \pm j V_{yz}),$$
$$V_{\pm 2} = \tfrac{1}{2}(V_{xx} - V_{yy}) \pm j V_{xy},$$

with the abbreviation $\alpha = eQ/[4I(2I-1)]$ (I_z, $I_\pm$ are operators of the nuclear spin I; N is the number of nuclei in the sample).

In the presence of a strong magnetic field H_0, usual in NMR experiments, the Hamiltonian $\hat{H}_Q$ acts as a perturbation of the Zeeman Hamiltonian $\hat{H}_Z$ of the spin which is given by the magnetic field. The time-independent first-order perturbation theory leads to a quadrupole distortion frequency:

$$\omega_Q^{(m)} = (2m+1)\frac{3\alpha}{\hbar} V_{zz} = (2m+1)a \tag{12}$$

of the satellite transition $m-1 \rightarrow m (m \neq \frac{1}{2})$.

In second order, the central transition $-\frac{1}{2} \rightarrow \frac{1}{2}$ is also shifted by

$$\omega_Q^{(2)} \approx \frac{\alpha^2}{\omega_0}\left[-|V_1|^2 + \tfrac{1}{2}|V_2|^2\right]$$

In eq. (12), V_{zz} is the component of the EFG $\{V_{ik}\}$ at a given nucleus in the direction of the applied magnetic field H_0. Generally the transformation of the EFG $\{V_{ik}\}$ from a frame of reference (ξ_1, ξ_2, ξ_3) to a frame (η_1, η_2, η_3) is given by the well-known formula:

$$\{V_{ik}^{\eta_i}\} = \mathbf{T}\{V_{ik}^{\xi_i}\}\mathbf{T}^{-1}. \tag{13}$$

The orthogonal rotation tensor $\mathbf{T} = \{t_{ik}\}$ is defined by the equation:

$$\begin{pmatrix}\eta_1\\ \eta_2\\ \eta_3\end{pmatrix} = \mathbf{T}\begin{pmatrix}\xi_1\\ \xi_2\\ \xi_3\end{pmatrix}; \qquad \text{i.e. } \mathbf{T} = \{t_{ik}\} = \{\cos(\eta_i, \xi_k)\}. \tag{14}$$

From the orthogonality of both frames it follows that $\mathbf{T}^{-1} = \{t_{ki}\}$. Therefore eq. (13) may be rewritten as:

$$V_{ik}^{\eta_i} = \sum_{l,m} V_{lm}^{\xi_i} t_{il} t_{km}. \tag{15}$$

Replacing the system (η_i) by the laboratory frame (x, y, z), the component V_{zz} of the EFG in the direction of the external magnetic field H_0 is given in the first-order quadrupole perturbation by the following expression:

$$V_{zz} = V_{11}t_{31}^2 + V_{22}t_{32}^2 + V_{33}t_{33}^2 + 2V_{12}t_{31}t_{32} + 2V_{13}t_{31}t_{33} + 2V_{23}t_{32}t_{33}. \tag{16}$$

For example, with this equation it is possible to determine the component V_{zz} from an EFG given in the coordinate system of the lattice defect. If the EFG $\{V_{ik}\}$ is given in the principal coordinate system (X, Y, Z), the off-diagonal elements vanish, so that eq. (16) is of the form:

$$V_{zz} = V_{XX}t_{31}^2 + V_{YY}t_{32}^2 + V_{ZZ}t_{33}^2. \tag{17}$$

Assuming the elements t_{ik} to be expressed by the Eulerian angles (ϕ, θ, ψ), generating (x, y, z) from (X, Y, Z), it follows from eq. (16) that

$$V_{zz} = V_{ZZ}\cos^2\theta + V_{XX}\sin^2\phi\sin^2\theta + V_{YY}\cos^2\phi\sin^2\theta,$$

or with

$$\eta = (V_{XX} - V_{YY})/V_{ZZ},$$
$$V_{zz} = \tfrac{1}{2}V_{ZZ}(3\cos^2\theta - 1 - \eta\sin^2\theta\cos 2\phi). \tag{18}$$

According to this equation it is possible to determine the maximum field gradient component V_{zz} and the asymmetry parameter η from a rotation pattern of the single crystal. This is shown in detail by Volkoff et al. [92, 93].

As discussed above, if the nuclear environment has a cubic point symmetry, the EFG $\{V_{ik}\}$ at the nucleus site vanishes. In the presence of strain, however, the cubic symmetry is destroyed and electric field gradients are created. In the elastic region, i.e. for sufficiently small strain, the EFG $\{V_{ik}\}$ can be correlated with the strain tensor $\{\varepsilon_{ik}\}$ or the stress tensor $\{\sigma_{ik}\}$ by a set of linear equations as shown by Shulman et al. [12]. In the Voigt notation, the relation can be written as

$$V_{ik} = \sum_{i=1}^{6} S_{ii}\varepsilon_{ik} = \sum_{i=1}^{6} C_{ii}\sigma_{ik}. \tag{19}$$

By symmetry arguments valid for a cubic lattice the gradient-elastic tensor $\{S\}$ as well as the gradient-stress tensor $\{C\}$ can be shown to possess only two independent elements, leading to:

$$V_{x_ix_i}\begin{Bmatrix} = S_{11}[\varepsilon_{x_ix_i} - \tfrac{1}{2}(\varepsilon_{x_jx_j} + \varepsilon_{x_kx_k})] \\ = C_{11}[\sigma_{x_ix_i} - \tfrac{1}{2}(\sigma_{x_jx_j} + \sigma_{x_kx_k})] \end{Bmatrix} \quad \text{cyclic,} \tag{20a}$$

$$V_{x_cx_k} = S_{44}\varepsilon_{x_cx_k} = C_{44}\sigma_{x_cx_k} \qquad (c \neq k). \tag{20b}$$

The coefficients S_{11}, C_{11}, S_{44} and C_{44} are related to the elastic compliance constants s_{ik} by:

$$C_{44} = s_{44}S_{44}, \tag{21a}$$
$$C_{11} = (s_{11} - s_{12})S_{11}. \tag{21b}$$

3.1.1. Homogeneous external stress

In the following the stress tensor $\{\sigma\}$ may be given by an external stress acting in the x-direction of the laboratory frame (x, y, z):

$$\{\sigma\} = \sigma_0\begin{pmatrix}1 & 0 & 0\\ 0 & 0 & 0\\ 0 & 0 & 0\end{pmatrix} \tag{22}$$

Transforming this matrix into the crystal axis system (x_1, x_2, x_3), substituting the matrix elements into eq. (20a), and then transforming back into the laboratory frame, leads [94] to the EFG

(a) σ_0 parallel to ⟨100⟩:

$$\{V^{(x,y,z)}\} = \frac{\sigma_0 C_{11}}{2}\begin{pmatrix} 2 & 0 & 0 \\ 0 & -1 & 0 \\ 0 & 0 & -1 \end{pmatrix}; \qquad V_{zz} = -\frac{\sigma_0 C_{11}}{2}. \tag{23a}$$

(b) σ_0 parallel to ⟨110⟩:

$$\{V^{(x,y,z)}\} =$$

$$\frac{\sigma_0}{4}\begin{pmatrix} C_{11}+2C_{44} & 0 & 0 \\ 0 & -C_{44}+\frac{1}{2}C_{11}+(\frac{3}{2}C_{11}-C_{44})\cos 2\phi & (C_{44}-\frac{3}{2}C_{11})\sin 2\phi \\ 0 & (C_{44}-\frac{3}{2}C_{11})\sin 2\phi & -[\frac{1}{2}C_{11}+C_{44}+(\frac{3}{2}C_{11}-C_{44})\cos 2\phi] \end{pmatrix} \tag{23b}$$

$$V_{zz} = -\frac{\sigma_0}{4}[\tfrac{1}{2}C_{11}C_{44}+(\tfrac{3}{2}C_{11}-C_{44})\cos 2\phi],$$

(c) σ_0 parallel to ⟨111⟩

$$\{V^{(x,y,z)}\} = \frac{\sigma_0 C_{44}}{3}\begin{pmatrix} 2 & 0 & 0 \\ 0 & -1 & 0 \\ 0 & 0 & -1 \end{pmatrix}; \qquad V_{zz} = -\frac{\sigma_0 C_{44}}{3}. \tag{23c}$$

(d) Quasi-isotropic polycrystalline sample:

$$\langle V_{zz}^2\rangle = \sigma_0^2[(383/140)C_{11}^2+(17/21)C_{11}C_{44}+(124/315)C_{44}^2]. \tag{23d}$$

Here ϕ is the angle between the static magnetic field H_0 (z-direction) and the x_3 axis. Note that in cases (a) and (c) the component V_{zz} is independent of the angle ϕ.

Several experimental groups have used the quadrupole distortion of the NMR signal due to an external elastic stress in order to determine the two gradient-elastic constants for crystals with a cubic lattice structure (see references in table 2). Results of such experiments are shown in fig. 6, confirming the linear relationship between the external stress σ_0 and the quadrupolar shift frequency a_Q which is proportional to V_{zz}. Furthermore, the expected dependence of the frequency shift a_Q on the orientation of the crystal relative to the external field according to case (b) (σ_0 parallel to ⟨110⟩) is demonstrated in fig. 7.

Values of the gradient-elastic constants obtained by such "external stress" (ES) experiments are listed in table 2. In addition the table exhibits data of gradient-elastic constants determined by nuclear acoustic resonance (NAR) experiments, as first described by Bolef [95]. In this technique, the elastic distortion of the lattice due to an ultrasonic wave produces fluctuating field gradients $V_{\pm 1}$ and $V_{\pm 2}$ via eq. (19) which give rise to the nuclear spin relaxation process. Furthermore, it should be noted that gradient-elastic constants can also be determined for crystals with a non-cubic lattice structure. This was shown in the case of $^{23}NaNO_2$ by Kanashiro et al. [96].

3.1.2. Field gradients caused by stress fields of dislocations

A dislocation produces in its surrounding a local strain field $\{\varepsilon(r_j)\}$ and a corresponding stress field $\{\sigma(r_j)\}$ leading to a local EFG $\{V_{ik}(r_j)\}$ at the site r_j of a given nucleus.

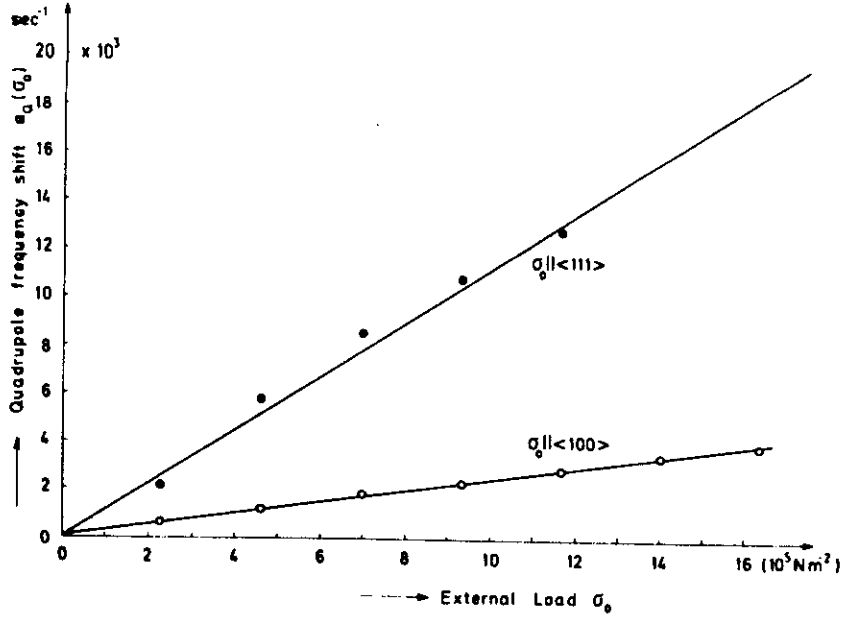

Fig. 6. Dependence of the quadrupole frequency shift $a_Q(\sigma_0)$ on the external stress for the ^{127}I resonance in RbI single crystals. Compression axes parallel to ⟨100⟩ and to ⟨111⟩ [134].

Table 2
Values of gradient-elastic constants (10^3 dyn$^{-1/2}$ = 10^3 statvolt/dyn)

Crystal	Nucleus	$\lvert C_{11}\rvert$	$\lvert C_{44}\rvert$	Method	Ref.
NaCl	^{23}Na	7.2	8.6	ES	[128]
		7.8	6.3	NAR	[129]
	^{35}Cl	9.1	34	ES	[128]
		6.9	27.5	ES	[130]
NaF	^{23}Na	6.2	4.95	ES	[130]
		4.75	5.25	ES	[131]
		3.7	-	NAR	[132]
RbCl	^{35}Cl	2.2	4.9	ES	[133]
	^{87}Rb	9.7	15.3	ES	[133]
RbI	^{87}Rb	44.5	51.7	ES	[134]
	^{127}I	22.6	160	ES	[134]
		51.5	-	NAR	[95]
Al	^{27}Al	4.0	6.7	ES	[135]
		3.7	10.6	NAR	[137]
Cu	^{63}Cu	ca. 0.1	ca. 0.15	ES	[106]
Ta	^{181}Ta	24.6	35.1	NAR	[137]
Nb	^{93}Nb	10.6	79.2	NAR	[138]
Mo	^{97}Mo	2.42	1.26	NAR	[139]

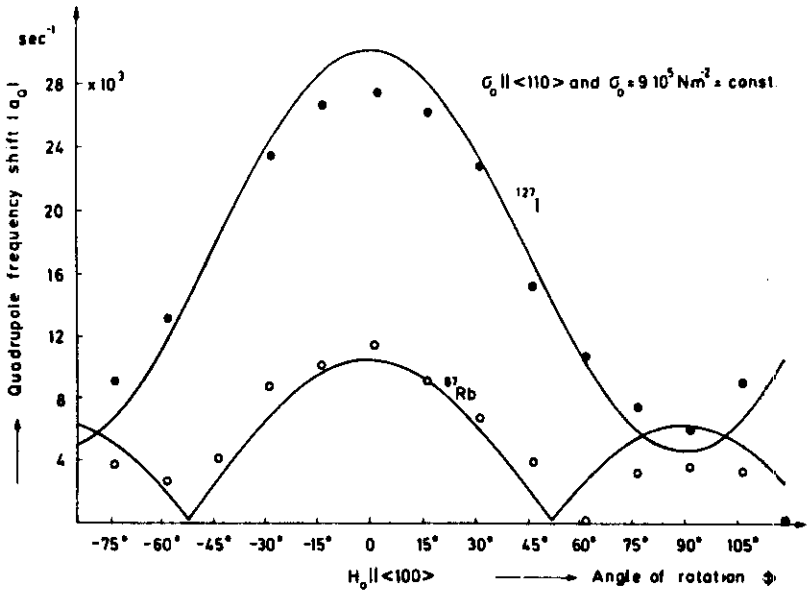

Fig. 7. Rotation pattern of the quadrupole frequency shift a_Q of ^{127}I and ^{87}Rb in an RbI single crystal elastically deformed in a ⟨110⟩ direction with $\sigma_0 = 9 \times 10^6$ dyn cm^{-2}. The solid curves represent the theory as discussed in the text [134].

At sufficiently large distances from the defect site the strains and stresses induced by the defect are small and can be described by linear elasticity theory. Assuming that in this region the EFG depends linearly on the stress or strain tensor, the EFG can be calculated, if the gradient-elastic constants introduced in the last section are known. In contrast, for ions situated in the neighbourhood of the defect the displacements are large, and linear elasticity theory fails in describing the ionic positions correctly. This region has to be treated on an atomistic scale. First, results will be presented in the region of linear elasticity theory as calculated by several authors [97–101]

The stress tensors of a screw and an edge dislocation in an isotropic medium are represented respectively in the frame ($v_1 = r\cos\theta$, $v_2 = r\sin\theta$, v_3 parallel to the dislocation line) of the dislocations by:

$$\{\sigma_S\} = \frac{K_S b}{2\pi r}\begin{pmatrix} 0 & 0 & f^S_{13}(\theta) \\ 0 & 0 & f^S_{23}(\theta) \\ f^S_{13} & f^S_{23} & 0 \end{pmatrix}, \tag{24a}$$

and

$$\{\sigma_E\} = \frac{K_E b}{2\pi r}\begin{pmatrix} f^E_{11} & f^E_{12} & 0 \\ f^E_{12} & f^E_{22} & 0 \\ 0 & 0 & f^E_{33} \end{pmatrix}, \tag{24b}$$

where K_S, K_E, f^S_{ik} and f^E_{ik} depend on the elastic moduli c_{11}, c_{12} and c_{44} and on the polar angle θ [102]. Furthermore, the relations (24a, b) are also valid for cubic crystals in the case of special directions of the dislocation relative to the crystal axes where [100, 101]: $c_{14} = c_{15} = c_{24} = c_{25} = c_{34} = c_{35} = c_{46} = c_{56} = 0$ (dislocation along a diad axis; as a result, the screw and edge components separate) or $c_{16} = c_{26} = c_{36} = c_{45} = c_{14} = c_{15} = c_{24} = c_{25} = c_{34} = c_{35} = c_{46} = c_{56} = 0$ (dislocation along a diad axis with another diad perpendicular). The crystal axes (X_1, X_2, X_3) of the lattice are related to the dislocation frames (v_1, v_2, v_3) by a rotation matrix $\{t_{ik}\}$ determined by the special type of slip system of the dislocation. Consequently, using the transformation (15) and eqs. (20a, b), the EFG in the surroundings of a screw and edge dislocation, respectively, can be written as:

$$\{V^S_{v_1,v_2,v_3}\} = \begin{pmatrix} 0 & 0 & V^S_{13} \\ 0 & 0 & V^S_{23} \\ V^S_{13} & V^S_{23} & 0 \end{pmatrix}, \tag{25a}$$

and

$$\{V^E_{v_1,v_2,v_3}\} = \begin{pmatrix} V^E_{11} & V^E_{12} & 0 \\ V^E_{12} & V^E_{22} & 0 \\ 0 & 0 & V^E_{33} \end{pmatrix}, \tag{25b}$$

with the condition $\mathrm{tr}\,\{V^E_{ij}\} = 0$.

Introducing the unit vector $\boldsymbol{h}$ in the direction of the external magnetic field H_0

$$\boldsymbol{h} = \begin{pmatrix} \cos(H_0, v_1) \\ \cos(H_0, v_2) \\ \cos(H_0, v_3) \end{pmatrix}, \tag{26}$$

the component V_{zz} which has to be used for the calculation of the quadrupole distortion frequency according to eq. (12) is given by the general relation

$$V_{zz} = \boldsymbol{h}\{V_{ij}\}\boldsymbol{h} = \sum_{i,j=1}^{3} V_{ij} h_i h_j, \tag{27}$$

leading to:

$$V^S_{zz} = 2h_3(h_1 V^S_{13} + h_2 V^S_{23}), \tag{28a}$$

$$V^E_{zz} = V^E_{22}(h_2^2 - h_1^2) + V^E_{33}(h_3^2 - h_1^2) + 2V^E_{12} h_1 h_2. \tag{28b}$$

Finally, substituting the coefficients K_S, K_E as well as the orientation functions f_S, f_E into eqs. (28a, b) the EFG V_{zz} in the surroundings of a screw and edge dislocation, respectively, may be written as:

$$V^{S,E}_{zz}(r, \theta, \boldsymbol{h}) = \frac{K_{S,E} b C_{11}}{2\pi}\frac{1}{r}\begin{Bmatrix} f_S(\theta, \boldsymbol{h}) \\ f_E(\theta, \boldsymbol{h}) \end{Bmatrix}, \tag{29}$$

where the orientation function $f_{S,E}$ depends on the direction of the dislocation line relative to the magnetic field direction and on the coefficients $k' = C_{44}/C_{11}$, c_{11}, c_{12} and c_{44} [103].

The mean EFG felt on the average by all atoms at a distance r from the dislocation

line is described by the root mean square $\langle f^2\rangle^{1/2}$ of the orientation functions $f_{S,E}$:

$$\langle f^2\rangle = \frac{1}{2\pi}\int_0^{2\pi} f^2\,\mathrm{d}\theta. \tag{30}$$

Furthermore, it is possible to introduce for a given slip system a total mean orientation function by:

$$\langle f^2\rangle = a_S\langle f_S^2\rangle + a_E\langle f_E^2\rangle, \tag{31}$$

where a_S and a_E are the relative abundances of screw and edge dislocations, respectively, with $a_S + a_E = 1$.

As shown by Brown [104] and Ogurtani and Huggins [105], in a metal near a dislocation a redistribution of conduction-electron charge density occurs analogous to the behaviour around point defects. From the redistribution around a dislocation, an oscillating potential with a period $2k_F$ (k_F: magnitude of the Fermi wave vector) results. This leads to a mean EFG at a distance r from the dislocation:

$$V_{zz}^{(S,E)}(r) \simeq 3k_F^{1/2}\frac{E_F}{e}(1-2\nu)r^{-5/2} \tag{32}$$

(E_F, Fermi energy; ν, Poisson's ratio).

An estimate shows that up to very high dislocation densities of the order of 10^{11} cm^{-2} the influence of the conduction electrons on the dislocation-induced quadrupole distortion remains below 1% [106].

Furthermore, in ionic crystals field gradients may be caused by a charged dislocation due to a jog in the dislocation line [107]. Starting from the electric field of a straight line with a charge density λ,

$$E_\lambda = 2\lambda/r, \tag{33}$$

according to Cohen and Reif [108] the total field gradient tensor at point r from the dislocation line can be written approximately as:

$$V_{zz}^{\lambda} \simeq (1+\gamma)\frac{2\varepsilon_r+3}{5\varepsilon_r}\frac{2\lambda}{r^2}. \tag{34}$$

where $(1+\gamma)$ represents the Sternheimer antishielding factor. It should be noted that the EFG V_{zz}^{λ} has the same geometrical structure as the EFG due to the stress field of a dislocation dipole which according to Greenberg [109] is given by:

$$V_{zz}^{D} \simeq DC_{11}\frac{h}{r^2}f_D(\theta,\hbar). \tag{35}$$

Here h is the spacing of the dislocation dipole, $D = \mu b/2\pi(1-\nu)$, with μ being the shear modulus, and f_D is an orientation function with $\langle f_D^2\rangle^{1/2}$ of the order of unity [110]. It can be shown that the charge effect is a factor of about 10^5 smaller than the strain effect around dislocations.

As a last remark concerning the region of linear elasticity theory the stress field tensor of a tilt boundary has the general form [111]:

$$\{\sigma^{(\nu_1,\nu_2,\nu_3)}\} = \frac{D}{h}\begin{pmatrix} t_u & t_m & 0 \\ t_m & t_v & 0 \\ 0 & 0 & t_w \end{pmatrix}, \tag{36}$$

where the matrix element t depends on the geometrical coordinates in a complicated way and h is the separation of the dislocations. In a rough approximation, the EFG V_{zz} can be expressed by:

$$V_{zz}(x) \simeq C_{11}\sigma_m(x). \tag{37}$$

In the case of an infinite dislocation wall, the stress component $\sigma_m(x)$ at a distance $x > h/\pi$ from the wall is given by [112]:

$$\sigma_m(x) = \frac{D\pi^2}{h^2}\frac{x}{\sinh^2(\pi x/h)}. \tag{38}$$

This leads to:

$$V_{zz}(x) \simeq \frac{D\pi^2 C_{11}}{h^2}\frac{x}{\sinh^2(\pi x/h)}, \tag{39}$$

with the asymptotic behaviour for $x > h$:

$$V_{zz}(x) \simeq \frac{D\pi^2 C_{11}}{4h^2}x\exp(-2\pi x/h). \tag{40}$$

From eq. (40) it follows that the EFG V_{zz} vanishes rapidly with increasing distance x. Therefore, it is to be expected that an observable quadrupole interaction exists only for nuclei in a small region of order h near a dislocation wall.

Contrary to the results based on the linear elasticity theory given above, the calculation of the EFG in the direct neighbourhood ($r \leqslant 3b$) of a dislocation is much more complex. A possible treatment is the extension of an analytical description of the EFG into the region $r \leqslant 3b$ using the computer-calculated positions r^0 of atoms in the core of a dislocation.

Hut et al. [84] have shown that for nuclei inside the core the radial function $f(r_i)$ of the electric field gradient can be expressed as

$$f(r_i) = -a_1 r_i^2 + a_2, \tag{41}$$

where the coefficients a_1 and a_2 are obtained by matching the function $f(r_i)$ and its first derivative to the EFG $V_{zz}(r)$ given by the linear elasticity theory at $r = 3b$.

Recently, a more direct calculation was carried out by Raupach [113] for alkali halide crystals. In his calculation, the crystal is considered to be built up of rigid ionic rows parallel to the dislocation line. Because of the periodicity of the lattice along the dislocation line, the EFG will be the same for all nuclei within an ionic row. Then the EFG at an arbitrary lattice site can be divided into two parts

$$V_{zz}^{i} = V_{zz}^{i0} + \tilde{V}_{zz}^{i}, \tag{42a}$$

where V_{zz}^{i0} is the contribution due to all ions of the ionic row containing the nucleus

under consideration, and

$$\tilde{V}_{zz}^{i}=\sum_{j} V_{zz}^{ij} \tag{42b}$$

represents the contribution of all other rows. V_{zz}^{ij} is the EFG induced at the site of a nucleus in the ionic row i by the ionic row number j. In all cases the external magnetic field (the z axis) was chosen parallel to one of the ⟨110⟩ directions.

For screw dislocations the result of the calculation is given by:

$$V_{zz}^{i0}=\frac{q_i}{2\sqrt{2\pi\varepsilon_0 a^3}}\sum_{m=1}^{\infty} m^{-3}, \tag{43}$$

and

$$\tilde{V}_{zz}^{i}=-\frac{2^{1/2}\pi}{\varepsilon_0 a^3}\sum_{\substack{j=1\\ j\neq i}}^{\infty} q_j \sum_{t=1}^{\infty} K_0\left(\frac{2^{1/2}\pi t r_{ij}}{a}\right)\cos\left(\frac{2^{1/2}\pi t z_{ij}}{a}\right), \tag{44}$$

where a is the nearest neighbour distance and $K_0(x)$ denotes the zero-order Mac-Donald function.

For edge dislocations, a treatment analogous to that used in the case of screw dislocations leads to the following expressions for the contributions to the EFG:

$$V_{zz}^{i0}=\frac{q_i}{2\pi\varepsilon_0 a^3}\sum_{m=1}^{\infty}\frac{(-1)^{m+1}}{m^3}, \tag{45}$$

$$\tilde{V}_{zz}^{i}=\frac{1}{\varepsilon_0 a^2}\sum_{\substack{j=1\\ j\neq i}}^{\infty}\left\{q_j\sum_{t=1}^{\infty}\left[\frac{(2t-1)^2\pi}{a}\frac{z_{ij}^2}{r_{ij}^2}K_0\left(\frac{\pi(2t-1)r_{ij}}{a}\right)\right.\right.$$

$$\left.\left.+\frac{2t-1}{r_{ij}^3}(2z_{ij}^2-r_{ij}^2)K_1\left(\frac{\pi(2t-1)r_{ij}}{a}\right)\right]\right\}. \tag{46}$$

Using the atomistically calculated positions for different potential functions and boundary conditions, the corresponding EFG at a cation site within the core of a screw and edge dislocation, respectively, is listed in table 3 for NaCl. As a result of the symmetry of the core configurations the symmetry relations $V_{zz}(-x,-y)=V_{zz}(x,y)$ for a screw dislocation and $V_{zz}(-z,x)=V_{zz}(z,x)$ for an edge dislocation, respectively, are expected for the EFG.

The differences in the values of the EFG for different model parameters reflect the corresponding deviations of the core configurations. The EFG is very sensitive to small changes in the positions of the ionic rows.

In addition, the calculations show that the EFG of a screw dislocation decreases rapidly with increasing distance from the dislocation line ($|V_{zz}|\approx 10^{-2}V/b^2$ for $r\approx 10a$). This is in good agreement with the result to be expected in the elastic region, where for the given orientation $h_1=h_2=0$ and the EFG must vanish, because in this case $f_S(\theta,h_i)=0$. Compared with the EFG for the screw dislocation, the EFG in the case of the edge dislocation always has larger absolute values. This is in accordance with the fact that the elastically calculated EFG for the edge dislocation is different from

Table 3

Atomistically calculated EFG at cation sites within the core of a $\langle 1\bar{1}0\rangle(110)$ screw (S) and edge (E) dislocation, respectively. z axis of the coordinate system is parallel to the dislocation line, external field parallel to ⟨110⟩. All distances in units of cation-anion distance a. (BMH Born-Mayer-Huggins repulsive potential, BP Born-Pauling repulsive potential, VDW van der Waals potential, E_1 isotropic linear elastic boundary conditions, E_2 anisotropic linear elastic boundary conditions.)

Position		EFG(V/b^2)		Screw dislocation	
x_S	y_S	BMH+VDW E_2	BP+VDW E_2	BMH E_2	BMH E_1
$-\frac{1}{4}2^{1/2}$	−1.5	0.922	1.347	0.888	0.742
$-\frac{3}{4}2^{1/2}$	−0.5	−3.290	−1.544	−3.645	−3.890
$+\frac{1}{4}2^{1/2}$	−0.5	−6.127	−4.028	−6.447	−6.700
$+\frac{3}{4}2^{1/2}$	−0.5	−1.594	−0.943	−1.704	−1.994

	EFG(V/b^2)			Edge dislocation	
$x_E y_E$	BMH I E_1	BP I E_1	BP I+VDW E_1	BMH III+VDW E_1	BMH III+VDW E_2
−2, −1	−5.152	−5.006	−5.511	−4.754	−4.741
−1, −2	5.811	5.949	6.044	5.986	5.976
−1, 0	6.505	6.395	6.382	6.404	6.296
+1, −2	15.35	15.19	15.06	14.65	14.65
+1, 0	19.88	19.72	17.78	19.64	19.68
+2, −1	1.800	1.699	0.598	1.408	1.559

zero, while for the screw dislocation for the chosen orientation the EFG vanishes identically.

3.2. Influence of the quadrupole perturbation on the NMR signal

The electric field gradients V_{zz} in the neighbourhood of a dislocation as calculated in the last section are associated with a quadrupole distortion frequency $\omega_Q(m)$ according to eq. (12). A given distribution of dislocations results in a corresponding distribution of quadrupole frequencies which may be described by an inhomogeneous line broadening function $g_Q^m(\omega)$ as discussed in detail in the forthcoming section.

In general the shape $g(\omega)$ of the NMR wide-line signal of nuclei with half-integral spin $I>\frac{1}{2}$ resulting from n mutually independent line broadening effects, each of which is characterized by a normalized distribution function $g_i(\omega)$, can be written as

$$g(\omega)=\sum_{m=-I}^{I-1} c_m[g_1^m(\omega)\oplus g_2^m(\omega)\oplus\cdots\oplus g_n^m(\omega)], \tag{47}$$

with

$$\int_{-\infty}^{+\infty} g(\omega)\,d\omega=1,$$

where c_m is the relative transition probability $m \rightarrow m+1$

$$c_m = \frac{I(I+1)-m(m+1)}{\sum_{m=-I}^{I-1}[I(I+1)-m(m+1)]},$$

and $\oplus$ stands for the convolution operation. It has to be noted that in fact most of the nuclei which are of interest as probes for studying quadrupole effects in solids have a half-integral spin $I > \frac{1}{2}$.

In the case of a rigid cubic lattice distorted by dislocations together with an external uniaxial stress, the distribution functions $g_i^m(\omega)$ are given by:

(1) the magnetic dipole interaction of nuclear spins, which is independent of the spin quantum number m: $g_1^m(\omega) = g_D(\omega)$;

(2) the electric quadrupole interaction between the nuclear quadrupole moment Q and the local EFG given by the dislocations:

$$g_2^m(\omega) = g_Q^m(\omega) = g_Q[(2m+1)a];$$

(3) the electric quadrupole interaction between the quadrupole moment Q and the constant EFG caused by the external stress σ_0:

$$g_3^m(\omega) = \delta[\omega - \omega_Q^m(\sigma_0)] = \delta[\omega - (2m+1)a(\sigma_0)]. \tag{48}$$

Using the symmetry relation $c_m = c_{-(m+1)}$ and remembering that in first order $a(-\frac{1}{2} \rightarrow +\frac{1}{2}) \equiv 0$, eq. (47) may be written as:

$$g(\omega) = c_{-\frac{1}{2}} g_D(\omega) + \sum_{m=+\frac{1}{2}}^{I-1} 2c_m g_D(\omega) \oplus g_Q\{(2m+1)[a-a(\sigma_0)]\}. \tag{49}$$

On the other hand, the time response function of the nuclear magnetization [often called free induction decay (FID)] $F(t)$ following an on-resonance rf pulse of length $\delta t = \frac{1}{2}\pi/(\gamma H_1)$ (H_1: strength of the corresponding magnetic rf field) is generated by a Fourier transform of the NMR signal $g(\omega)$ [114]. Therefore $F(t)$ is given by:

$$F(t) = c_{-1/2} D(t) + \sum_{m=+\frac{1}{2}}^{I-1} 2c_m D(t) Q_m(t) \cos[(2m+1)a(\sigma_0)t], \tag{50}$$

where

$$D(t) = \int_{-\infty}^{+\infty} g_D(\omega) \cos \omega t \, d\omega; \qquad D(0) = 1, \tag{51a}$$

and

$$Q_m(t) = \int_{-\infty}^{+\infty} g_Q(a) \cos[(2m+1)at] \, da; \qquad Q_m(0) = 1, \tag{51b}$$

are the Fourier cosine transformations of the corresponding distribution functions $g(\omega)$.

Experimentally, the observation of the total free induction decay is often complicated because of the finite dead time of the receiver of the NMR spectrometer.

On applying a second rf pulse following the first $\pi/2$ pulse after a time $\tau > t_s$ (the half width of the FID), multiple spin-echo signals are observed [114–120].

Especially, the main echo $E(t')$ at time $t' = t + 2\tau$ has a form very similar to eq. (50) ([103], p. 12):

$$E(t') = C_{-1/2}(I) D^*(t') + \sum_{m=+\frac{1}{2}}^{I-1} 2C_m(I) D^*(t') Q_m(t') \cos[(2m+1)a(\sigma_0)t'], \tag{52}$$

where $D^*(t')$ denotes a modified dipolar function. The coefficients $C_m(I)$ depend on the spin quantum number I and on the rotation angle $\beta = \gamma H_1 \delta t_2$ of the second rf pulse, and are calculated by Mehring and Kanert [121]. The maximum echo height is obtained for an optimum rotation angle β_{opt}. Values for β_{opt} together with the corresponding values for $C_m(I)$ are listed in table 4.

Table 4
Spin echo signal parameters

Spin I	$\frac{3}{2}$	$\frac{5}{2}$	$\frac{7}{2}$	$\frac{9}{2}$
β_{opt}	64°	40°	30°	24°
$C_{-1/2}(\beta_{opt})$	0.366	0.247	0.190	0.153
$2C_m(\beta_{opt}) \mid m = \frac{1}{2}$	0.634	0.469	0.362	0.294
$m = \frac{3}{2}$	-	0.284	0.297	0.266
$m = \frac{5}{2}$	-	-	0.151	0.201
$m = \frac{7}{2}$	-	-	-	0.089

As discussed above; the dipolar part $D(t)$ in eq. (50) is due to the magnetic dipole interaction of the nuclear spins and can be expressed to a good approximation by a modified Gaussian function [122, 123]:

$$D(t) = \exp(-\tfrac{1}{2}c_1^2 t^2) \sin(c_2 t)/c_2 t. \tag{53}$$

The coefficients c_1 and c_2 are related to Van Vleck's second and fourth dipolar moments, Δ^2 and Δ^4 [124], by the equations

$$\Delta^2 = c_1^2 - \tfrac{1}{3}c_2^2 \qquad \text{and} \qquad \Delta^4 = 3c_1^4 + 2c_1^2 c_2^2 + \tfrac{1}{5}c_2^4.$$

For many purposes one can assume that $D(t)$ is roughly approximated by a Gaussian function of the form:

$$D(t) \simeq \exp(-\tfrac{1}{2}\Delta^2 t^2), \tag{54}$$

and consequently

$$g_D(\omega) = \frac{1}{(2\pi)^{1/2}} \frac{1}{\Delta} \exp(-\omega^2/2\Delta^2). \tag{55}$$

Furthermore, a theoretical expression for the modified dipolar function $D^*(t)$ in eq. (52) does not exist, since up to now the problem of refocusing of spins under the influence of the total dipolar and quadrupolar Hamiltonian is unsolved. However, line-shape analyses of measured spin-echo signals $E(t^*)$ show that in all practical cases $D^*(t)$ can be described by $D(t)$ in a good approximation [125]. Supposing also a

Gaussian shape for the quadrupolar broadening function

$$g_Q(a)=\frac{1}{(2\pi)^{1/2}}\frac{1}{\langle a^2\rangle^{1/2}}\exp(-a^2/2\langle a^2\rangle), \qquad (56)$$

with $\langle a^2\rangle$ being the second moment of $g_Q(a)$ and assuming $a(\sigma_0)=0$, one can calculate

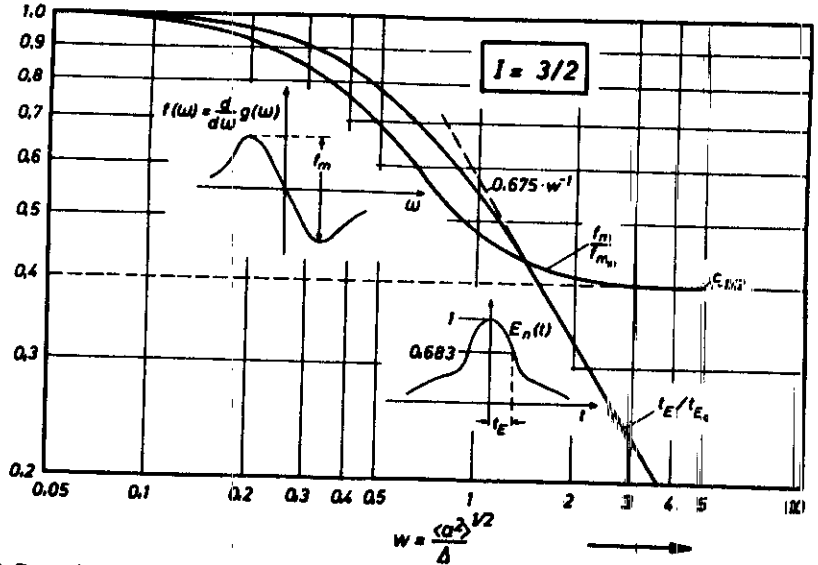

Fig. 8. Dependence of the peak intensity f_m/f_{m_0} of the wide-line signal and the spin-echo half width t_E/t_{E_0} on the normalized quadrupole perturbation ω for spin $I=\frac{3}{2}$ [136].

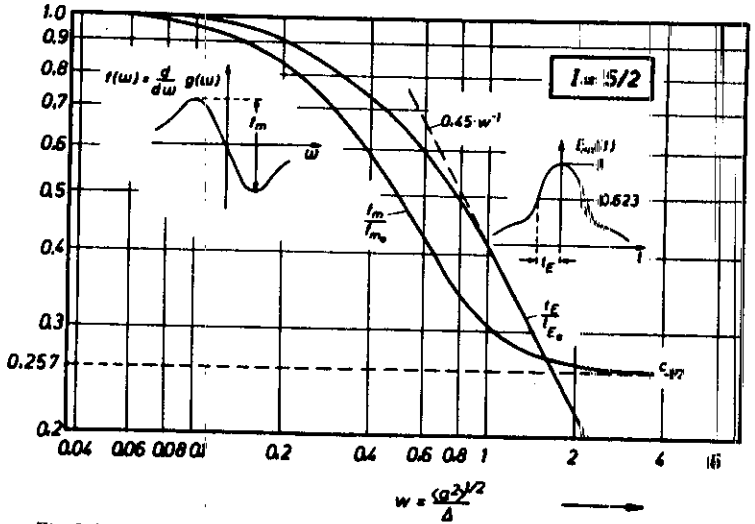

Fig. 9. NMR line parameters as given in fig. 8 in the case of spin $I=\frac{5}{2}$ [103].

the dependence of defined signal parameters of the wide-line signal $g(\omega)$ and of the spin-echo signal $E(t^*)$ on the normalized mean quadrupole distortion $w=\langle a^2\rangle^{1/2}/\Delta$. Starting from the derivative $f(\omega)=d/d\omega g(\omega)$ which is actually recorded in wide-line experiments, the relative peak intensity f_m/f_{m_0} of $f(\omega)$ is the usual parameter in such experiments. On the other hand, in spin-echo experiments it is more effective to measure the width of the echo signal. Therefore, Kanert and Mehring [103, p. 17] have introduced a spin-dependent width t_E of the echo which has been shown to be most sensitive against a change in quadrupole distortion.

Results of such calculations are shown in figs. 8 and 9 in the cases of spins $I=\frac{3}{2}$ and $\frac{5}{2}$. The insets in the figures give the exact definition of the echo width t_E for both cases.

Furthermore, as described by eq. (49), a finite uniaxial stress σ_0 induces satellite lines at the frequency position $(2m+1)a(\sigma_0)$ in the wide-line signal $g(\omega)$. An example is shown in fig. 10 for the case of NaCl loaded with an external stress σ_0 as given by

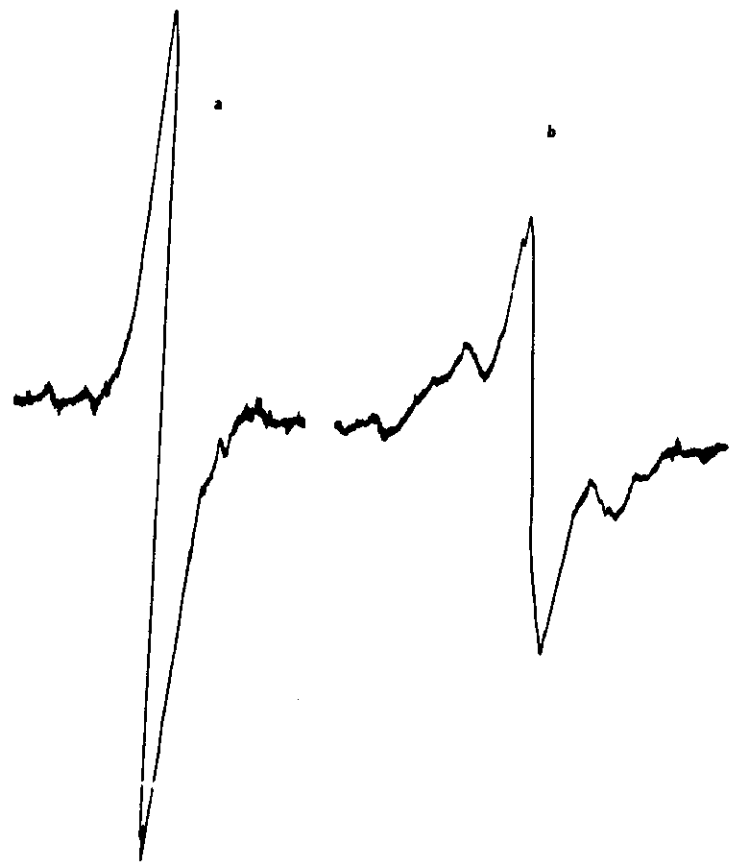

Fig. 10. Derivatives of $f(\omega)$ of the wide-line signal $g(\omega)$ of ^{35}Cl in an undeformed (a) and an elastically deformed (b) NaCl single crystal ($\sigma_0=3\times10^7$ dyn cm^{-2} along the ⟨111⟩ axis) [126].

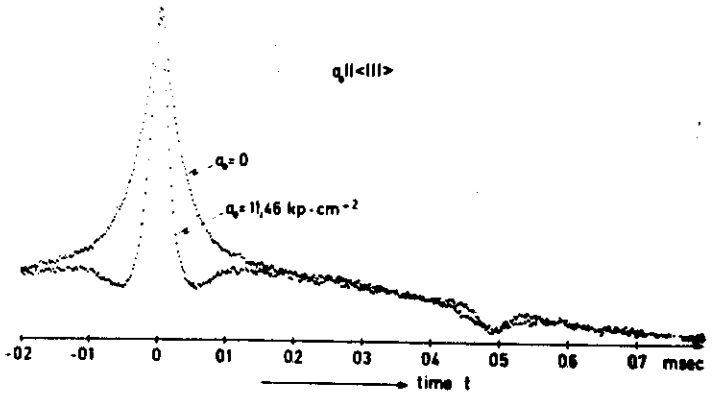

Fig. 11. Spin-echo signal of ^{127}I in an unloaded ($\sigma_0 = 0$) and an elastically deformed ($\sigma_0 = 11.24 \times 10^6$ dyn cm^{-2} along the ⟨111⟩ axis) RbI single crystal, showing the reversible narrowing of the echo signal due to an external uniaxial stress σ_0. The signal at $t = 0.5$ ms is the allowed 3τ-echo [115].

Bogdanov and Lemanov [126]. Corresponding to the splitting of the wide-line signal $g(\omega)$, the free induction decay $F(t)$ eq. (50) as well as the spin-echo signal $E(t')$ eq. (52) given by the Fourier transform mechanism are modulated with the frequency $(2m+1)a(\sigma_0)$. The beginning of such modulation of a ^{127}I echo signal in an elastically deformed RbI single crystal is demonstrated in fig. 11. The gradient-elastic constants based on such experiments are listed in table 2 under the abbreviation "ES".

Before concluding this section it is noteworthy that the assumption of a Gaussian line shape for the quadrupolar function $g_Q(a)$ as formulated in eq. (56) is quite arbitrary. Indeed, quadrupolar broadening functions as given by dislocations will be presented in detail in the forthcoming section. Nevertheless, to get a feeling for the behaviour of the NMR signal influenced by static quadrupole distortions as demonstrated in figs. 10 and 11, it is legitimate to introduce such a simple analytical expression for $g_Q(a)$.

3.3. Quadrupolar distribution function for dislocations

In order to calculate the quadrupole broadening function $g_Q(a)$ and the corresponding time function

$$Q(t) = \int_{-\infty}^{+\infty} g_Q(a)\cos(at)\,\mathrm{d}t$$

due to the distribution of the quadrupole frequencies, one has to take into account the density and arrangement of the dislocations in the sample. It is obvious that any change in the arrangement of the dislocations in the crystals results in a change of the broadening function $g_Q(a)$. Vice versa, a measured broadening function $g_Q(a)$ may be associated with different densities and arrangements of dislocations. Up to now, only the simple model of a network of randomly distributed, parallel dislocations of

density ρ has been used for a detailed calculation of $g_Q(a)$. In this case, following the treatment given by Cohen and Reif [108] and Stoneham [127], the broadening function can be obtained by a random-walk theory. They have shown that in general the time function $Q(t)$ can be written as

$$Q(t) = \prod_{j=1}^{N} c_j \exp(i a_j t). \tag{57}$$

Here c_j is the probability that a lattice defect is on site j and a_j is the quadrupole distortion frequency of a given nucleus due to the defect on the jth lattice site. It should be remarked that in the case of the random distribution of defects discussed here c_j is independent of j and denotes the concentration c of the defects.

The linear term of the series vanishes in the case of a large defect concentration c where each nucleus is perturbed by a sufficient number of defects. Introducing the second moment

$$\langle a^2 \rangle = c \sum_{j=1}^{N} a_j^2, \tag{58}$$

and neglecting terms higher than quadratic in the expansion, eq. (57) may be written as:

$$Q(t) \simeq \exp(-\langle a^2 \rangle t^2/2). \tag{59}$$

This result is known as the *central limit theorem*. The Fourier transform of eq. (59) leads to the distribution function $g_Q(a)$ assumed in eq. (56). To calculate the response function $Q(t)$ for small defect concentrations one has to bear in mind that each defect produces in first order at a given nucleus an antisymmetrical set of quadrupole frequencies as described by eq. (12). Therefore, eq. (57) may be written as:

$$Q(t) = \prod_{j=1}^{N} c_j \cos a_j t = \prod_{j=1}^{N} [1 - 2c_j \sin^2(a_j t/2). \tag{60}$$

Using the approximation $\ln(1-x) \simeq -x$ one has

$$\ln Q(t) = -2 \sum_{j=1}^{N} c_j \sin^2(a_j t/2). \tag{61}$$

Restricting the sum over the lattice sites j to the core region of the defect and replacing the sum by a space integral outside the core, the time function can be written as:

$$Q(t) = \exp\left[-2c \left(\sum_{\substack{j=1 \\ (r_j \leqslant r_c)}}^{N_c} \sin^2(a_j t/2) + \int_{\mathrm{vol}} \sin^2(a(r)t/2)\mathrm{d}v \right) \right], \tag{62}$$

where r_c represents the core radius.

According to eqs. (12), (26), (27) and (41) for a dislocation (either screw or edge) the mean strain-induced quadrupole frequency a_j of a nucleus at distance r_j from the dislocation line can be expressed approximately by:

$$a_j = A_{S,E} f_{S,E}(\theta, h) \begin{cases} 1/r & r > r_c \\ f(r_j) & r_j \leqslant r_c \end{cases}, \tag{63}$$

where

$$A_{S,E}=\frac{3eQ}{4I(2I-1)\hbar}\,\frac{K_{S,E}bC_{11}}{2\pi}. \tag{64}$$

Then for a network of randomly distributed parallel dislocations the semi-discrete approximation of the time function $Q(t)$ has the form:

$$Q(t)=\exp\left[-\rho\left(2d_0^2\sum_{j=1}^{N_c}\sin^2\{[\tfrac{1}{2}A_{S,E}f_{S,E}(\theta,h)]f(r_j)t\}\right.\right.$$
$$\left.\left.+\frac{A_{S,E}^2}{2}t^2\int_0^{2\pi}\int_{x_0\to 0}^{x_c}\frac{\sin^2[xf_{S,E}(\theta,h)]}{x^3}\,d\theta\,dx\right)\right], \tag{65}$$

Where $x=A_{S,E}t/2r$, ρ is the dislocation density, d_0 is the nearest neighbour distance, and the sum has to be restricted to nuclei inside a plane orthogonal to the z axis of the core cylinder where: $0\leqslant\theta<2\pi$; $0<r_j\leqslant r_c$. Since the integral diverges logarithmically for x_0 approaching zero, i.e. $r\to\infty$, one has to introduce an upper value r_0 for the distance r defined by the relation

$$r_0=2.5(\pi\rho)^{-1/2}. \tag{66}$$

This is approximately the mean distance between the dislocations.

In most cases, a continuum approximation to eq. (65) together with an average orientation function $\langle f_{S,E}^2\rangle$ is sufficient for describing the response function $Q(t)$ [113]. Carrying out the integration over the angle θ and introducing the normalized time

$$\tau=1.25A_{S,E}(\pi\rho)^{1/2}t=Bt, \tag{67}$$

eq. (65) leads to the normalized form of $Q(t)$ in a continuum approximation:

$$Q(\tau)=\exp\left[-\left(\frac{\tau}{1.25}\right)^2\int_{0.16\tau}^{\infty}\frac{\sin^2x}{x^3}\,dx\right]. \tag{68}$$

A plot of $Q(\tau)$ is shown in fig. 12, demonstrating a behaviour similar to a Gaussian function. Therefore, in a first approximation, instead of eq. (68) the analytical expression of eq. (56) may be used. The normalized half width $\tau_{1/2}$ (dimensionless) is correlated to the real half time $t_{1/2}$ of the time function $Q(t)$ by

$$\tau_{1/2}=0.70=1.25A_{S,E}(\pi\rho)^{1/2}t_{1/2}. \tag{69}$$

The corresponding plot of the normalized distribution function $g_Q(s)$ calculated by a Fourier transformation of eq. (68) is presented in fig. 13 as a function of the normalized frequency $s=(1/B)\omega$.

In order to verify the theoretical expression for the dislocation-induced quadrupole broadening function g_Q, spin-echo measurements were performed in ultra-pure, plastically deformed non-metallic (NaCl) and metallic (Al) samples. As described above, from the measured echo signal $E(t')$ the response function $Q(t')$ and via a Fourier transform the corresponding broadening function $g_Q(\omega)$ can be obtained. Results of such measurements are shown in fig. 14a for ^{23}Na in NaCl and in fig. 14b

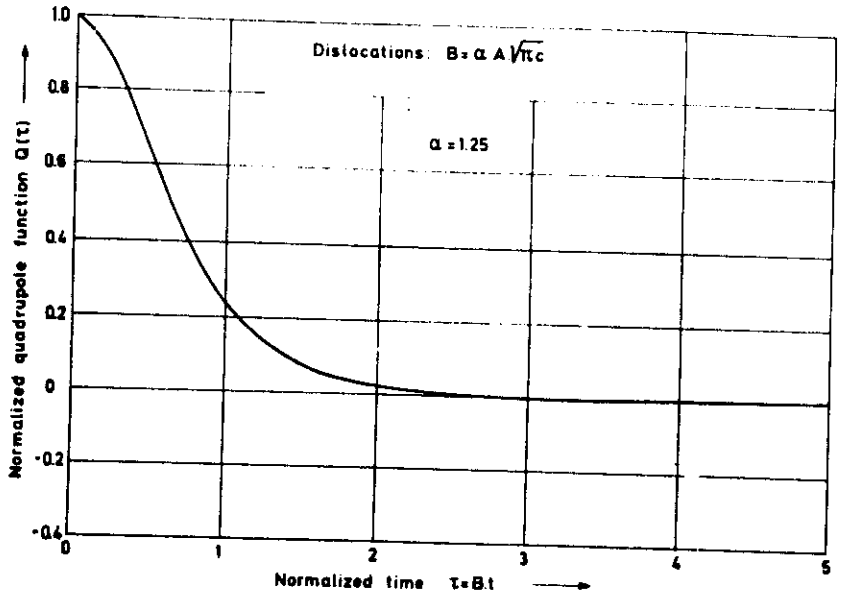

Fig. 12. Theoretical normalized quadrupole function $Q(\tau)$ versus normalized time τ. Note that the slope is finite at $\tau=0$ [103].

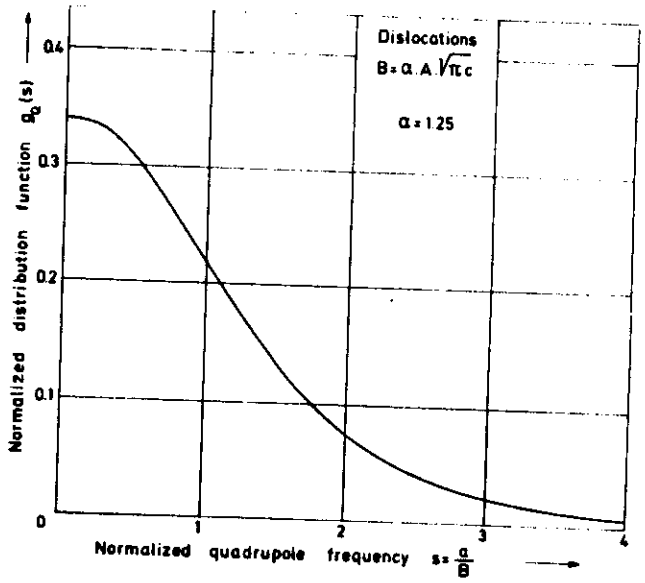

Fig. 13. Theoretical normalized distribution function $g_Q(s)$ versus normalized quadrupole frequency s [103].

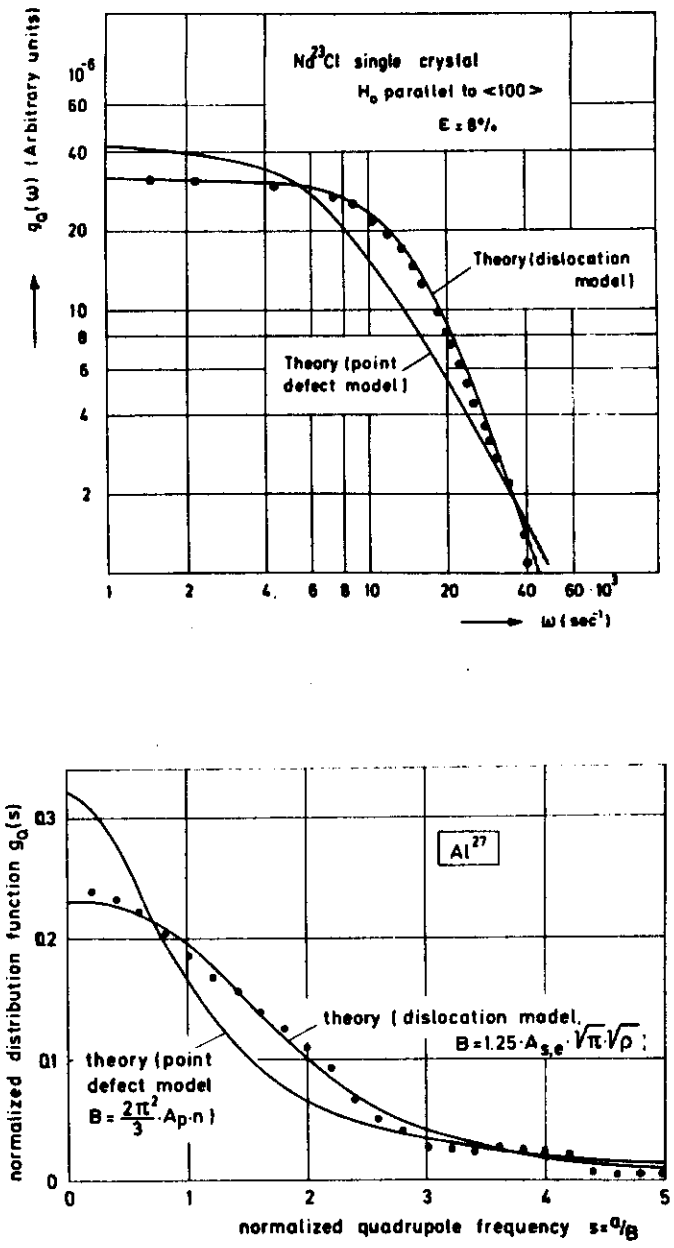

Fig. 14. Comparison of the measured distribution function (dots) and the theoretical distribution functions $g_Q(\omega)$ for dislocations and for point defects (spin $I = \frac{3}{2}$). The experimental values are obtained from NMR wide-line signals by a numerical deconvolution procedure: (a) deformed ^{23}NaCl single crystal and (b) deformed Al crystal [103].

for ^{27}Al in aluminium. For comparison, the theoretical quadrupole functions due to a broadening mechanism of point defects are inserted into the figures. Both the plots demonstrate clearly that the dislocation-induced distribution function g_Q fits the experimental data, in sharp contrast to the broadening function caused by point defects.

3.4. Effect of dislocation density on the NMR signal

In ultra-pure crystals, lattice distortions are mainly produced by dislocations. In this case, the resulting quadrupole broadening of the NMR signal is determined by the total density ρ_t of the dislocations. The broadening may be described by the half width $a_{1/2}$, the absolute first moment $\langle|a|\rangle$ or the square root of the second moment $\langle a^2\rangle^{1/2}$ of the distribution function $g_Q(a)$.

In all the cases the broadening is proportional to the parameter B in eq. (67), i.e. to the square root of the total dislocation density ρ_t. Hence, together with eq. (12)

$$\langle\omega_Q^2\rangle = A\rho_t, \tag{70}$$

with $A = \alpha\pi^2 A_{S,E}^2 \langle f_{S,E}^2\rangle$ and α being a factor of the order of one. For a more precise discussion, one has to take into account that the densities of screw and of edge dislocations are different for different slip systems. With a_S^i and a_E^i being the relative abundances of screw (density ρ_S^i) and edge dislocation (density ρ_E^i) in the ith slip system of the lattice, the quadrupole second moment can be written as

$$\langle\omega_Q^2\rangle = \alpha\pi^2\left(A_S^2\sum_i a_S^i\langle f_S^2(\boldsymbol{h})\rangle^i\rho_S^i + A_E^2\sum_i a_E^i\langle f_E^2(\boldsymbol{h})\rangle^i\rho_E^i\right) \tag{71}$$

From the orientation dependence of the functions $\langle f^2(\boldsymbol{h})\rangle^i$ an orientation dependence of $\langle\omega_Q^2\rangle$ is expected in general [103]. Based on these concepts, dislocation densities on different planes can be measured as shown by Alsem and De Hosson [218].

4. *Nuclear spin relaxation theory adapted for dislocation motion*

4.1. Motion-induced spin–lattice relaxation

While static quadrupolar effects associated with static lattice defects such as dislocations are analyzed in terms of width, line shape, and intensity of the NMR signal, *dynamical* effects originating from time-dependent quadrupolar interactions due to the motion of defects, such as the long-range migration of a dislocation during plastic deformation, are studied through the related nuclear spin-lattice relaxation process.

Following the sudden application of a static magnetic field $\boldsymbol{H}$ to an unmagnetized diamagnetic sample, the exchange of energy between the nuclear spin system and the non-spin degrees of freedom (the "lattice") may be detected via the evolution of the nuclear magnetization $\boldsymbol{M}(t)$ towards its equilibrium value $\boldsymbol{M}_0$. Typically, this relaxa-

tion process follows a simple relationship [89]

$$\dot{M}(t) = -\frac{1}{T_1}[M(t) - M_0], \tag{72}$$

where M_0 is governed by Curie's law and T_1 is called the spin–lattice relaxation time. The relaxation process is due to a weak time-dependent interaction, described by a spin–lattice Hamiltonian $\hat{H}_{SL}(t)$ between the strongly coupled spins with a Hamiltonian $\hat{H}_S$ and the "lattice" with a Hamiltonian $\hat{H}_L$, and is caused by phenomena such as atomic, defect, and electronic motion. Consequently, the total Hamiltonian of the sample is given by

$$\hat{H} = \hat{H}_S + \hat{H}_L + \hat{H}_{SL}(t), \tag{73}$$

where $\hat{H}_{SL}(t)$ commutes neither with $\hat{H}_L$ nor with $\hat{H}_S$, but $[\hat{H}_S, \hat{H}_L] = 0$. The corresponding thermodynamic picture based on a quantum-statistical description [140] is shown in fig. 15. In the figure, the sample is decomposed into a spin system and a lattice heat reservoir characterized by a temperature $\beta = 1/kT$ and a heat capacity [141]. Independent of the special types of relaxation theory given in the literature, the following fundamental physical assumptions have been incorporated into all these theories:

(1) The general starting Hamiltonian is assumed to be of the type given in eq. (73).
(2) The heat capacity of the lattice is assumed to be infinitely large and therefore $\beta_L = \text{constant}$.
(3) The spacing of the energy levels associated with the spin Hamiltonian $\hat{H}_S$ is assumed to be much smaller than the thermal energy β_L^{-1} ("high-temperature approximation").
(4) The small size of $\hat{H}_{SL}$ with respect to $\hat{H}_S$ allows the use of first-order perturbation theory to calculate the "lattice"-induced transition probabilities, i.e. the relaxation rates.

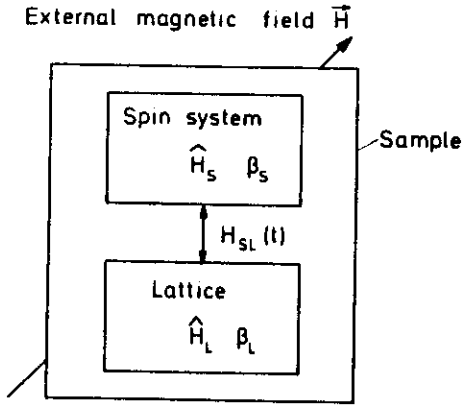

Fig. 15. Schematic representation of spin–lattice relaxation.

(5) Because of the use of perturbation theory the observation time has to be large compared with the correlation time of $\hat{H}_{SL}(t)$.
(6) $\hat{H}_{SL}(t)$ is assumed to be a random operator, the correlation function

$$\langle \hat{H}_{SL}(t')\hat{H}_{SL}(t'+t)\rangle_{t'} = \lim_{t'\to\infty}\frac{1}{t'}\int_0^{t'} d\tau \hat{H}_{SL}(\tau)\hat{H}_{SL}(\tau+t) \tag{74}$$

of which is assumed to be stationary, i.e. independent of a shift of the time scale.
(7) The spins are assumed to be strongly coupled, leading to a common spin temperature β_S.

Then, by applying second-order perturbation theory, the "golden rule of quantum mechanics" leads to the relaxation rate [140]

$$\frac{1}{T_1} = \frac{2}{\hbar^2}\,\mathrm{Re}\int_0^\infty dt' \,\overline{\langle a|\hat{H}^*_{SL}(t')|b\rangle\langle b|\hat{H}^*_{SL}(0)|a\rangle}. \tag{75}$$

Here the bar indicates the average over the spin ensemble and $\hat{H}^*_{SL}$ denotes the interaction representation of $\hat{H}_{SL}$ defined by

$$\hat{H}^*_{SL}(t) = e^{iH_Z t/\hbar}\,\hat{H}_{SL}(t)\,e^{-iH_Z t/\hbar} \tag{76}$$

where $\hat{H}_Z$ is the Zeeman operator which determines the precession frequency $\omega_0 = \gamma H$ of the spins (γ: gyromagnetic ratio). To relate the spin–lattice relaxation rate in eq. (75) to the motion of defects in the lattice, one has to remember that the general mathematical structure of $\hat{H}_{SL}$ is given by a product of a spin-operator part $\hat{Q}$ and a "lattice" function $F[r(t)]$ as shown by eq. (11) in the case of a quadrupolar interaction. In the usual semiclassical approximation the spin-operator part is treated quantum mechanically while the lattice function $F(t)$ is assumed to form a classical correlation function

$$G(t) = \frac{1}{N}\sum_{j,k=1}^{N}\langle F_{jk}(t')F^+_{jk}(t+t')\rangle_{t'}, \tag{77}$$

where the ensemble average in eq. (75) is replaced by a time average. Defining the spectral density

$$J(\omega) = \int_{-\infty}^{+\infty} G(t)\,e^{i\omega t}\,dt, \tag{78}$$

one obtains as a general expression for the spin–lattice relaxation rate

$$1/T_1 = f(I)J(\omega_0), \tag{79}$$

where the factor $f(I)$ is determined by the quantum-mechanical treatment of $\hat{Q}$. Next, the spectral density function has to be related to the motion of the defects, requiring the calculation of the correlation function $G(t)$ for a given mechanism of motion. As discussed first by Bloembergen et al. [142], it is quite reasonable for a typical motional process to let $G(t)$ have the functional form

$$G(t) = \langle F(0)^2\rangle\, e^{-|t|/\tau_c}, \tag{80}$$

where

$$\langle F(0)^2\rangle = \frac{1}{N}\sum_{j,k}^{N} F^2$$

and τ^{NMR} denotes the mean time between consecutive changes in $\hat{H}_{SL}(t)$, i.e. the "NMR correlation time". It is important to recognize that in general τ^{NMR} differs from the "mean jump time" τ of the lattice defects. For instance, it is obvious that, in the case of the motion of a defect pair $(j-k)\tau^{NMR} = \frac{1}{2}\tau$, since whenever j or k performs a jump the operator $\hat{H}^{jk}_{SL}(t)$ will fluctuate. However, it will be shown in the forthcoming sect. 4.3 that for motion of a dislocation the relation $\tau^{NMR} = \tau$ is valid.

Hence, carrying out the Fourier transformation of eq. (80), the relaxation rate $1/T_1$ [eq. (79)] may be expressed as

$$\frac{1}{T_1} \simeq \langle\omega^2_{SL}(0)\rangle \frac{\tau^{NMR}}{1+(\omega_0\tau^{NMR})^2}, \qquad \text{(81)}$$

where $\langle\omega^2_{SL}\rangle$ is determined by $\hat{H}_{SL}$ and describes the strength of the coupling between the "lattice" and the spin system which acts as a probe for the motion of defects. It has to be noticed that eq. (81) is only a rough approximation, but nevertheless the relation is a fair basis for describing the general important trends in a motion-induced relaxation process.

The basic results of eq. (81) with respect to magnetic relaxation spectroscopy are illustrated in fig. 16, and are as follows:

(1) At $\tau^{NMR} = 1/\omega_0$, the relaxation rate $1/T_1$ goes through a maximum, offering a direct possibility of determining the NMR correlation time τ^{NMR}. Since it is possible experimentally to change the precession frequency ω_0 over a very large range between about 10^{-8} s. (Zeeman-relaxation in the strong static field) and 10^{-3} s. (relaxation in the local fields of the spins), τ^{NMR} can be measured over a large time scale. Especially if the internal motions are rather slow, as in the case of dislocation motion, the process of motion has to be followed by means of a special type of relaxation spectroscopy, namely the spin-locking relaxation technique. In this technique, the related spin–lattice relaxation rate in the rotating frame, $1/T_{1\rho}$, is observed at a

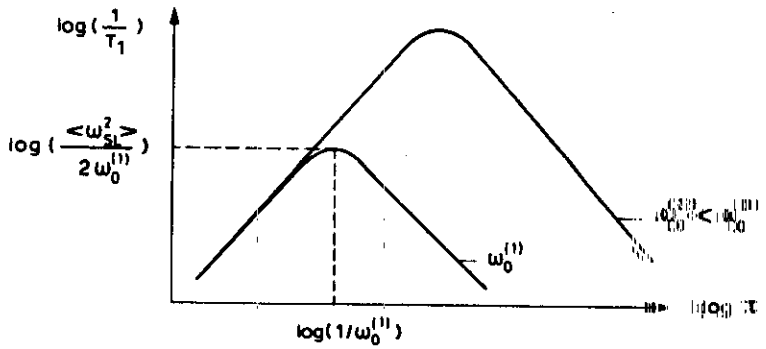

Fig. 16. Motion-induced spin–lattice relaxation.

very low precession frequency determined by the strength of the rf field. Details of the technique and the relaxation theory will be discussed in the two following sections.

(2) Lowering of the precession frequency ω_0 results in an increase of the relaxation rate according to:

$$(1/T_1)_{max} = \langle\omega^2_{SL}\rangle/2\omega_0. \qquad \text{(82a)}$$

(3) For $\omega_0\tau \ll 1$, the relaxation rate $1/T_1$ is equal to the NMR correlation time τ^{NMR} scaled by the strength of the spin-lattice coupling $\langle\omega^2_{SL}(0)\rangle$:

$$1/T_1 = \langle\omega^2_{SL}(0)\rangle\tau^{NMR}. \qquad \text{(82b)}$$

(4) For the ultra-slow motions, where $\omega_0\tau \gg 1$ the relaxation rate $1/T_1$ is proportional to the inverse of the NMR correlation time τ^{NMR} and depends inversely on the square of the precession frequency ω_0:

$$1/T_1 = \langle\omega_{SL}(0)\rangle/\omega_0^2\tau^{NMR}. \qquad \text{(82c)}$$

It should be noticed at this point that most of the relaxation measurements carried out for studying dislocation motion are governed by a relation of type (82c). This will be shown in detail in sect. 5.

4.2. The spin-locking experiment

As shown by Redfield [143], the spin system under the effect of a strong rf irradiation leading to a rotating magnetic rf field may be treated in a manner which is formally identical to the treatment of the spin system exposed to a time-independent static magnetic field. The key factor of the formal equivalence lies in the transformation of $\hat{H}_S$ into a reference frame (x, y, z) parallel to the external field which rotates with the frequency of the rf field.

Experimentally, as shown in fig. 17, a 90° pulse with an rf field H_1 along the x axis rotates the nuclear magnetization M from the direction of the static magnetic field to the y direction. As soon as the pulse is completed the phase of the rf field H_1 is changed by $\pi/2$, so that H_1 also now lies along the y axis. Since H_1 and M are collinear, no torque is exerted on M, and M remains along the y axis. The sample magnetization is called "spin-locked" in the rotating frame. In the rotating frame, H_1 plays the role of a time-independent field. Consequently, the rotating magnetization relaxes parallel to the locking field H_1 towards its equilibrium value characterized by a relaxation time, usually called the relaxation time in the rotating frame, $T_{1\rho}$. Clearly, $T_{1\rho}$ must be closely related to T_1, the relaxation time in a static magnetic field (determined by a precession frequency $\omega_1 = \gamma H_1$). To measure the relaxation time $T_{1\rho}$, the nuclear magnetization is allowed to decrease in the presence of the locking field H_1 for some time τ, then H_1 is turned off and the initial height of the free induction decay $F(\tau)$ is noted. After repetition of the process for other values of τ, a plot of $\log F(\tau)$ vs τ gives a straight line with a slope $1/T_{1\rho}$.

It should be mentioned that it is possible to turn the locking field H_1 off and (just before time τ) on again adiabatically in order to perform a nuclear relaxation process

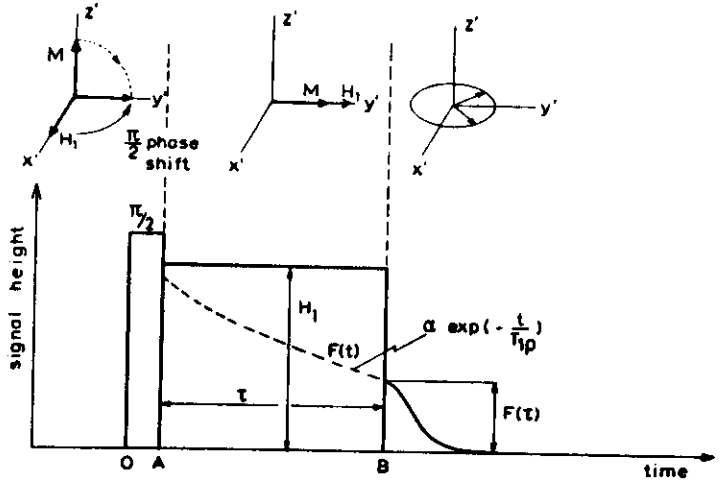

Fig. 17. Spin-locking experiment and free induction decay.

with a precession frequency ω_0 determined by the local magnetic field H_{loc} of the spins: $\omega_{loc}=\gamma H_{loc}$. The technique is called "adiabatic demagnetization in the rotating frame" (ADRF) in the literature [144]. In the ADRF state, the net magnetization is zero, i.e. the order of the spin system is transferred from the Zeeman alignment to a local spin alignment within the nuclear dipole fields. Hence the relaxation process is determined by the corresponding precession frequency in the local dipolar field: $\omega_{loc}=\gamma H_{loc}$.

4.3. Spin relaxation due to dislocation motion

As discussed in sect. 3, in cubic crystals electric field gradients at the nuclear positions are due to the stress fields of lattice defects such as dislocations. Whenever a dislocation changes its position in the crystal, the surrounding atoms have also to move, thus causing time fluctuations both of the quadrupolar and dipolar spin Hamiltonian for spins with $I>\frac{1}{2}$. However, as verified by Hut [145] and theoretically confirmed by Wolf and Kanert [146], the dipolar effects on the nuclear spin relaxation due to dislocation motion are negligible, and quadrupolar interactions dominate the observed relaxation behaviour. Therefore in this section we shall concentrate exclusively on the effect of quadrupolar fluctuations on the nuclear spin relaxation due to the motion of dislocations.

Furthermore, for the investigation of rather infrequent defect motions as in the case of moving dislocations, the spin–lattice relaxation time in the rotating frame $T_{1\rho}$ has proved to be the most appropriate NMR parameter affected by such motions. In reviewing the basic expressions for $T_{1\rho}$ due to time fluctuations of quadrupolar interactions, we limit ourselves to the case in which (i) all N spins of the sample are identical and (ii) the rotating locking field H_1 is applied at the exact resonance-

precession frequency $\omega_0=\gamma H_0$ of the spins, H_0 being the static external magnetic field.

For a comprehensive discussion we start with the general relation for $T_{1\rho}$ due to quadrupolar fluctuations as derived by Wolf [140]

$$\frac{1}{T_{1\rho}}=\frac{\delta_Q}{H_{eff}^2}\left(\left.\frac{dG_Q(t)}{dt}\right|_{t=0}-\mathrm{Re}\int_0^\infty dt\,\frac{d^2G_Q(t)}{dt^2}\,k_Q(t)[1+\exp(j2\omega_{eff}t)]\right), \tag{83}$$

where δ_Q is defined as follows:

$$\delta_Q=\frac{3}{320}\left(\frac{eQ}{\gamma\hbar}\right)^2\frac{2I+3}{I^2(2I-1)}. \tag{84}$$

The classical quadrupolar "lattice" correlation function $G_Q(t)$ is given by

$$G_Q(t)=\frac{1}{N}\sum_{j=1}^{N}\sum_{k=1}^{N_d^{dyn}}\langle V_{kj}(t'+t)V_{kj}^*(t')\rangle_{t'}, \tag{85}$$

where N_d^{dyn} denotes the number of *mobile* defects and the angular brackets symbolize the time average over the initial time t' as introduced by eq. (74). V_{kj} represents the EFG at the site of spin j which is due to a defect k and is given by [see also eq. (18)]:

$$V_{kj}=\tfrac{1}{2}V_{zz}(k,j)(3\cos^2\theta_{kj}-1-\eta_{kj}\sin^2\theta_{kj}\cos 2\phi_{kj}). \tag{86}$$

Here $V_{zz}(k,j)$ and η_{kj} denote the magnitude and asymmetry parameter of the EFG at the position of spin j which is produced by the defect k, while θ_{kj} and ϕ_{kj} characterize the orientation of the symmetry axis of the EFG tensor associated with defect k with respect to the laboratory frame with its z axis parallel to the external magnetic field H_0.

The "quadrupolar spin-correlation function" $k_Q(t)$ describes a thermal mixing process between the nuclear spins following a dislocation jump, i.e. a distortion in $\hat{H}_{SL}$ [146]. In close analogy to the cross-relaxation process discussed by McArthur et al. [147] and Demco et al. [148] one may assume that

$$k_Q(t)\simeq\exp(-t/T_m), \tag{87}$$

where the "quadrupolar thermal mixing time" T_m is given approximately by

$$1/T_m\simeq\gamma H_{loc}\exp(-H_1/H_{loc}). \tag{88}$$

Physically, the relation demonstrates that the strength of the thermal mixing process is determined by the overlap of the nuclear energy levels in the rotating frame which is given by the magnitude of the local field H_{loc}. An increase of the level splitting by increasing the locking field H_1 leads to a decrease of the overlap, i.e. an increase in the thermal mixing time T_m. The "effective Zeeman field" H_{eff} in eq. (83) defined by

$$H_{eff}^2=H_1^2+H_D^2+(H_Q^n)^2+[1-k_Q(\tau_m)](H_Q^0)^2, \tag{89}$$

is proportional to the effective heat capacity of the spin system, i.e. the heat capacity of that part of the spin system which is able to maintain a common spin temperature (condition 7 in sect. 4.1) even during the quadrupolar fluctuations. The corresponding local fields in the rotating frame which appear in eq. (89) contain secular (0) and

nonsecular (n) contributions with respect to the Zeeman Hamiltonian in the rotating frame. τ_m denotes the quadrupolar "lattice" correlation time, i.e. the mean time between consecutive changes in EFG caused by the stress fields of mobile dislocations. (Note that the term $[1-k_Q(t_m)]$ denotes the probability that on the average quadrupolar thermal mixing takes place between consecutive changes in the EFG.) Furthermore, $\omega_{eff}=\gamma H_{eff}$ is the "effective spin precession frequency". The dipolar local field H_D in the rotating frame is connected [124] to Van Vleck's dipolar second moment Δ^2, introduced below eq. (53), by [140]

$$H_D^2=\tfrac{1}{3}\Delta^2, \tag{90}$$

while the different quadrupolar local field contributions in the rotating frame are given by

$$H_Q^2=4(H_Q^0)^2=\tfrac{4}{3}(H_Q^n)^2=\delta_Q\frac{1}{N}\sum_{j=1}^{N}\sum_{k=1}^{N_d}|V_{kj}|^2 \tag{91a}$$

and

$$H_Q^2=\tfrac{1}{3}\langle\Delta H_Q^2\rangle, \tag{91b}$$

where $\langle\Delta H_Q^2\rangle$ represents the quadrupolar second moment in the laboratory frame. N_d denotes the *total* number of defects (mobile as well as immobile). In the two limiting cases of "strong" and "weak" collisions, eq. (83) can be simplified as follows.

(*a*) *Quadrupolar strong-collision region.* For $\tau_m \gg T_m$ the "lattice" correlation function $G_Q(t)$ in eq. (83) remains in essence unchanged while $k_Q(t)$ decays to zero during quadrupolar thermal mixing. In practice, $k_Q(t)$ therefore vanishes at all times [see eq. (87)] and one obtains

$$\frac{1}{T_{1\rho}}=\frac{\delta_Q}{H_1^2+H_D^2+H_Q^2}\left(-\frac{\mathrm{d}\,G_Q(t)}{\mathrm{d}t}\right)_{t=0}. \tag{92}$$

Introducing by [see eqs. (85) and (91)]:

$$H_Q^2|_{dyn}=\delta_Q\frac{1}{N}\sum_{j=1}^{N_d^*}\sum_{k=1}^{N_d^m}|V_{kj}|^2 \tag{93}$$

a *dynamical* quadrupolar local field associated with that part of the EFG which fluctuates, thus causing spin–lattice relaxation, eq. (92) may be rewritten as:

$$\frac{1}{T_{1\rho}}=\frac{H_Q^2|_{dyn}}{H_1^2+H_D^2+H_Q^2}\frac{1}{G_Q(0)}\left(-\frac{\mathrm{d}\,G_Q(t)}{\mathrm{d}t}\right)_{t=0}. \tag{94}$$

Analogous to the theory of Rowland and Fradin [149], the factor on the right-hand side of eq. (94) involving $G_Q(t)$ may be interpreted in terms of the average rate of change of the mobile part of the quadrupolar energy due to the dislocation motion. In order to show this, the initial time derivative of $G_Q(t)$ may be replaced approximately by

$$-\left.\frac{\mathrm{d}\,G_Q(t)}{\mathrm{d}t}\right|_{t=0}\simeq\frac{G_Q(0)-G_Q(\tau_m)}{\tau_m}. \tag{95}$$

Then, eq. (94) becomes

$$\frac{1}{T_{1\rho}}\simeq\frac{H_Q^2|_{dyn}}{H_1^2+H_D^2+H_Q^2}(1-q)\frac{1}{\tau_m}, \tag{96}$$

where

$$1-q=\frac{G_Q(0)-G_Q(\tau_m)}{G_Q(0)} \tag{97}$$

represents the average relative change of the mean quadrupolar energy per spin due to one defect jump. (See Rowland and Fradin [149].) As a final remark, instead of the dynamical local field $H_Q^2|_{dyn}$ we could equally well have inserted the total quadrupolar local field H_Q^2 eq. (91) into eq. (92). The factor involving $G_Q(t)$ then would have to be interpreted in terms of the rate change of the *total* quadrupolar energy due to defect jumps.

(*b*) *Quadrupolar weak-collision region.* For $\tau_m \ll T_m$, $G_Q(t)$ decays much more rapidly than $k_Q(t)$. Hence, in eq. (83) $k_Q(t)$ may be replaced by unity according to eq. (87). After two subsequent partial integrations eq. (83) then yields

$$\frac{1}{T_{1\rho}}=\tfrac{3}{2}\delta_Q)^2\frac{H_1^2+\alpha_Q[H_D^2+(H_Q^n)^2]}{H_1^2+H_D^2+(H_Q^n)^2}J_Q(2\omega_{eff}), \tag{98}$$

where $J_Q(\omega)$ represents the spectral density associated with $G_Q(t)$:

$$J_Q(\omega)=\int_{-\infty}^{+\infty}G_Q(t)\,\mathrm{e}^{\mathrm{j}\omega t}\,\mathrm{d}t. \tag{99}$$

The quantity α_Q in eq. (98) is of the order of two, depending on the ratio H_Q/H_D [140]. It should be mentioned that for a locking field H_1 large compared to the local fields, eq. (98) turns over to the general expression (79). The main difference between the strong-collision expression (92) and the weak-collision relation (98) lies in the absence of thermal mixing between successive defect jumps in the weak-collison region. Accordingly, by extrapolating eq. (92) towards weak collisions, the same result has to be obtained from eq. (98) for $2\omega_{eff}\tau_m \gg 1$. As shown by Wolf and Kanert [146], the result of such a comparison leads to the relation

$$\left.\frac{1}{T_{1\rho}}\right|_{w.c.}\simeq\frac{3}{4}\frac{H_1^2+H_D^2+H_Q^2}{H_1^2+H_D^2+\frac{3}{4}H_Q^2}\left.\frac{1}{T_{1\rho}}\right|_{s.c.}. \tag{100}$$

Consequently, in zero field ($H_1=0$) the difference between the weak- and the strong-collison rate is smaller, the larger H_Q with respect to H_D. In the high-field limit this difference is accounted for by the factor $\frac{3}{4}$.

(*c*) "*Lattice*" *correlation function associated with dislocation motion.* By applying an external stress $\sigma(t)$ to a crystal, dislocations may be forced to move from one stable position to another. The result is an anelastic or plastic contribution to the deformation $\varepsilon(t)$ of the sample. As illustrated above, in order to determine the related nuclear-relaxation behaviour, the corresponding quadrupolar "lattice" correlation function $G_Q(t)$ has to be calculated for some assumed microscopic model of dislocation motion.

The usual procedure applied to determine correlation functions of the type of eq. (85) begins with the conversion of the time average into an ensemble average. This step is only permitted, however, if the microscopic fluctuations causing the decay of $G_Q(t)$ represent a random *stationary* statistical process. In a crystal, dislocations perform discrete jumps. Assuming that the mean time τ_m between successive jumps of mobile dislocations is independent of time, the time average in eq. (85) may be converted into the following ensemble average [150]:

$$G_Q(t)=\frac{1}{N}\sum_{j=1}^{N}\sum_{k=1}^{N_k^m}V_{kj}(r_{kj}^0)\int_{vol}d\tau P_k(r,t)V_{kj}(r_{kj}^0-r). \tag{101}$$

The meaning of the vectors in eq. (101) is easily understood from fig. 18: r_{kj}^0 denotes the initial vector from an element of dislocation k to some spin j, while r symbolizes the displacement vector of the same dislocation k in the slip direction.

$P_k(r,t)$ represents the probability that during time t dislocation k has been displaced by the vector r relative to its position at $t=0$. By assuming the probabilities $P_k(r,t)$ to be independent of r_{kj}^0 (i.e. $P_k\equiv P$) it was implied that the relative motions of atoms and dislocations are uncorrelated. For atoms close to the path of the dislocation this is not quite true. However, since most of the atoms in the crystal do not perform any dislocation-induced jumps, the above approximation is well justified.

A realistic model of dislocation motion has to take into account that the displacement r results from a number of *discrete* jumps. Separating the time scale from the geometry associated with these jumps, analogous to the self-diffusion case, one may write [150]:

$$P(r,t)=\sum_{s=0}^{\infty}W_s(t,\tau_m)P_s(\delta r_s)\delta(r-\delta r_s). \tag{102}$$

Here $W_s(t,\tau_m)$ denotes the probability that some dislocation k performs s discrete jumps in time t if the mean time of stay is τ_m, $P_s(\delta r_s)$ represents the geometrical probability that as the result of s discrete jumps a dislocation has been displaced by the resulting shift vector δr_s. In particular, $P_0(0)=\delta(0)$, and P_s is given by the s-fold convolution integral of P_1.

Inserting eq. (102) into (101) and carrying out the summation over individual dislocations k via an integration over the dislocation loop length one obtains

$$G_Q(t)=\frac{1}{N}\sum_{j=1}^{N}V_j(r_j^0)\sum_{s=0}^{\infty}W_s(t,\tau_m)P_s(\delta r_s)V_j(r_j^0-\delta r_s), \tag{103}$$

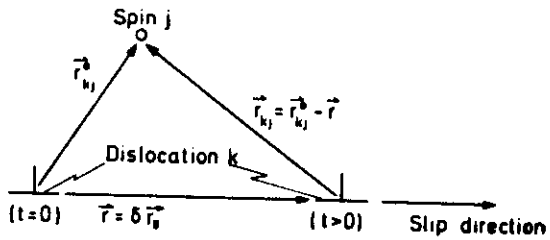

Fig. 18. Geometry of the variables used in the calculation of the quadrupolar geometry factor g_Q for a mobile dislocation.

where $V_j(r_j^0)$ denotes the field gradient at the site r_j^0 of spin j which originates from a unit element of a "representative" dislocation. The transition from $V_{kj}(r_{kj}^0)$ in eq. (101) to $V_j(r_j^0)$ implies that, per unit length, all dislocations are of the same type (e.g. edge or screw dislocations). With this assumption the EFG per unit dislocation length experienced by some spin j no longer depends on the dislocation k producing it, and the vector r_{kj}^0 may formally be replaced by r_j^0.

Also the summation over all N spins may then be simplified. As illustrated by Hut [145], this summation may be restricted to those spins which actually experience a fluctuation of their EFG due to moving dislocations. If n_{ρ_m} is the number of such nuclei per unit dislocation length, $N=\rho_m V n_{\rho_m}$, where ρ_m and V denote the density of *mobile* dislocations and the crystal volume, respectively.

If, as is assumed for solids, a dislocation runs on its way from one obstacle to another with an appreciable fraction f of the sound velocity c_s, the actual time t_j a dislocation spends in the jumping process is much shorter than its mean waiting time τ_m at an equilibrium position. Also, consecutive jumps are uncorrelated with each other in a statistical sense. Therefore the probability $W_s(t,\tau_m)$ is governed by the Markovian relation

$$W_s(t,\tau_m)=\frac{1}{s!}\left(\frac{t}{\tau_m}\right)^s\exp(-t/\tau_m). \tag{104}$$

If during a single jump $s=1$ a dislocation covers the distance $L=|\delta r_1|$, the validity of eq. (104) is limited by the following condition:

$$t_j=L/(fc_s)\ll\tau_m. \tag{105}$$

In typical plastic-deformation experiments $10^{-5}\,\text{cm}\lesssim L\lesssim 10^{-4}\,\text{cm}$ (see sect. 5). Consequently the validity of a Markovian process is unquestioned. The results of this section may be summarized by combining eq. (103) and eq. (104) to yield:

$$G_Q(t)=\frac{\rho_m V}{N}\sum_{s=0}^{\infty}\frac{1}{s!}\left(\frac{t}{\tau_m}\right)^s\exp\left(-\frac{t}{\tau_m}\right)B(s), \tag{106}$$

where the lattice sum $B(s)$ has been defined as follows:

$$B(s)=\sum_{j=1}^{n_{\rho_m}}V_j(r_j^0)P_s(\delta r_s)V_j(r_j^0-\delta r_s). \tag{107}$$

The Fourier transform and first time derivation of $G_Q(t)$ which dominate $T_{1\rho}$ in the weak- and strong-collision region, respectively, are easily found. Differentiating, one has at $t=0$

$$\left(-\frac{dG_Q(t)}{dt}\right)_{t=0}=\frac{\rho_m V}{N}B(0)\left(1-\frac{B(1)}{B(0)}\right)\frac{1}{\tau_m}. \tag{108}$$

Inserting eq. (108) into eq. (92), the quadrupolar relaxation in the strong-collision region becomes

$$\frac{1}{T_{1\rho}}=\frac{\delta_Q}{H_I^2+H_D^2+H_Q^2}\langle V^2\rangle g_Q\frac{\rho_m}{\tau_m}. \tag{109}$$

Here the summation j over spins in eq. (107) has been converted into an integration

over r and θ, thus taking into account that for a given position of the dislocation line with respect to the external field H_0 [see eq. (26)], $V(r)$ depends only on r and θ:

$$\langle V^2\rangle = \int_0^{R_0}\int_0^{2\pi} r\,\mathrm{d}r\,\mathrm{d}\theta V^2(r,\theta). \tag{110}$$

The cut-off radius R_0 corresponds to the number of spins $n_{\rho m}$ appearing in eq. (107). The integral appearing here represents the mean-squared EFG due to a dislocation element of *unit length*. Values of $\langle V^2\rangle$ may be either determined theoretically by means of the corresponding equations given in sect. 3 or derived experimentally from the analysis of the free induction decay $F(t)$ or spin echo $E(t)$ of the NMR signal (see sect. 5). The factor g_Q in eq. (109) is called the "*quadrupolar geometry factor*" and is given by the relation [see eq. (108)]:

$$g_Q = 1 - \frac{B(1)}{B(0)}. \tag{111}$$

Values of g_Q will be discussed in detail in sect. 4.4.

As illustrated by Wolf [151], the spectral density $J_Q(\omega)$ eq. (99) may be written with the aid of eq. (106) as follows

$$J_Q(\omega) = \frac{1}{\omega}\frac{\rho_m V}{N}\sum_{s=0}^{\infty} j_s(\omega\tau_m)B(s), \tag{112}$$

where

$$j_s(x) = \mathrm{Re}[2x/(1-\mathrm{i}x)^{s+1}] = \frac{2x}{(1+x^2)^{s+1}}\sum_{n=0}^{K}(-1)^n\binom{s+1}{2n}x^{2n}, \tag{113}$$

with K being the greatest integer $\leqslant \frac{1}{2}(s+1)$. For $s=0$, $J_Q(\omega)$ represents the usual Lorentzian [obtained by assuming $G_Q(t)$ to be simple exponential as expressed in eq. (80)], since

$$j_0(x) = 2x/(1+x^2). \tag{114}$$

For $s>0$ the functions $j_s(x)$ have been analyzed elsewhere [151]. Furthermore, for $x \ll 1$

$$j_s(x) = 2x \tag{115}$$

for all values of s.

Assuming that the jumps of a dislocation cover distances $|\delta r_s|$ which are fairly large, $V_j(r_j - \delta r_s)$ vanishes to a good approximation except for $s=0(\delta r_s = 0)$ since (in the continuum approximation) the EFG V_j is proportional to $1/r$. Consequently, only terms $s=0$ contribute appreciably to the spectral density $J_Q(\omega)$ given by eq. (112). Then, inserting eqs. (114), (112), and (107) into (98), the relaxation rate in the weak-collision region may be written as follows:

$$\frac{1}{T_{1\rho}} = 3\delta_Q\gamma^2\langle V^2\rangle\frac{H_1^2+\alpha_Q[H_D^2+(H_Q^n)^2]}{H_1^2+H_D^2+(H_Q^n)^2}\rho_m\frac{\tau_m}{1+4\omega_{eff}^2\tau_m^2}. \tag{116}$$

In the limit of large locking fields H_1 eq. (116) becomes

$$\frac{1}{T_{1\rho}} = 3\delta_Q\gamma^2\langle V^2\rangle\rho_m\frac{\tau_m}{1+4\omega_1^2\tau_m^2}. \tag{117}$$

Figure 19 illustrates schematically the relaxation behaviour as a function of the mean waiting time τ_m in the strong- and weak-collision regions. The dashed lines in the figure show the regions which do not comply with the condition for the strong-collision ($\tau_m \gg T_m$) and the weak-collision range ($\tau_m \ll T_m$) respectively. The properties of the maximum of $T_{1\rho}^{-1}$ of eq. (116) provide the most direct access to the understanding of the microscopic dynamic properties of the underlying mechanism of dislocation motion. The position of the maximum governed by the relationship

$$\tau_m^{-1} = 2\omega_{eff} \tag{118}$$

leads to the mean waiting time between two consecutive jumps of a dislocation, whereas the maximum value of $T_{1\rho}^{-1}$

$$\left.\frac{1}{T_{1\rho}}\right|_{max} = \frac{3}{4}\delta_Q\gamma^2\langle V^2\rangle\frac{H_1^2+\alpha_Q[H_D^2+(H_Q^n)^2]}{H_1^2+H_D^2+(H_Q^n)^2}\frac{1}{\omega_{eff}}\rho_m \tag{119}$$

directly yields the density ρ_m of the mobile dislocations. According to eq. (109) a relaxation measurement in the strong-collision region leads only to the ratio ρ_m/τ_m which is indicated by the straight lines in fig. 19. Therefore, to get more detailed information about the mechanism of dislocation motion one has to combine such a NMR measurement with another type of experiment. Such a combined measurement will be discussed below.

It has to be recalled at this point that the model of the microscopic mechanism of dislocation motion has not been specified so far, except for the assumption of discrete dislocation jumps with a fairly large step width. [The latter is used only in the relation for the relaxation rate in the weak-collision region (eq. (116)).] To get a step further, possible mechanisms encountered in different kinds of deformation experiments have

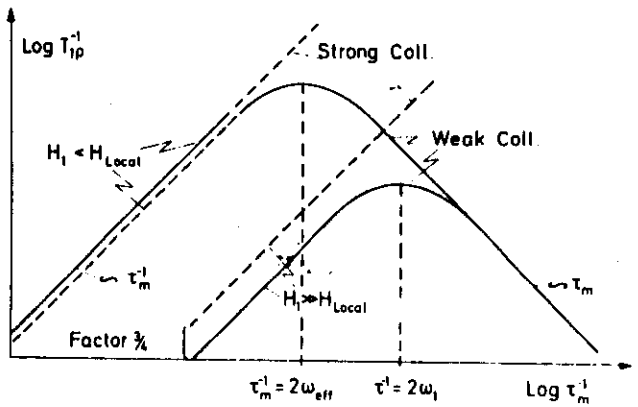

Fig. 19. Schematic double logarithmic plot of the rotating-frame nuclear relaxation rate $T_{1\rho}^{-1}$ versus the inverse of the waiting time τ.

to be introduced into the relaxation theory. In the following we will focus on plastic-deformation experiments with a constant deformation rate $\dot{\varepsilon}$. This type of experiment is governed by the Orowan relation [152]

$$\dot{\varepsilon} = \phi b \rho_m \bar{v} = \phi b \rho_m L/\tau_m. \tag{120}$$

The physical model underlying eq. (120) assumes a thermally activated, jerky motion of the mobile dislocations of density ρ_m between the obstacles in the material. ϕ denotes a geometrical factor ($\phi \approx \frac{1}{2}$), while b symbolizes the magnitude of the Burgers vector. The mean dislocation velocity v may be expressed in terms of the mean distance L between obstacles and the mean waiting time τ_m.

As pointed out above, the strong-collision rate eq. (109) depends similarly to the Orowan equation on the ratio ρ_m/τ_m. Therefore, combining eqs. (109) and (120), one obtains

$$\frac{1}{T_{1\rho}} = \frac{\delta_Q \langle V^2 \rangle}{H_1^2 + H_D^2 + H_Q^2} \frac{1}{\phi b} g_Q \frac{1}{L} \dot{\varepsilon}. \tag{121}$$

Hence, for a given plastic-deformation rate $\dot{\varepsilon}$ the nuclear spin relaxation rate is proportional to the inverse mean jump distance L. This relationship may be used to determine L.

Applying the Orowan equation to the weak-collision relaxation rate eq. (116) for $\omega_{eff}\tau_m \gg 1$, one obtains (approximately)

$$\frac{1}{T_{1\rho}} = \frac{3}{4} \frac{\delta_Q \langle V^2 \rangle}{H_1^2 + H_D^2 + (H_Q^n)^2} \frac{1}{\phi b} \frac{1}{L} \dot{\varepsilon}. \tag{122}$$

As shown in fig. 19, in the limit of large locking fields H_1 eq. (122) differs from the strong-collision rate by a factor $\frac{3}{4}$. In the other extreme, for $\omega_{eff}\tau_m \ll 1$, eq. (116) becomes

$$\frac{1}{T_{1\rho}} = 3\delta_Q \gamma^2 \langle V^2 \rangle \frac{H_1^2 + \alpha_Q [H_D^2 + (H_Q^n)^2]}{H_1^2 + H_D^2 + (H_Q^n)^2} \phi b L \rho_m^2 \frac{1}{\dot{\varepsilon}}. \tag{123}$$

As a final remark of this section one should mention that, in principle, a dipolar fluctuation should occur, also leading to a dipolar relaxation process. For the following two reasons the dipolar lattice correlation function $G_D(t)$ and hence the dipolar contribution to the spin–lattice relaxation rate may be neglected as compared with $G_Q(t)$ if the nuclear spin relaxation is entirely due to dislocation motion:

(i) the mean time τ between successive dislocation-induced jumps of an arbitrary atom is much larger than τ_m. The reason for this is obvious; although a given dislocation may jump rather often during a given time interval, in a single dislocation jump only a fairly small number of atoms move slightly. By definition, however, τ is an averaged quantity for all atoms. Since the great majority of the atoms do not move at all during the deformation experiment, the value of τ averaged over all atoms of the sample is extremely long, and $G_D(t)$ decays considerably less fast than $G_Q(t)$.

(ii) Due to the fact that few atoms ever "see" a dislocation pass by at a distance of less than a lattice constant, and then only in the very short time interval during which they are "visited" by a dislocation, the dipolar lattice sums $B_D(s)$ defined in analogy to

eq. (107) may practically be replaced by their rigid-lattice values $B_D(0)$.

Consequently, the dipolar geometry factor g_D defined analogously to eq. (111) by the relation

$$g_D = 1 - \frac{B_D(1)}{B_D(0)}$$

vanishes, leading to a vanishing dipolar relaxation rate in analogy to eq. (109).

4.4. The quadrupolar geometry factor of dislocations

The remaining problem for calculating the dislocation-induced relaxation rate is to specify the quadrupolar geometry factor g_Q defined by eq. (111). In order to carry out a calculation of g_Q one has to introduce into eq. (107) an "Ansatz" for the geometrical probability $P_1(\delta r_1)$ that as a result of one single jump the dislocation has been displaced by the shift vector δr_1. Assuming a Gaussian distribution centred at the mean jump distance L, the distribution function $P_1(\delta r_1)$ may be written [153] as

$$P_1(\delta r_1) = \frac{1}{(2\pi)^{1/2} \langle \delta r_1^2 \rangle^{1/2}} \exp[-(\delta r_1 - L)^2/2\langle \delta r_1^2 \rangle] \tag{124}$$

where $\langle \delta r_1^2 \rangle$ denotes the second moment of $P_1(\delta r_1)$, i.e. $\langle \delta r_1^2 \rangle^{1/2}$ describes the width of the distribution function $P_1(\delta r_1)$. It should be noted that alternatively a Poisson-like distribution function may be introduced for $P_1(\delta r_1)$ as discussed by Appel et al. [154] in the case of MgO single crystals and by Neuhäuser and Schulz [155] in the case of copper.

Introducing eq. (124) into eq. (107) one obtains for g_Q [eq. (111)]:

$$g_Q(L) = 1 - \frac{1}{(2\pi)^{1/2} \langle \delta r_1^2 \rangle^{1/2}} \cdot \frac{\sum_{j=1}^{n_m} V_j(r_j^0) \int_0^\infty d(\delta r_1) V_j(r_j^0 - \delta r_1) \exp[-(\delta r_1 - L)^2/2\langle \delta r_1^2 \rangle]}{\sum_{j=1}^{n_m} V_j^2(r_j^0)}. \tag{125a}$$

Assuming that the width $\langle \delta r_1^2 \rangle^{1/2}$ of the distribution function $P_1(\delta r_1)$ is small compared to the mean jump distance L, eq. (124) may be approximated by a δ-function, leading to

$$g_Q(L) = 1 - \frac{\sum_{j=1}^{n_m} V_j(r_j^0) V_j(r_j^0 - \delta r_1)}{\sum_{j=1}^{n_m} V_j^2(r_j^0)}, \tag{125b}$$

with $L = |\delta r_1|$.

Starting with eq. (125b), Hut [84, 145] has carried out a computer-calculation of the geometry factor g_Q as a function of L for edge dislocations in NaCl. Outside the core

region of the dislocation ($|r_j^0| > r_c = 3b$) he has used the continuum approximation for the EFG V_j according to eq. (29). Inside the core region ($|r_j^0| \leq r_c = 3b$) the radial dependence of the EFG V_j was approximated by a parabolic distance function $f(r_j)$ as given by eq. (41), assuming no change in the angular function $f_{kk'}(\theta, \phi)$ in eq. (29) on going from $r_j < r_c$ to $r_j > r_c$. For $r_j > r_c$ the positions of the nuclei were taken from linear elasticity theory, whereas inside the core the results of a calculation of Granzer et al. [20] for the position of the nuclei have been used. (It should be noted that the atomic positions they obtained do not depend very sensitively on the special type of potential they used.)

Starting with the assumption given above, the computer-calculation of g_Q was performed using 43 nuclei in the core and a region of $200b \times 200b$ outside the core. With those numbers, the convergence of the calculation of g_Q was excellent.

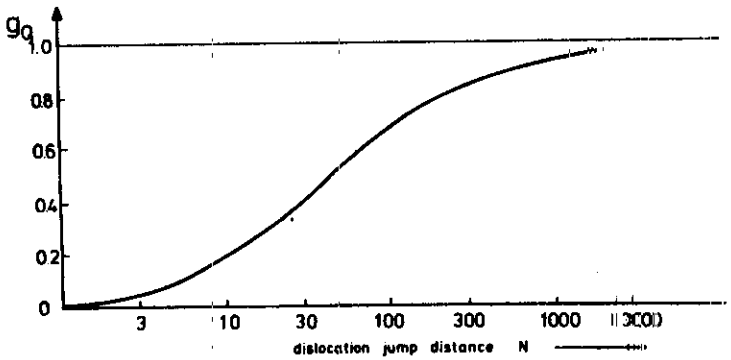

Fig. 20. Quadrupolar geometry factor g_Q for a mobile dislocation as a function of the normalized jump distance N (in units of the Burgers vector).

The result of the computer calculation is presented in fig. 20, where the jump distance L is expressed in units of the Burgers vector b: $N = L/b$. As expected from the general formula (125a) the quadrupolar geometry factor g_Q varies from zero [jump distance $L = |\delta r_1|$ equal to zero, i.e. $V_j(r_j^0 - \delta r_1) \simeq V_j(r_j^0)$] to one [jump distance $L = |\delta r_1|$ equals infinity, i.e. $V_j(r_j^0 - \delta r_1) \simeq 0$ because of $V_j \sim r^{-1}$]. Typically, in plastic-deformation experiments the jump distance L is of the order of 10^{-5}–10^{-4} cm, i.e. $N = L/b$ is of the order of 10^3. As shown in fig. 20, for such a large jump distance g_Q approaches unity and is not very sensitive to a change in L. Furthermore, it has been shown [145] that for large jump distances of the edge dislocation g_Q becomes quite independent of the detailed atomic positions in the core. Therefore for practical applications one may suspect that the difference in g_Q for an edge and for a screw dislocation is not very significant. As a general concluding remark there are good arguments to believe that the shape of g_Q given in fig. 20 describes fairly well the dependence of the quadrupolar geometry factor on the jump distance $N = L/b$ independent of the special type of dislocation and crystal lattice, at least for $N \geq 10^2$.

5. Nuclear spin relaxation measurements and results

5.1. Principles of the measurements

5.1.1. Specimens

The measurements reported on alkali halides were performed on high-purity single crystals. The Jeener experiments [156, 157] were carried out on ^{23}NaCl, ^{87}RbCl and K^{19}F single crystals bought from Quartz and Silice Co. (Paris) and Harshaw Chemical Co. (Solon, Ohio). These crystals were all cylindrical with a length of 15 mm and a diameter of 10 mm, aligned along the ⟨100⟩ crystal axis.

The spin-locking experiments were performed on alkali halide single crystals furnished by Korth Co. (Kiel). The ⟨100⟩ single crystals were cleaved along {100} planes and then carefully polished to square prisms. Before being deformed, all alkali halide single crystals were kept at 150°C for at least six hours and slowly cooled. Spin-locking experiments were also carried out on ⟨111⟩, ⟨110⟩ and ⟨9 13 10⟩ single crystals.

Since it is well known that divalent cation impurities might influence the flow stress of these crystals, some randomly chosen ultra-pure alkali halide single crystals were investigated for their impurity content by means of a Perkin Elmer spectrometer after the deformation. The impurity content was of the order of 0.001 mol% for Ca^{2+} and 0.0001 mol% for Fe^{2+} and for Mg^{2+}. Relaxation experiments were also performed on ⟨100⟩ single crystals doped with different amounts of $CaCl_2$ ranging from 7 to 700 mol ppm.

For the investigations on metals, ultra-pure (99.999%) polycrystalline aluminium samples were used. The average grain size was about 150 μ. To avoid skin-effect distortions of the NMR signal, the samples consisted of thin rectangular foils with a length of 27 mm, a width of 12 mm and a thickness of about 50 μ.

5.1.2. Spectrometer

The spectrometer used was a commercial Bruker SXP 4-100 pulse spectrometer with a modified resonance circuit described elsewhere [158] operating at 15.7 MHz, corresponding to a magnetic field of 1.4 T, including a NMR field stabilizing system. The sample under investigation was plastically deformed by a servo-hydraulic tensile machine (ZONIC Technical Lab. Inc.) in which the exciter head moves a driving rod with a constant velocity. The NMR head of the spectrometer and the frame in which the rod moves formed a unit which was inserted between the pole pieces of the electromagnet of the spectrometer. The unit could be temperature controlled between 77 K and 550 K. The spectrometer was triggered by the electronic control of the tensile machine. The trigger starts the nuclear relaxation measurements of the nuclear spin relaxation experiment at a definite time during deformation.

The decay signal obtained exhibited a signal to noise ratio of about 100:1 in the case of alkali halide single crystals and of about 20:1 in the case of polycrystalline aluminium. The signals were stored on a fast transient recorder (Biomation 802) and then transcribed on magnetic tape. Further processing of the decay data was carried out by an on-line Varian 620/L computer system.

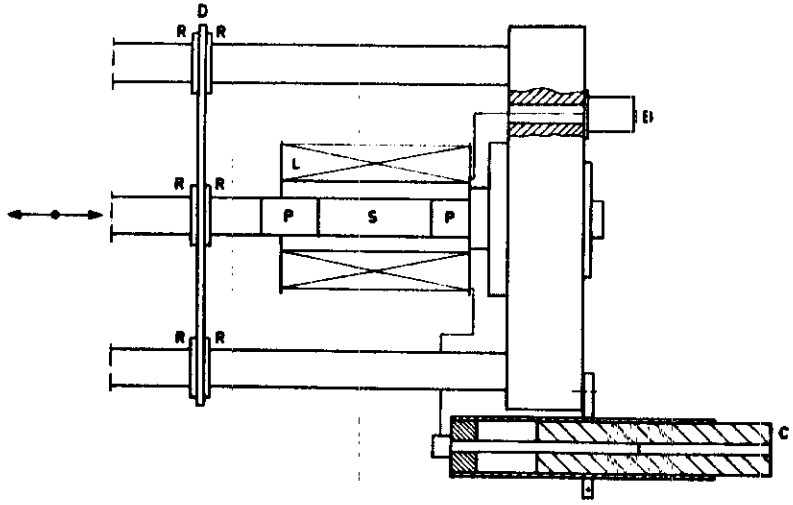

Fig. 21. Part of the mechanical tester which is inserted between the pole pieces and the probe head. D is the diaphragm, L is the coil, B is the connector to the spectrometer, S is the specimen, P are the PVC templates, C is the condenser and R are rings for fixing the diaphragm/rod [145].

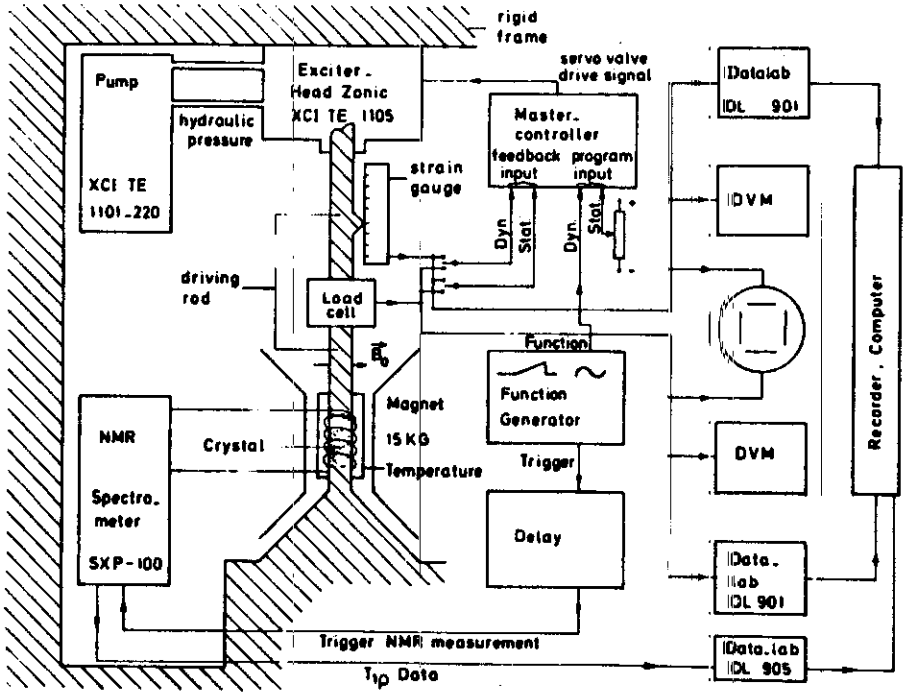

Fig. 22. Scheme of experimental set-up [107, 217].

5.1.3. Mechanical tester

In fig. 21 the part of the assembly between the pole pieces of the magnet is shown schematically [84]. The inner rod (brass) can be displaced relative to the outer ones with a constant velocity. The distance between the rods was fixed by diaphragms with a large stiffness perpendicular to the axis of the rods and a low stiffness in the displacement direction. The diaphragms prevented the bars from buckling; this was effective up to a load of 200 kgf, and the maximum load in the experiments did not exceed this value. The cross-head templates were manufactured from polyvinyl chloride, so as to avoid bringing metal into the coil during a test. The cross-head velocity could be varied from $10^{-5}\,s^{-1}$ to $10\,s^{-1}$. No plastic deformation took place in the machine itself. The direction of compressive deformation always lies perpendicular to the external field H_0.

The stress was measured by a strain-gauge load cell and the elongation by an inductive displacement transducer. Measurements at temperatures lower than room temperature were carried out by using a hollow polyvinyl chloride cylinder around the coil as a cryostat and blowing N_2 vapour through it. Temperature stability of about ± 1°C, which could be sensitively determined by the variation of the pressure, was usually reached in about half an hour.

The part of the tensile machine shown was placed in the gap of a 10 in. Bruker BE-25 magnet with a current stabilizer and an external Bruker NMR stabilizer B-SN 15.

An overview of the experimental set-up is depicted schematically in fig. 22. Detailed information can be found in [217].

5.2. Measurements of T_1, $T_{1\rho}$ and T_2 during plastic deformation of ionic crystals

The first investigation concerned the existence of the effect of a finite plastic deformation rate on the zero-field spin relaxation time ($H_1 = 0$). Using the Jeener pulse sequence [156], signals for two states $\dot{\varepsilon} \neq 0$ and $\dot{\varepsilon} = 0$ were compared for the three single crystals with three different resonant nuclei: the results are presented in fig. 23.

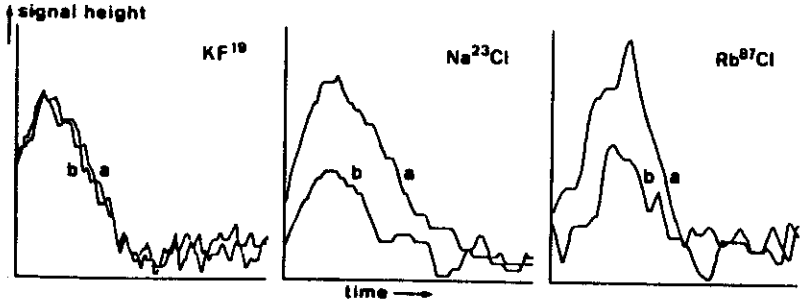

Fig. 23. Signal after a $(\frac{1}{2}\pi - T_2 - \frac{1}{4}\pi/\frac{1}{2}\pi - \tau - \frac{1}{4}\pi)$ pulse sequence as a function of time; the signal height is proportional to $\exp(-\tau/T_{1\rho})$ [159]. $K^{19}F$–a, $\dot{\varepsilon} = 0$; b, $\dot{\varepsilon} = 3.3 \times 10^{-4}\,s^{-1}$; a, $T_{1\rho} = 30$ s; b, $T_{1\rho} = 30$ s; $T = +20$°C, $\tau = 4$ s, $R_D = 0$. $^{23}NaCl$–a, $\dot{\varepsilon} = 0$; b, $\dot{\varepsilon} = 3.3 \times 10^{-4}\,s^{-1}$; a, $T_{1\rho} = 4.7$ s; b, $T_{1\rho} = 2.1$ s; $T = +20$°C, $\tau = 3.5$ s, $R_D = 0.26$ s. $Rb^{87}Cl$–a, $\dot{\varepsilon} = 0$; b, $\dot{\varepsilon} = 1.9 \times 10^{-4}\,s^{-1}$; a, $T_{1\rho} = 1.45$ s; b, $T_{1\rho} = 0.49$ s; $T = -196$°C, $\tau = 3.5$ s, $R_D = 0.26$ s.

The maximum signal height S is related to the time τ the spin system spent in the internal ordering state, i.e. alignment of the spins according to their local fields, by:

$$S(\tau) = S(0)\exp(-\tau/T_{10}). \tag{126}$$

The relaxation time T_{10} is equal to $T_{1\rho}$ with $H_1 = 0$ (see sect. 4).

First T_{10} was determined with $\dot{\varepsilon} = 0$ on the basis of the equation for $S(\tau)$ by varying the time τ between the pulse pair and the read-out pulse and observing the signal height S as a function of this time τ. Then $\tau \approx T_{10}$ was chosen – for maximum change in signal height – and the decays were measured for $\dot{\varepsilon} = 0$ (curves a) and $\dot{\varepsilon} \neq 0$ (curves b).

It is quite obvious from fig. 23 that the zero-field relaxation time of ^{23}Na and ^{87}Rb is affected by plastic deformation whereas T_{10} of ^{19}F is unaltered.

The difference must be attributed to the presence of the quadrupole moment in ^{23}Na and ^{87}Rb which both have $I = \frac{3}{2}$ and to its absence in ^{19}F, which has $I = \frac{1}{2}$. In the case of ^{19}F the effective quadrupolar coupling is equal to zero since for a half-integral spin the levels $m = \pm\frac{1}{2}$ are shifted by the same amount and the transition frequency between them is unaffected in first order by the quadrupolar coupling.

Apparently the dipolar geometry factor g_D (sect. 4), which in principle could be responsible for a change in T_{10} due to dislocation motion, is too small to be observed. The results shown in fig. 23 therefore confirm that the quadrupolar geometry factor g_Q is much greater than the dipolar geometry factor g_D.

There appears to be a contribution from the moving dislocations to the zero-field relaxation via quadrupolar interactions which one would like to separate from other relaxation mechanisms. This may be done by applying the relation:

$$\frac{1}{T_{10}} = \frac{1}{T_{10}(\dot{\varepsilon}=0)} + \frac{1}{T_{10D}}, \tag{127}$$

where the total relaxation time T_{10} is split up into a component due to dislocation motion T_{10D} and one due to all other causes $T_{10(\dot{\varepsilon}=0)}$. In this formula it is assumed that both relaxations, i.e. with and without plastic deformation, are described by an exponential decay.

Figure 24 shows the experimental data confirming the exponential character of the decays following a Jeener pulse sequence.

A problem arises if one does not take into account the change of the line shape as a function of plastic strain due to the increase of the dislocation density. The signal height was always determined from the integral of a number of digitalized values grouped around the maximum signal. By this procedure the effect of noise on the signal is diminished; this is important during deformation where signal averaging is impossible. However, although the maximum signal height is unaffected by an increase in dislocation density, the integrated signal height is lowered by the increase in the number of nuclei influenced by quadrupolar interactions due to dislocations. To avoid this problem the experimental data depicted in fig. 24 by squares were obtained from 4 different crystals, which were deformed with the same velocity, and at approximately the same amount of plastic strain. The data indicated by dots were obtained from one crystal.

For each deformed crystal $S(0)$ was determined as a function of plastic strain ε

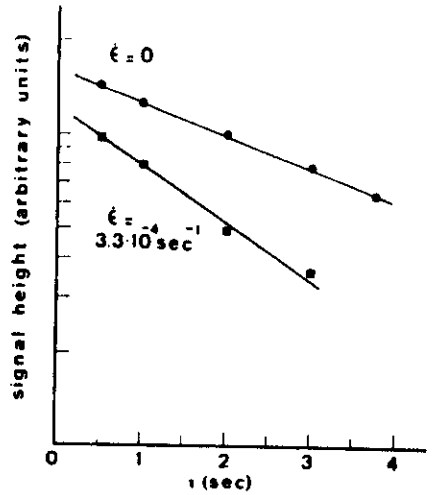

Fig. 24. The exponential character of the decays following a Jeener pulse sequence with and without plastic deformation of the specimen. The signal heights are plotted on a logarithmic scale [145, 157].

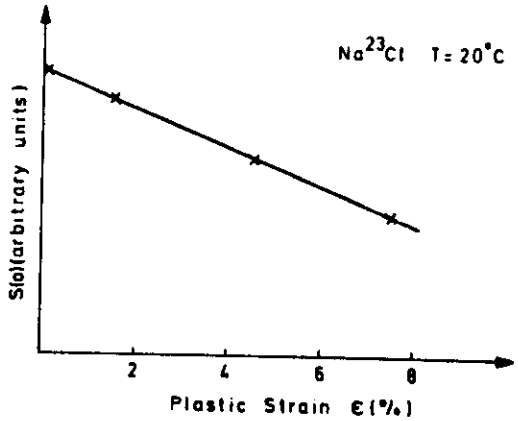

Fig. 25. The variation of $S(0)$ with strain obtained from the Jeener pulse sequence [145].

by interrupting the deformation process at intervals of a few percent of plastic strain and by then varying τ in eq. (126). An example of such an experimentally determined relationship between $S(0)$ and ε is shown in fig. 25. During plastic deformation only one signal can be obtained for given values of τ and ε. Using fig. 25, $S(0)$ was determined from the measured value of ε at the moment the decay was obtained. The exponential relationship between the signal height and τ (fig. 24) was used to determine T_{10} or $T_{1\rho}$ from $S(0)$ and the single measured signal height at the given value of τ.

In fig. 26 T_{10} is given as a function of plastic strain for various deformation rates $\dot{\varepsilon}$. It is quite obvious from this plot that both parts of the relaxation time, the background

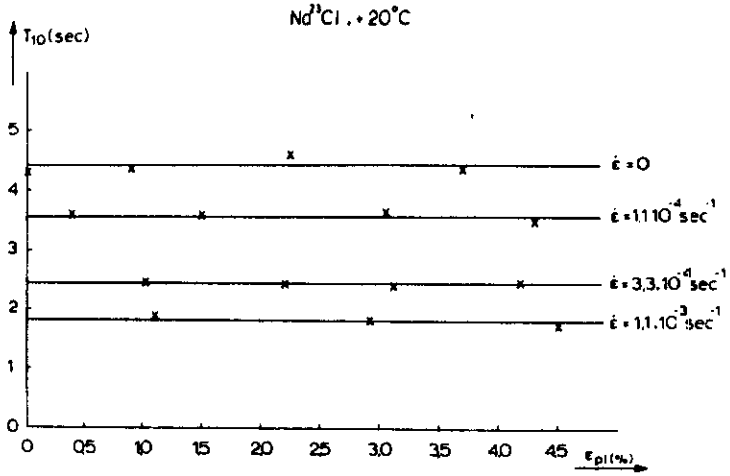

Fig. 26. T_{10} as a function of plastic strain for various deformation velocities $\dot{\epsilon}$ [145, 157].

relaxation time and the contribution due to dislocation motion, are independent of the plastic strain.

An example of a typical $T_{1\rho}$ measurement on ^{23}NaCl is shown in fig. 27. The behaviour of $T_{1\rho}$ as a function of deformation rate was found to be quite analogous to that of T_{10}, as might be expected on theoretical grounds (see sect. 3). However,

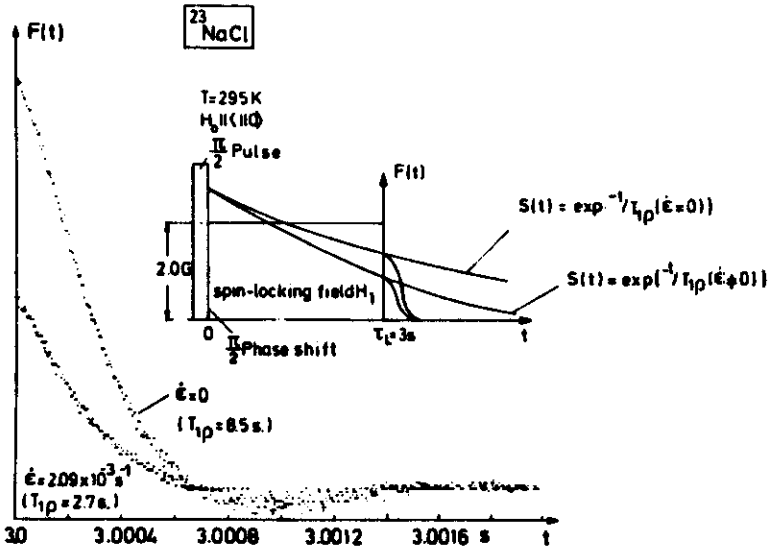

Fig. 27. Experimental result showing two free induction decays $F(t)$ after a spin-locking field H_1 of 2 G (see insert) with zero and with finite plastic deformation rates $\dot{\epsilon}$. The values of $T_{1\rho}$ given in the figure are calculated from the usual expression $F(t) = F(0)\exp(-t/T_{1\rho})$ in which $F(0)$ is the maximum of $F(t)$ [160].

$T_{1\rho}$ experiments have a much better signal to noise ratio than T_{10} measurements. In addition an extra variable H_1 is available in $T_{1\rho}$ experiments (see sect. 4). For these reasons most of the experiments carried out were spin-locking experiments.

Since $T_{1\rho}$ is not a function of strain, the $T_{1\rho}$ experiments were performed as depicted in fig. 28. One crystal is deformed with increasing deformation velocities. $T_{1\rho}$ is unaltered when both the applied load and the plastic strain rate are zero. From the results depicted here it is evident that the change in $T_{1\rho}$ is a function of the plastic strain rate. It is observed that the line shape of the decay is unaffected during plastic deformation. From these results and from the exponential decay the dynamic part of the relaxation rate due to dislocation motion R_D^p can be calculated according to

$$R_D^p = \frac{1}{T_{1\rho}(\dot{\epsilon} \neq 0)} - \frac{1}{T_{1\rho}(\dot{\epsilon} = 0)}. \tag{128}$$

In order to check the conditions for the validity of the strong-collision theory [161, 149] for ^{23}NaCl and ^{87}RbCl, T_1 and T_2 were measured during plastic deformation. The result based on the strong-collision theory is applicable only in the limiting case of strong collisions where the sudden quantum approximation can be used [162] (sect. 4). Furthermore, the strong-collision theory may only be applied if the time τ between jumps is much longer than the inverse of the dipolar line width frequency and the energy of the quadrupolar system is not much larger than that of the dipolar system; i.e. before each jump one common spin temperature is established: $\tau \gg (\omega_D)^{-1}$ and $H_Q^2 \leqslant 3H_D^2$.

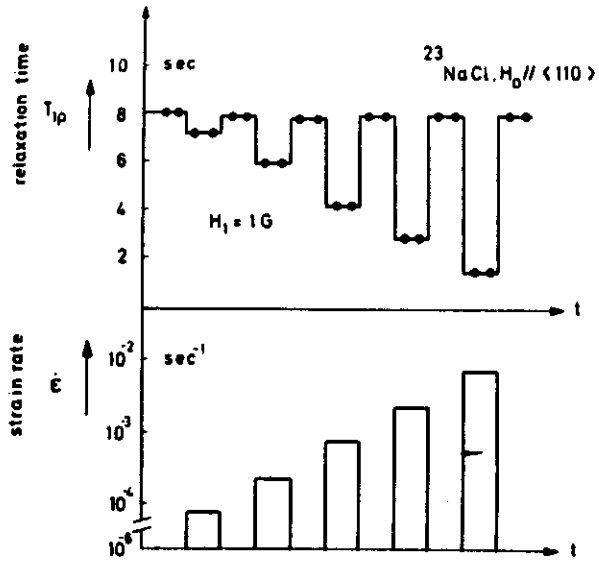

Fig. 28. Experimental run consisting of consecutive compressive deformations at increasing strain rates. The associated decrease in the total relaxation time $T_{1\rho}$ of NaCl is shown in the upper half of the diagram. The variation in the relaxation time $T_{1\rho}$ follows that of the strain rate without any measurable time lag [84].

T_1 was measured after a pulse sequence $\pi-\tau-\frac{1}{2}\pi$; no change in signal height or line shape was observed with respect to the non-deforming case, as is illustrated in fig. 29. From fig. 29 it may be concluded that T_1 is unaffected by the plastic deformation rate $\dot{\varepsilon}$.

In ^{87}RbCl, T_2 was determined as a function of plastic strain rates using a pulse $\frac{1}{2}\pi-\tau-\beta$ [111]. Because the signal height given by $S=S(0)\exp(-\tau^2/2T_2^2)$ was found to be constant (see fig. 30) for the same τ, it was concluded that T_2 is constant and unaffected by the plastic deformation rate $\dot{\varepsilon}$.

From the constancy of T_1 and the change in the spin–lattice relaxation time in the

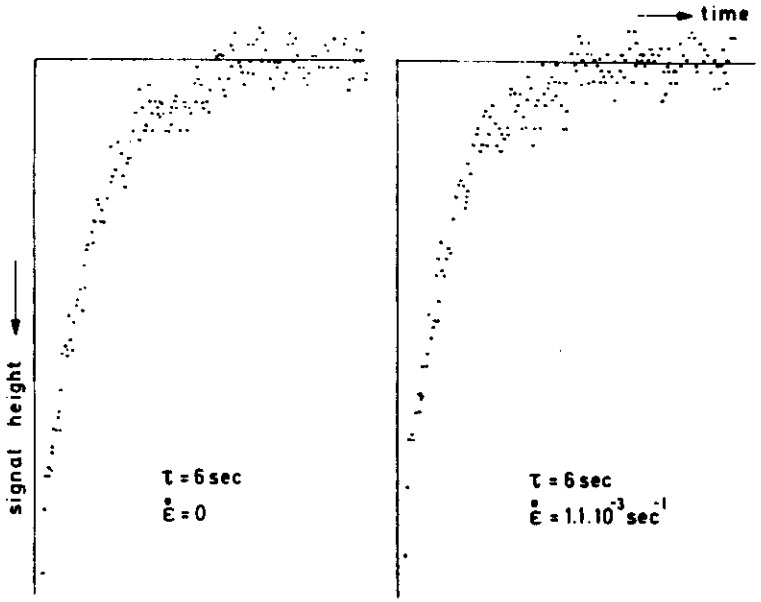

Fig. 29. Two decay curves of ^{23}NaCl at 20°C after a pulse sequence $\pi-\tau-\frac{1}{2}\pi$. The signal height is given by $S=S(0)[1-2\exp(-\tau/T_1)]$ [145].

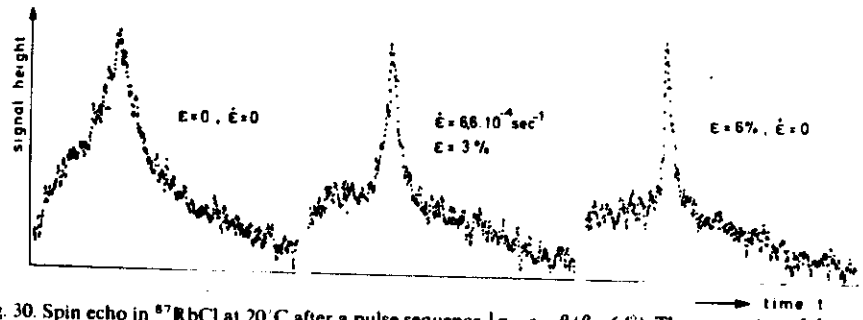

Fig. 30. Spin echo in ^{87}RbCl at 20°C after a pulse sequence $\frac{1}{2}\pi-\tau-\beta$ ($\beta=64°$). The narrowing of the peak is due to the increase of the dislocation density with plastic deformation [145].

rotating frame $T_{1\rho}$ during plastic deformation it may be concluded that a dislocation line actually jumps in a time considerably less than $(\omega_D)^{-1}$.

Whether or not the concept of a common spin temperature before each jump is valid depends also on the values of H_D^2 and H_Q^2. This will be discussed in the next section.

Before concluding this section, however, it should be noted that a more general theory than that of strong collision was presented in sect. 4 following Wolf [163], in which there are no limitations in the mean time of stay τ of dislocations. Especially when crystals are deformed at constant deformation rates $\dot{\varepsilon}$ in a very large rate interval, say from 10^{-4} to 10^2 s^{-1}, the strong-collision model fails. Experimental evidence will be presented for Wolf's NMR relaxation theory in sect. 5.2.5.

5.2.1. Test of the validity of the theoretical model

The dislocation-motion induced part of the relaxation rate $1/T_{1\rho D}$ is given by eq. (121) of sect. 4 [146]:

$$\frac{1}{T_{1\rho D}}\equiv R_D{}^{\rho}=\frac{\delta_Q\langle V^2\rangle}{H_1^2+H_L^2}\frac{g_Q(L)}{\phi bL}\dot{\varepsilon}, \tag{129}$$

where δ_Q is a quadrupole coupling constant, $\langle V^2\rangle$ denotes the mean-squared electric field gradient due to the stress field of a dislocation of unit length and H_L is the mean local field at a resonant nucleus determined by the local dipolar field H_D and the local quadrupolar field H_Q: $H_L^2=H_Q^2+H_D^2$. The quadrupolar geometry factor g_Q depends on the mean step width L of a dislocation. Equation (129) is valid as stated before in the strong-collison region where a common spin temperature exists between successive dislocation jumps.

In order to obtain experimental proof for eq. (129), R_D^{ρ} was measured as a function of $\dot{\varepsilon}$ with H_1 as a parameter (fig. 31). The slope of the curves up to $\dot{\varepsilon}\approx 2\times10^{-3}$ s^{-1} is about 1 as predicted by eq. (129). According to eq. (129) a plot of the relaxation time $T_{1\rho D}=(R_D^{\rho})^{-1}$ versus H_1^2 will yield a straight line, which can be extrapolated to the intercept at $H_1^2=-H_L^2=-\gamma^{-2}(\langle\omega_D^2\rangle+\langle\omega_Q^2\rangle)^{-1}$. The slope of the line is determined by $C\dot{\varepsilon}^{-1}$:

$$C\dot{\varepsilon}^{-1}=\frac{\phi bL}{\delta_Q\langle V^2\rangle g_Q(L)}\dot{\varepsilon}^{-1}, \tag{130}$$

where C is approximately constant. Figure 32 shows the result of such an evaluation of the experimental data, confirming the theoretical predictions of eq. (129). The occurrence of an apparent common point of intersection of the different experimental curves with the H_1^2 axis is explained by the fact that the change in H_Q^2 with strain in the different samples yielding the data in fig. 32 is small compared to $H_D^2+H_Q^2$ and lies within the experimental error. Furthermore, the ratio of the slopes of two different curves in the figure is equal to the inverse ratio of their deformation rates $\dot{\varepsilon}$ as required by eq. (130).

In these measurements the crystals were oriented with one of the ⟨110⟩ directions parallel to the large external field H_0 so as to avoid a possible orientation effect. Subsequently R_D^{ρ} in ^{23}NaCl was measured as a function of the slip-plane direction

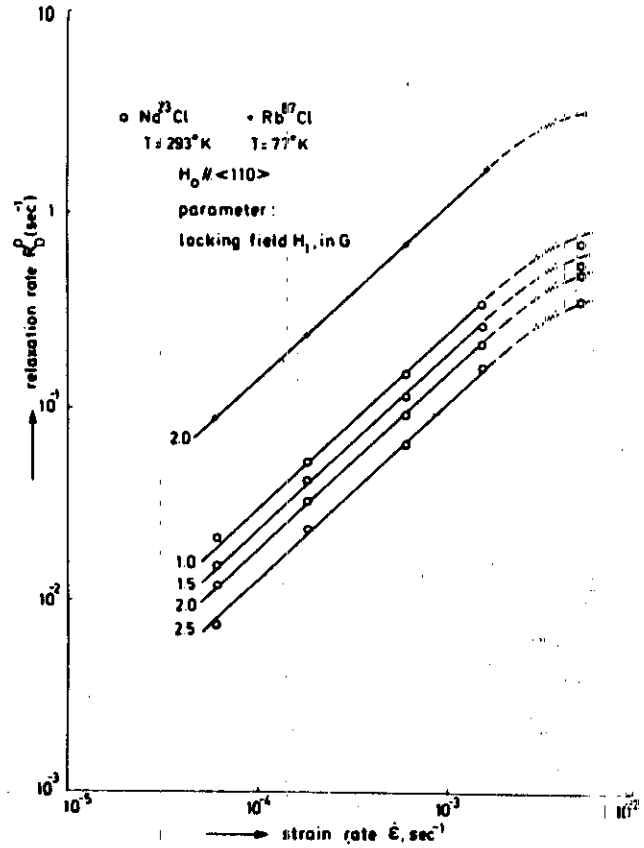

Fig. 31. Experimental data of R_0^{ρ} for ^{23}Na and ^{87}Rb as functions of $\dot{\varepsilon}$ [84].

relative to H_0. No orientation dependence was observed within an error of about 10%; this is in good agreement with the theoretical model used for the calculation of $g_Q(L)$ as described earlier in sect. 4.

So far only the qualitative agreement between theory and experiment has been discussed. In order to determine whether there is a quantitative agreement the values of the different parameters of eq. (129), viz. $\delta_Q\langle V^2\rangle$, $\langle\omega_D^2\rangle$ and $\langle\omega_Q^2\rangle$ should be known.

For the shape of the free induction decay after the locking pulse (see fig. 27) the following expression holds ([103], p. 10):

$$F_n(t)=c_{-1/2}D(t)+c_s D(t)Q^+(t), \tag{131}$$

where $F_n(t)$ is the normalized decay function, $c_{-1/2}$ and c_s are the transition probability coefficients and $D(t)$ and $Q^+(t)$ the dipolar and quadrupolar Fourier cosine transforms, respectively, of the distribution functions.

With $I=\frac{3}{2}$ for ^{23}NaCl one obtains ([103], pp. 62ff):

$$c_{-1/2}=0.4, \qquad c_s=0.6, \qquad Q^+(t)=Q(2t). \tag{132}$$

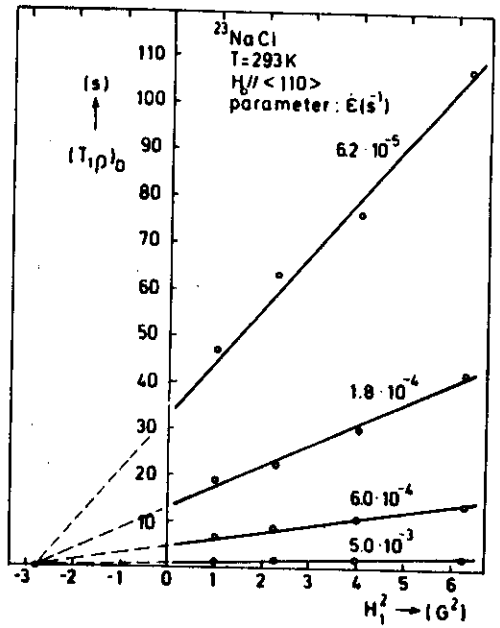

Fig. 32. $T_{1\rho c}$ of ^{23}Na versus H_1^2. The intersections of the lines with the abscissa are approximately at one point, given by $-2.6\,G^2$ [84, 145, 160].

Assuming Gaussian distribution functions [eqs. (55), (56) and (59)],

$$D(t)=\exp(-\tfrac{1}{2}\langle\Delta^2\rangle t^2), \tag{133}$$

and

$$Q(t)=\exp(-\tfrac{1}{2}\langle a^2\rangle t^2), \tag{134}$$

where $\langle\Delta^2\rangle^{1/2}$ and $\langle a^2\rangle^{1/2}$ are the dipolar and quadrupolar line widths ($\frac{1}{2}\langle\omega_D^2\rangle^{1/2}$ and $\frac{1}{2}\langle\omega_Q^2\rangle^{1/2}$, respectively), the resulting expression for $F_n(t)$ becomes:

$$F_n(t)=0.4\exp(-\tfrac{1}{2}\langle\Delta^2\rangle t^2)+0.6\exp(-\tfrac{1}{2}\langle\Delta^2\rangle t^2)\exp(-2\langle a^2\rangle t^2). \tag{135}$$

Fitting F_n to the measured free induction decay, the dipolar energy term $\langle\omega_D^2\rangle$ and the quadrupolar energy term $\langle\omega_Q^2\rangle$ can be obtained at several stages of the deformation process. From these analyses it was found that $\langle\omega_D^2\rangle\simeq 32\times10^6\,s^{-2}$, in good agreement with the value $40\times10^6\,s^{-2}$ as given by Hebel [164], and to first order independent of strain.

The results of the values for $\langle\omega_Q^2\rangle$ thus obtained as functions of the applied stress are shown in fig. 33. Using a statistical distribution of dislocations one may write [eq. (70)]:

$$\langle\omega_Q^2\rangle=A\rho=\gamma^2\delta_Q\langle V^2\rangle\rho, \tag{136}$$

where A is a constant ($\simeq0.13\,cm^2\,s^{-2}$ for ^{23}NaCl) and ρ stands for the total dislocation density. Because of the linear relationship between $\langle\omega_Q^2\rangle^{1/2}$ and the applied

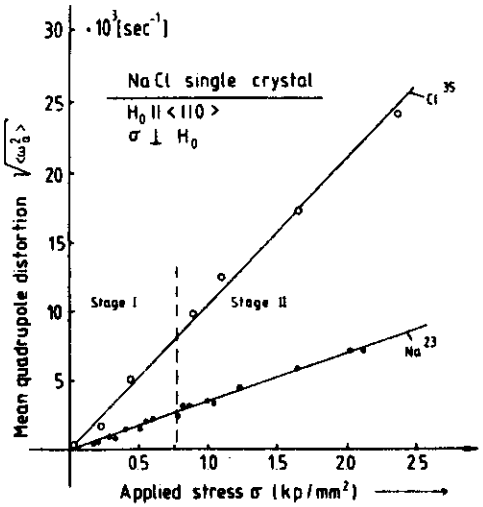

Fig. 33. Linear relationship for NaCl between the applied stress and $\langle\omega_Q\rangle^{1/2}$ measured on ^{23}Na and on ^{35}Cl. The different sensitivity of the two probes is mainly caused by the difference in the nuclear quadrupolar moments Q and in the gradient elastic constants (table 2) [84].

stress σ depicted in fig. 33, it confirms the well-known proportionality between the shear stress and $\rho^{1/2}$ in stage I and stage II which was found by Matucha et al. [52] and Hesse and Hobbs [34]. The maximum value of H_Q^2 in these experiments was 1.3 G^2, which satisfies the condition that H_Q^2 is not much larger than H_D^2($\simeq$0.6 G^2).

Further evaluating eq. (129) quantitatively, a preliminary estimate of the average distance between obstacles encountered by a "jumping" dislocation can be made. Taking the curves for ^{23}NaCl in fig. 31 it is observed that

$$R_D^p = C(H_1)\dot{\varepsilon}. \tag{137}$$

Numerical evaluation of the experimental results yields the value 161 for $C(H_1)$ at $H_1 = 2$ G. Quantitative agreement between eq. (129) and the experimental result [eq. (137)] is obtained, using eq. (136), only if

$$\frac{g_Q}{L} = C(H_1)\frac{\gamma^2 H_1^2 + \langle\omega_D^2\rangle + \langle\omega_Q^2\rangle}{A}\phi b, \tag{138}$$

where $\langle\omega_D^2\rangle + \langle\omega_Q^2\rangle = \gamma^2 H_L^2$. Inserting the values of $C(H_1)$, $\langle\omega_D^2\rangle \simeq 32\times10^6$ s^{-2}, $\langle\omega_Q^2\rangle = 16\times10^6$ s^{-2} (fig. 33), $\gamma^2 = 50\times10^6$ G^{-2} s^{-2}, $A = 0.13$ cm^2 s^{-2}, $\phi = 0.5$ and $b = 0.396$ nm, it follows that:

$$\frac{g_Q}{L} \simeq 6.31\times10^5 \text{ m}^{-1}. \tag{139}$$

From the calculated values of g_Q/Nb (sect. 4) it is concluded that only dislocation jumps across large distances satisfy this equality. Taking g_Q approximately equal to 1, L is equal to about 4000 Burgers vectors ($\simeq 1.6\times10^{-6}$ m). This value found for L

agrees reasonably well with the distance between the dislocations given by $\rho^{-1/2}$, which was found to vary between 5×10^{-6} m and 0.5×10^{-6} m in the deformation test (fig. 33). This agreement would confirm the idea of dislocation motion impeded by forest dislocations.

The values for R_D^p for ^{23}NaCl and for ^{87}RbCl (fig. 31), where the same dislocation mechanism operates, are different, since the factor $\langle\omega_Q^2\rangle/(\gamma^2 H_1^2 + \gamma^2 H_L^2)$ in eq. (129) [using eq. (136)] is different for the two nuclei. For nuclei with spin I the mean quadrupolar energy $\langle\omega_Q^2\rangle$ can be written as

$$\langle\omega_Q^2\rangle \simeq \text{constant}\times q^2, \tag{140}$$

with $q = C_{11}Q$, where Q is the nuclear quadrupole moment and C_{11} is the corresponding matrix element of the gradient elastic tensor connecting the mechanical stress tensor linearly to the EFG (sect. 3). The ratio $R_D^p(1)/R_D^p(2)$ of the relaxation rates (1 stands for ^{87}RbCl and 2 for ^{23}NaCl) of the two systems (1, 2) measured in a rotating field of the same strength $H_1 = 2$ G is given by eq. (129):

$$\frac{R_D^p(1)}{R_D^p(2)} = \frac{q_1^2\gamma^2(2)H_1^2 + \langle\omega_D^2(2)\rangle + \langle\omega_Q^2(2)\rangle}{q_2^2\gamma^2(1)H_1^2 + \langle\omega_D^2(1)\rangle + \langle\omega_Q^2(1)\rangle}. \tag{141}$$

The dipolar second moments and the gyromagnetic ratios γ of the two systems are nearly the same. Taking into account the different constants C_{11} and the different quadrupole moments (^{23}NaCl: $C_{11} = 7.5\times10^3$ dyn$^{-1/2}$, $Q = 0.1b$ [103]; ^{87}RbCl: $C_{11} = 32\times10^3$ dyn$^{-1/2}$, $Q = 0.13b$ [134]), a value of approximately 8 is obtained. The latter is confirmed by experiments, where the ratio 8.5 is obtained from fig. 31. From these results it may be concluded that both for ^{23}NaCl and ^{87}RbCl the conditions for eq. (129) to hold are satisfied.

5.2.2. Effect of the orientation of the compression axis on the mean free path of moving dislocations in NaCl

The present section will treat the results obtained using the pulsed nuclear magnetic resonance technique for studying the deformation mechanism of ultra-pure sodium chloride single crystals at room temperature (impurity concentration < 10 ppm). The purpose of this investigation is twofold. First, to provide information about the orientation dependence of work hardening. Results of applying four different deformation axes are presented: ⟨100⟩, ⟨110⟩, ⟨9 13 10⟩, ⟨111⟩. Second, to investigate the self-consistency of the work-hardening theory and of the NMR theory of moving dislocations, and the compatibility of the latter with mechanical experiments. In particular, the mean free paths L of mobile dislocations derived from pulsed nuclear magnetic resonance experiments are compared with the values predicted by work-hardening theory.

In that connection, it is to be understood that the physical model of dislocation motion applied here assumes a thermally activated motion of mobile dislocations between strong obstacles viz. dislocations and impurities.

Because the components of the stress in the glide direction and in the glide plane depend on the direction of the compression axis, the stress-strain (σ versus ε) curves have to be reduced to curves of resolved shear stress against shear strain (τ versus a)

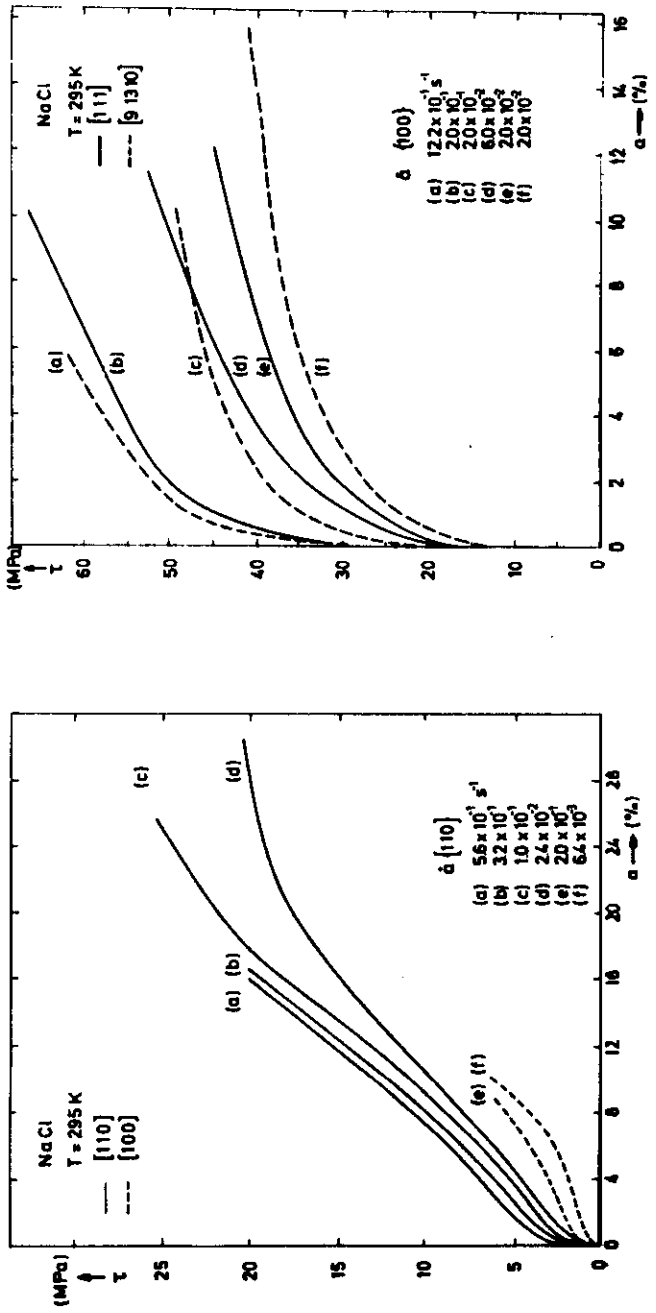

Fig. 34. Shear stress τ as a function of the shear strain a for differently oriented NaCl single crystals for shear on {110} (a) and for shear on {100} (b) [165, 166].

according to $\tau = \phi\sigma$ and $a = \varepsilon/\phi$, in which ϕ is the Schmid factor. The τ versus a curves, resolved on {110} planes for [100] and [110] compression axes and resolved on {100} planes for [111] and [9 13 10] deformation axes, are depicted in fig. 34 using the Schmid factors of the active glide planes which are listed in table 5.

In fig. 35 the accompanying results of the spin-locking experiments have been indicated, where R_D^e has been plotted as a function of the shear strain rate $\dot{a}$ on {110} (fig. 35a) and on {100} (fig. 35b). The linear relation between R_D^e and $\dot{a}$ is expressed in eq. (129). From this proportionality and with the aid of the experimentally known local fields $[\langle\omega_Q^2\rangle + \langle\omega_D^2\rangle]$ and the theoretically determined A_Q (eq. (136)] the mean free path L for dislocations is obtained and listed in table 6.

From fig. 34 it may be concluded that there exists an orientation dependence of work hardening. Work hardening is much higher for the ⟨110⟩ deformation axis than for compression along the ⟨100⟩ axis. In addition, the work hardening along the ⟨111⟩ axis is similar to that along the ⟨9 13 10⟩ compression axis. However, the predominant slip systems in NaCl-type crystals are four $\langle 110\rangle\{1\bar{1}0\}$ slip systems which are equally stressed for the [100] and [110] deformation axes. Nevertheless,

Table 5
The Schmid factor ϕ for ⟨110⟩ slip direction

Deformation axis	{100}	{110}	{111}
⟨100⟩	0.0	0.5	0.41
⟨110⟩	0.35	0.25	0.41
⟨9 13 10⟩	0.5	0.13	0.36
⟨111⟩	0.47	0.0	0.27

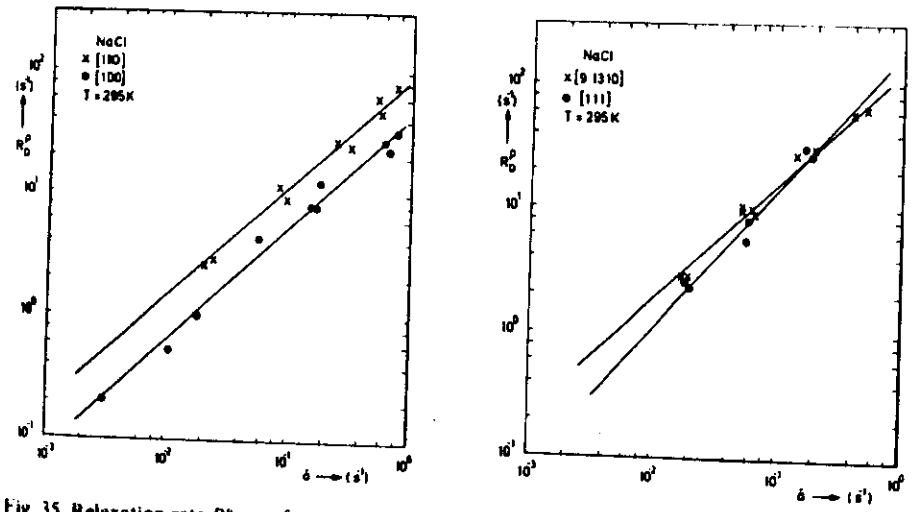

Fig. 35. Relaxation rate R_D^e as a function of the shear strain rate $\dot{a}$ resolved on {110} (a) and on {100} (b) planes [165, 167].

Table 6
The mean free path L (units 10^{-6} m) calculated from the dependence of R_β^β on $\dot{a}$ using the theoretically determined A_Q values (units $cm^2 s^{-2}$)

Deformation axis	{100}	A_Q	{110}	A_Q
⟨100⟩	-		1.53	0.094
⟨110⟩	0.45	0.121	1.22	0.330
⟨9 13 10⟩	0.22	0.045	0.37	0.075
⟨111⟩	0.29	0.055	-	

the [110] compression axis hardens more strongly than the [100] because there exists a finite shear stress on {100} planes when applying ⟨110⟩ compression which is absent using ⟨100⟩ deformation. Extra hardening could be caused by activation of slip on these secondary {100} slip planes and by the interference with primary {110} slip planes. According to Matucha [41] (sect. 2.1), deformation takes place by single slip on one of the {110} planes right from the onset of macroscopic plastic flow (stage I). In stage II where a higher constant work hardening exists than in stage I, about 1% of slip occurs on {100} planes in ⟨110⟩ oriented specimens.

In general, it is to be expected that if L increases, all other variables remaining constant, then the plastic strain a would increase approximately in proportion, and that the strain hardening $\delta\tau/\delta a$ would be inversely proportional to such an increase. Although the experimental scatter is much too large for any quantitative check of this prediction to be made, a comparison between the L values obtained for various axes of compression and tabulated in table 6 and the slopes of the strain-hardening curves in fig. 34 shows that this is broadly true, especially for crystals in stage I, i.e. oriented along [110] or [100]. For crystals in which stage I is absent, viz. those oriented along [111] and [9 13 10], this correlation does not seem to be valid.

Crystals compressed along ⟨111⟩ have no resolved shear stress on {110} planes (table 5). They deform by a combination of {100} and {111} slip [55]. The work hardening rate (fig. 34) is much higher compared to that for deformation along ⟨110⟩, which is in accordance with the observations of Franzbecker [36]. In ⟨9 13 10⟩ oriented crystals slip also occurs on {110}⟨1$\bar{1}$0⟩ systems [39, 40], while not all {100} planes are equally stressed.

From these analyses, the self-consistency of the work-hardening theory, of the NMR theory of moving dislocations, and the compatibility of the latter with mechanical experiments might be concluded.

5.2.3. Influence of the impurity content on the mean free path of moving dislocations in NaCl

The main obstacles at which dislocations can be held up are points where other immobile dislocations (forest dislocations) cut the glide plane, or point defects such as impurities. The intersection of mobile dislocations with forest dislocations can be hard to accomplish because the intersecting dislocations may react and form small nodal dislocation segments, which lower the local energy significantly. Therefore these

obstacles are referred to as "strong" obstacles. In alkali halide crystals of monovalent ions, divalent impurities are effective obstacles. To preserve charge neutrality in the lattice, each impurity ion, e.g. a Ca^{2+} ion in NaCl, is associated with a cation vacancy. These dipoles interact with dislocations and therefore also influence the mechanical properties. At temperatures below 150°C the obstacles are fixed and can be overcome only by thermal activation, whereas at higher temperatures the defects become mobile and are able to follow the moving dislocations, which gives rise to a drag force. Apart from single dipoles, aggregates of dipoles are also present in the crystal. Their number and distribution depend strongly on the thermal treatment previous to the deformation and on the temperature of deformation itself [169].

Considering the fact that the mean free path L in eq. (129) is determined by the mean distance d_F between forest dislocations and by d_p, the mean distance between point defects, eq. (129) is refined by insertion of:

$$\frac{1}{L}=\frac{1}{d_F}+\frac{1}{d_p}. \tag{142}$$

Relaxation measurements have been performed on NaCl (001) single crystals doped with different amounts of $CaCl_2$ ranging from 7 to 340 mol ppm in the temperature range from 10–270°C. The spin–lattice relaxation rate in the rotating frame is measured by means of the spin-locking technique. In fig. 36 the value of $R_\beta^\beta = T_{1\rho}^{-1}(\dot{\varepsilon}\neq 0)$ is depicted as a function of the strain rate $\dot{\varepsilon}$ in the direction of the compression axis for single crystals doped with different amounts of impurities. Raising the concentration of impurities will diminish the mean distance d_p and therefore the relaxation rate will increase. The mean free path L can be determined with the aid of eq. (129), yielding for pure crystals a value for d_F of about 1.0 μm. Evaluation of the data using eq (142) gives values for d_p which are plotted in fig. 37. These results do not correspond with the values obtained from calculations of the mean distance between

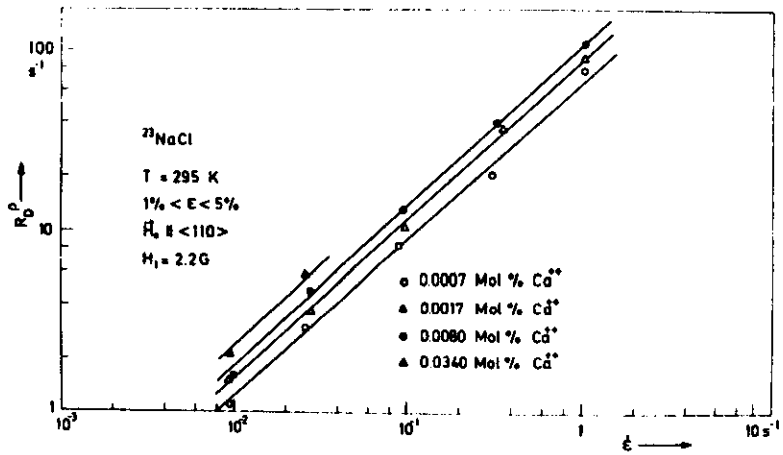

Fig. 36 Dislocation-induced part of the relaxation rate R_β^β as a function of the strain rate $\dot{\varepsilon}$ in ^{23}NaCl single crystals doped with different amounts of impurities [170].

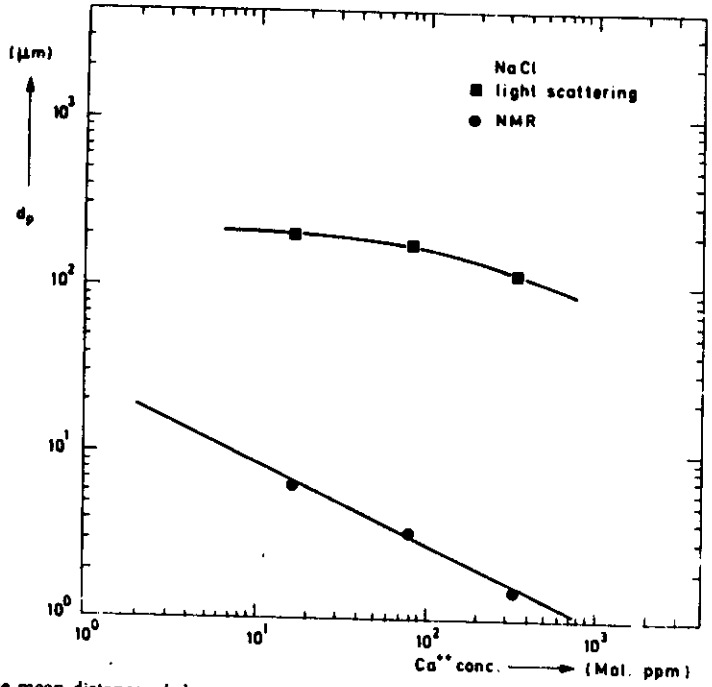

Fig. 37. The mean distances d_p between pointlike obstacles as a function of the Ca^{2+} concentration in NaCl as obtained from NMR measurements and those between large impurity clusters as obtained from light-scattering experiments [172].

randomly distributed single point defects in the crystal with the given impurity concentration C, according to:

$$d_R = (M/C\rho N)^{1/3}, \tag{143}$$

with M the molecular weight, ρ the density and N Avogadro's number. In fact d_p turns out to be about a factor of 100 larger than d_R.

However, a moving dislocation interacts only with defects which lie in its glide plane. The distance between randomly distributed point defects in the plane must be proportional to $C^{-1/2}$ [168, 171]. The NMR data displayed in fig. 37 agree quite well with this. However, d_p is still found to be about 50 times larger than the distance to the nearest-neighbour single-point defect in the plane d'_R. (d_R will be less than d'_R by a factor of about $C^{1/6}$.) It is therefore concluded that impurity clusters are present in the crystals which have been slowly furnace-cooled, and as a result of this the number of local obstacles for moving dislocations diminishes.

The mean distance between the impurity clusters as obtained from light-scattering experiments has also been plotted in fig. 37. These experiments determine the distance between neighbouring clusters in space which must be proportional to $C^{-1/3}$. It is obvious from fig. 37 that the fit to this slope is less good than the slope $-\frac{1}{2}$ obtained from NMR measurements. It should be noted, however, that from the observations

the mean distance between the obstacles in space is found to be larger than that between obstacles in the plane determined by NMR. Because it can be argued that $d'_R > d_R$, it must therefore be concluded that in the light-scattering observations only the largest clusters have been detected. (d'_R should also be greater than d_R if the defects form clusters, provided that the size of the cluster is independent of the concentration C.)

5.2.4. *Measurements of T_1 and $T_{1\rho}$ as functions of temperature*

As long as the mechanism of dislocation motion is unaffected by a temperature change, $R_D (\equiv T_1^{-1})$ should be independent of temperature, as it is a function of this mechanism only. In fig. 38 the results of such measurements performed with the Jeener technique are shown in the temperature range from $-60°C$ to $20°C$. The values of R_D obtained at different temperatures exhibit no effect of temperature variation. This accords well with what is known about the constancy of the mechanism of thermal activation of dislocation motion [173]. In the case of pure $^{23}NaCl$ there obviously exists a constancy of the mechanism of thermal activation of dislocation motion in at least the temperature range from $-60°C$ to $20°C$.

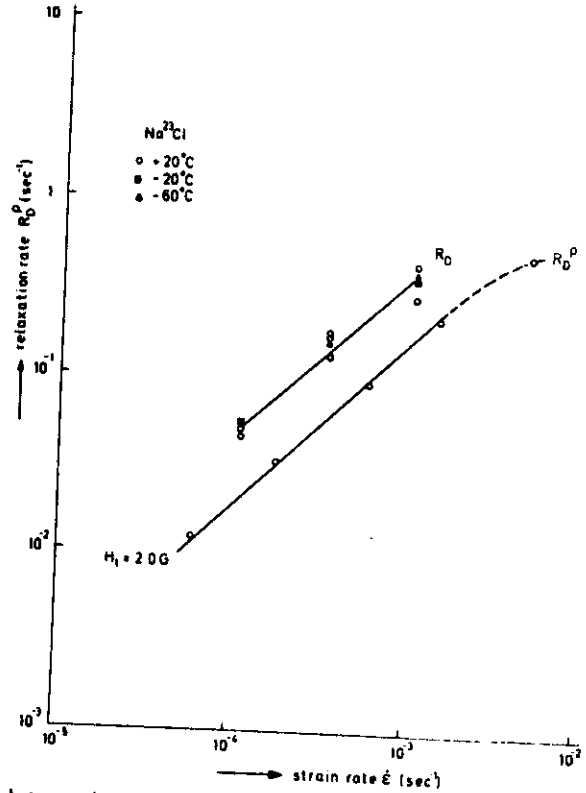

Fig. 38. Comparison between the results obtained by the spin-locking (R_D^ρ) and the Jeener phase-shifted pulse-pair techniques (R_D). The results of the latter were obtained at various temperatures [145].

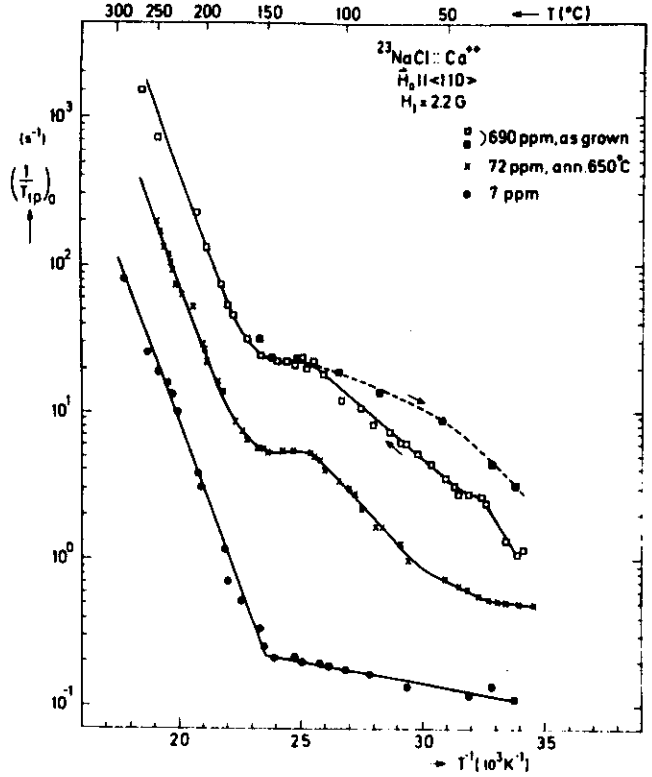

Fig. 39. The static spin–lattice relaxation rate in the rotating frame as a function of temperature in ^{23}NaCl ($\dot{\varepsilon}=0$) [107, 172].

In fig. 39 spin–lattice relaxation rates $T_{1\rho}^{-1}$ are depicted as functions of temperature. These static measurements were performed on ultra-pure single crystals (impurity concentration $\leqslant 10$ ppm) and on crystals containing 72 and 690 mol ppm Ca^{2+} ions. Up to temperatures of about 150°C the lattice part of $1/T_{1\rho}$ in the undoped crystals increases with T, whereas above this temperature an exponential increase occurs with an activation energy of 0.89 eV. The same energy is found from the slope of the high-temperature part of $T_{1\rho}^{-1}$ in doped crystals. In this region the cation–vacancy diffusion is the dominant process and the migration energy corresponds to the above-mentioned value [174]. The effective activation energy of the cation vacancy has been determined by Dreyfus and Nowick [174] based on the ionic conductivity of doped NaCl crystals, and was found to be about 0.8 eV. However, a certain discrepancy in this value exists among various authors, ranging from 0.72 eV [175] to 0.85 eV [176].

In the temperature range between 50°C and 180°C the *static* relaxation rate $T_{1\rho}^{-1}$ depends on the thermal treatment of the doped crystals. The as-grown crystals show an exponential increase with a slope of 0.36 eV, while the crystals after an anneal at 650°C and cooling to room temperature at 50°C/min have higher rates increasing

with a slope of 0.31 eV. These values are close to the dissociation energy of dimers (a configuration of two dipoles). Crawford [177] presented a corpus of ideas regarding the processes underlying the aggregation of divalent cation impurity dipoles. It was shown that the third-order kinetics experimentally observed by Dryden [178] which governs the aggregation can be accounted for on the basis of a two-step process, namely: (a) two dipoles come together to form a loosely coupled pair which in turn (b) captures a third dipole to form a trimer. This process can yield a reaction rate proportional to the third power of the dipole concentration only if the dimers are in quasi-equilibrium with the free dipoles, a condition which implies that the energy binding the pair is rather small ≈ 0.2 eV. Nevertheless, the activation energy for the segregation reaction in NaCl:Ca^{2+} is rather small (0.04 eV) which is probably too small to be significant. Dubiel et al. [179] concluded from T_1 spin–lattice relaxation time measurements in NaCl:Ca^{2+} that aggregation processes take place in the range up to 200°C. For higher temperatures no change in the dipole concentration could be measured. For doping up to 500 ppm mainly dimers and trimers were formed. Analysing their experimental curves they concluded that the enthalpy for the dipole motion was about 0.6 eV and the dimer association enthalpy about equal to 0.3 eV, which is in accordance with the results presented in fig. 39.

Measurements of $T_{1\rho}$ on deforming crystals as a function of temperature yielded the data depicted in fig. 40. They were obtained at a strain rate $\dot{\varepsilon}=0.4\ s^{-1}$ with deformations of $\varepsilon=3\%$ and 7% for the undoped crystals and about 5% for the doped crystals. It can be seen that the room-temperature value of the mean free path for moving dislocations hardly changes in the region up to 150°C. The very few impurities are fixed obstacles with respect to the mobile dislocations and the interactions of the moving dislocations with forest dislocations dominate the magnitude of L. Therefore

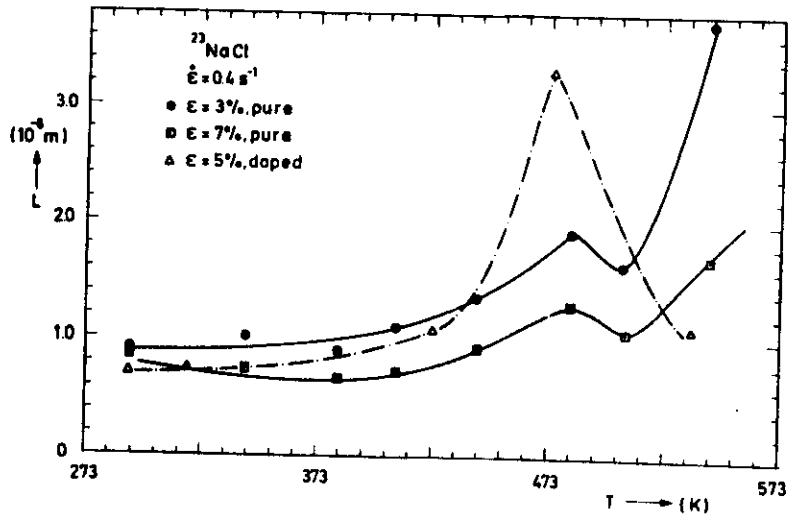

Fig. 40. The mean free path L as a function of temperature for pure and for doped (40 mol ppm Ca^{2+}) NaCl (100) crystals using a strain rate $\dot{\varepsilon}=0.4\ s^{-1}$ [170].

more highly strained crystals show a slightly lower value of L. Above 150°C the migration of vacancies becomes important and the mobile dislocations are assisted in passing the obstacles [152]. This yields an increase in L from the same temperature where the static relaxation rate $T_{1\rho}^{-1}$ starts to increase (see fig. 39). At 260°C L is almost 4 μm for the pure crystal at $\varepsilon = 3\%$. The fraction of weaker obstacles, which can be overcome quite easily at raised temperatures, is smaller for crystals strained to $\varepsilon = 7\%$. This moderates the increase in L at higher temperatures. The extent to which L increases is obviously smaller in the case of highly deformed crystals on account of the change of the ratio strong/weak obstacles.

Some dynamic spin–lattice relaxation measurements on NaCl single crystals with 40 mol ppm Ca^{2+} as a function of temperature are also given. Using eq. (129), the mean free paths L have been obtained from these experiments, and they are depicted in fig. 40. At 260°C L has decreased by about a factor of 4 with respect to the undoped crystals. The variation is caused by the fact that the number of obstacles increases because of the dissolution of dipole aggregates, and the mobility of these point defects increases with temperature; these effects are opposed by an increasing thermal activation of dislocations detained by obstacles.

In the temperature range above 200°C the mobility of Ca^{2+} impurities which are present even in the pure crystals used ($\sim 7 \times 10^{-4}$ mol%) is sufficiently high [181] for them to follow the mobile dislocations, inducing a drag stress by the formation of an impurity cloud around the dislocation. It is a plausible explanation for the decrease of L above 200°C, which is more pronounced in the doped crystals (see fig. 40). Below 150°C the impurities are rather fixed obstacles with respect to the mobile dislocations. The interaction between dislocations and impurities is determined by thermal activation.

The Ca^{2+} impurities are not only effective as fixed obstacles for moving dislocations but can also be effective by forming the so-called Snoek atmosphere of elastic dipoles oriented preferentially in the stress field around the dislocation, causing the Snoek stress [180]. This Snoek stress is necessary to break away the dislocation line from the Snoek atmosphere and superimposes on the short-range stress of thermal activation [182]. Fröhlich et al. [181] concluded from their strain-rate sensitivity measurements on NaCl:Ca^{2+} that the minimum of the strain-rate sensitivity at 150°C deformation temperature is related to the Snoek effect.

5.2.5. *Mobile dislocation density*

Starting from the more general theory of Wolf [163], the relevant quadrupolar part of the rotating-frame relaxation rate induced by the motion of dislocations has been calculated without any limitations on the mean time of stay τ and is depicted in fig. 17 (see sect. 4). To do this, a modified model of thermally activated jerky motion of dislocations as given by Argon [183] was introduced into the relaxation theory (sect. 4).

For the relaxation rate in the strong-collision region, one obtains [see sect. 4.3, eq. (109)], using $H_Q^2 = \delta_Q \langle V^2 \rangle \rho_l$,

$$R_D^\rho = \frac{H_Q^2}{H_l^2 + H_D^2 + H_Q^2} \frac{\rho_m}{\rho_l} \theta_Q \frac{1}{\tau}, \tag{144}$$

where ρ_m and ρ_l are the mobile and total dislocation density respectively. Introducing a mean velocity $\bar{v}$ of the dislocation by $\bar{v} = L/\tau$ and taking the Orowan equation $\dot{\varepsilon} = \phi \rho_m b \bar{v}$ one obtains eq. (129).

A specific formula based on Wolf's theoretical model for the relaxation rate can be written [eq. (117)] for large H_1 as

$$R_D^\rho = \frac{3H_Q^2}{H_l^2 + H_D^2 + H_Q^2} \frac{\rho_m}{\rho_l} \frac{\omega_1^2 \tau}{1 + 4\omega_1^2 \tau^2}. \tag{145}$$

The rotating-frame spin–lattice relaxation measurements were performed at room temperature on ^{23}Na in NaCl and NaF single crystals. The NMR coil of the spectrometer was part of a "fast" tensile machine, described elsewhere [184]. Figure 41 gives the results of R_D^ρ measurements on ^{23}Na in NaCl and in NaF as a function of $\dot{\varepsilon}$ for constant locking fields H_1. The measurements were carried out at a mean constant plastic deformation ε of about 3%. The small value of $\varepsilon = 3\%$ leads to a relatively small local field $H_L = (H_D^2 + H_Q^2)^{1/2} = 1.3$ G since the quadrupolar field H_Q depends on ε, i.e. on the mean elastic strain field due to the presence of dislocations. Figure 41 indicates that eq. (144) is valid not only for low values of the deformation rate $\dot{\varepsilon}$ but also for high values. The measurements point to the strong-collision approximation being applicable over a large range of deformation rates ($\dot{\varepsilon} = 5 \times 10^{-5}$ to 1 s^{-1}), where R_D^ρ is found to be proportional to $\dot{\varepsilon}$.

From the straight lines in fig. 41 the ratio $R_D^\rho(1)/R_D^\rho(2)$ ("1" stands for ^{23}NaCl and "2" for ^{23}NaF) is experimentally found to be equal to 2.0. A theoretical value of the

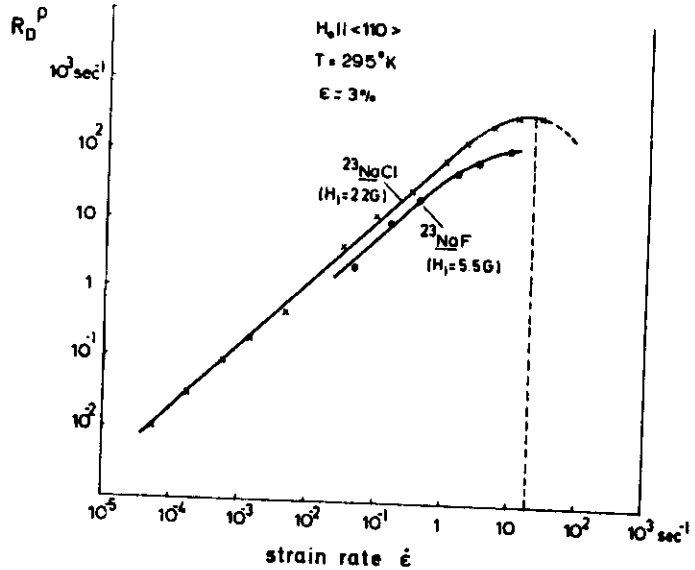

Fig. 41. Measured data of the dislocation-induced part of the relaxation rate R_D^ρ of ^{23}Na in single crystals of (1) NaCl ($H_1 = 2.2$ G) and (2) NaF ($H_1 = 5.5$ G) as functions of the strain rate $\dot{\varepsilon}$ for $\varepsilon = 3\%$. The maximum of R_D^ρ of ^{23}NaCl lies at $\dot{\varepsilon} = 20$ s^{-1} ($H_0 \| \langle 110 \rangle$, $T = 295$ K) [153].

Table 7
Different values for ^{23}NaCl and ^{23}NaF appearing in the relaxation rate eq. (146)

	^{23}NaCl	^{23}NaF
μ	1.85×10^{11} dyn cm^{-2}	3.65×10^{11} dyn cm^{-2}
C_{11}	7.5×10^{3} dyn$^{-1/2}$	6.2×10^{3} dyn$^{-1/2}$
b	0.396 nm	0.327 nm
H_D	0.98 G [136]	3.8 G [123]
H_L	2.2. G	5.5 G

same ratio may be found, using the relation $H_Q \simeq \mu b Q C_{11}$, analogous to eq. (141):

$$\frac{R_D^e(1)}{R_D^e(2)} = X^2 \frac{(H_l^2 + H_D^2)_2 + X^{-2} b_2^2 b_1^{-2} H_Q^2(1)}{(H_l^2 + H_L^2)_1}. \tag{146}$$

where μ is the shear modulus, C_{11} is the corresponding matrix element of the gradient elastic tensor (sect. 3), X represents the ratio $(\mu C_{11})_1/(\mu C_{11})_2$, and Q is the nuclear quadrupole moment. Taking into account the different values for ^{23}NaCl and ^{23}NaF as listed in table 7 a ratio of the relaxation rates of approximately 2.7 is obtained, which is in reasonable agreement with the experimental value ($H_Q = 0.85$ G, $H_L^2 = 1.7$ G^2, see fig. 42) [123, 136].

From the condition for the maximum of the relaxation rate

$$2\omega_{eff}\tau_m = 1, \tag{147}$$

the mean time of stay between two consecutive jumps may be determined. The relative shift of the two maxima is explained by the fact that the effective frequency ω_{eff} is larger for ^{23}NaF than for ^{23}NaCl, as follows from the data given in table 7.

According to eq. (147) the mean waiting time τ_m between two jumps of a dislocation line can be obtained in a direct manner from the maximum value of R_D^e. With $\omega_{eff} = 1.8 \times 10^4$ s^{-1}, derived from the values given above, the following value was found for

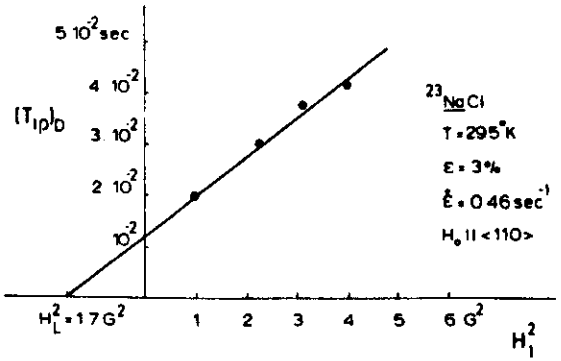

Fig. 42. Relaxation time $T_{1\rho D}$ of ^{23}Na in NaCl versus H_1^2 for $\varepsilon = 3\%$, $\dot{\varepsilon} = 0.46$ s^{-1}. The intersection of the straight line with the abscissa gives a local field $H_L = 1.3$ G [153].

the time τ_m:

$$\tau_m(\dot{\varepsilon}_m = 20\ \mathrm{s}^{-1}) = 2.8 \times 10^{-5}\ \mathrm{s}, \tag{148}$$

and the mean velocity at the maximum $\bar{v}_m = L/\tau_m$ with $L \simeq 2$ μm is

$$\bar{v}_m(\dot{\varepsilon}_m = 20\ \mathrm{s}^{-1}) = 0.071\ \mathrm{m/s}. \tag{149}$$

Using Orowan's relation it is possible to estimate the density ρ_m of the mobile dislocations as:

$$\rho_m = \dot{\varepsilon}/\phi b \bar{v}_m = 1.4 \times 10^{12}\ \mathrm{m}^{-2}, \tag{150}$$

with $\phi = \frac{1}{2}$ and $b \simeq 0.4$ nm.

The value of ρ_m indicates that a relatively high fraction of the dislocations in the crystal is mobile. Hesse and Hobbs [34] found a value of about 3.8×10^{12} m^{-2} for the total dislocation density ρ_t for an applied external stress of 9.5 kp/mm^2 which corresponds approximately to a plastic deformation of $\varepsilon = 3\%$, which is the strain value of interest here. Using the ρ_t value of Hesse and Hobbs results in a ratio of 0.37 for ρ_m/ρ_t. On the other hand, the fraction of the mobile dislocations can be estimated from the maximum value of R_D^e which is attained (see sect. 4):

$$R_D^e(\tau_m) = \frac{3}{4}\gamma H_1 \frac{H_Q^2}{H_l^2 + H_D^2 + H_Q^2} \frac{\rho_m}{\rho_t}. \tag{151}$$

Using the data quoted, the experimental value $R_D^e(\tau_m) = 340\ \mathrm{s}^{-1}$ of fig. 41 leads to $\rho_m/\rho_t = 0.26$, which is in quite reasonable agreement with the value obtained above. It should be remarked here that the good conformity of the two values is more or less fortuitous, since the various data used for the evaluation are applied to different crystals and themselves are subject to appreciable error and uncertainty. Nevertheless, it should be noted that the condition of eq. (147) for the maximum of the relaxation rate is to a first approximation independent of the precise mode of dislocation motion (see for a general discussion ref. [151] and sect. 4).

In this sense, the determination of the mean time of stay τ from eq. (145) could be characterized as direct and relatively independent of the particular model of the dislocation movement employed.

5.3. Measurements of $T_{1\rho}$ during plastic deformation of polycrystalline Al

As has been mentioned before, ultra-pure (99.999%) polycrystalline aluminium samples were used for the investigation on metals. The sample under investigation was plastically deformed by a servo-hydraulic tensile machine of which the exciter head moves a driving rod with a constant velocity. During the deformation ^{27}Al NMR measurements were carried out with a Bruker pulse spectrometer operating at 15.7 MHz. Immediately before and after the plastic deformation the magnitude of the background relaxation time was measured. The motion-induced part of the relaxation time could be determined from the experimental data by means of eq. (128). All measurements were carried out at plastic deformation strains ε between 5% and 30%.

To be sure that the increase in the nuclear spin relaxation rate during the plastic deformation is due to dislocation motion, the relaxation rate was measured while moving the sample with a constant velocity without any deformation. No change in the relaxation rate was observed within the experimental error.

5.3.1. Test of the validity of the theoretical model

According to eq. (129), in the strong-collision region a plot of the dislocation-induced contribution to $T_{1\rho}$ against the square of the locking field H_l will yield a straight line which may be extrapolated to find the intercept with the abscissa at $H_l^2 = -H_L^2$. Figure 43 shows such a plot for $T_{1\rho D}$ at a constant strain rate $\dot{\varepsilon}$ at $T = 77$ K. The total local field thus obtained is $H_L = 4.5$ G. On the other hand, in polycrystalline aluminium Van Vleck's formula [124] leads to a value for the dipolar local field H_D of about 2.9 G. From these data, the quadrupolar local field H_Q caused by the stress field of all dislocations in the sample (mobile as well as immobile dislocations) is obtained as $H_Q = (H_L^2 - H_D^2)^{1/2} \simeq 3.4$ G.

It has to be noted at this point that Van Vleck's formula leads to a value for the dipolar field H_D in the *laboratory* frame. However, since the total local field H_L is measured in the *rotating* frame, first the dipolar field in the rotating frame has to be calculated from an expression analogous to eq. (91b) $\langle H_D^2 \rangle_\rho = \langle \Delta H_D^2 \rangle / 3$ in order to find $\langle H_Q^2 \rangle_\rho$ by making use of the value for H_L^2. A recent analysis by Tamler et al. [188] showed that $H_L \simeq 3.1$ G leading to $\langle H_Q^2 \rangle_\rho \simeq 7.2\,\mathrm{G}^2$ using $H_D \simeq 2.9$ G. Nevertheless, this rotating frame aspect does not greatly affect the value obtained for the mean jump distance L as described in the following section if $H_L \lesssim H_l$.

In fig. 44 the motion-induced part of the relaxation rate, $T_{1\rho D}^{-1}$ measured with a locking field H_l of 10 G is plotted as a function of $\dot{\varepsilon}$ at two different temperatures (77 K and 298 K). For comparison the results of ^{23}Na NMR measurements in NaCl are also inserted in the figure. The slope of the curve up to $\dot{\varepsilon} \simeq 10\,\mathrm{s}^{-1}$ is found to be proportional to the strain rate $\dot{\varepsilon}$ as is predicted by eq. (129). So we may now conclude that the theoretically derived formula for the dislocation-induced part of the relaxation rate is also valid in the case of ^{27}Al.

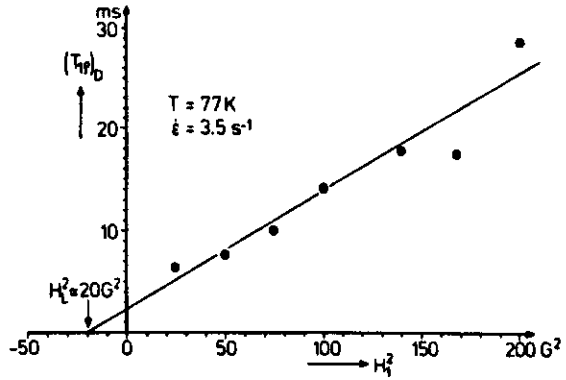

Fig. 43. Plot of the dislocation-induced contribution to the relaxation time $T_{1\rho}$ against the square of the locking field H_l of ^{27}Al at a constant strain rate $\dot{\varepsilon}$ at 77 K [185].

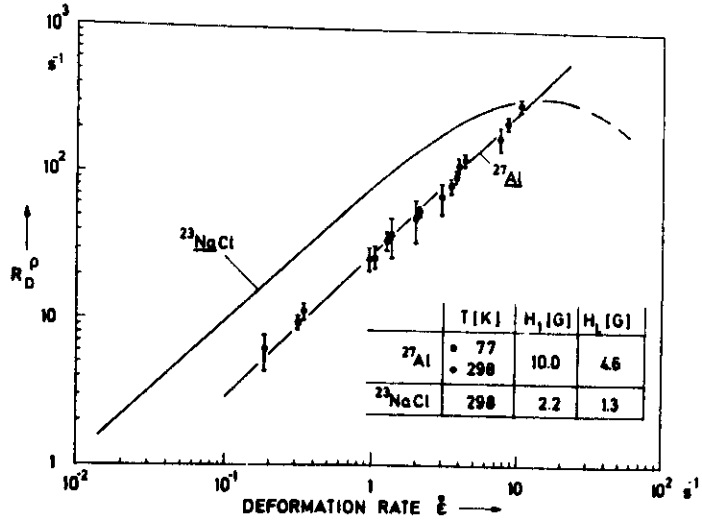

Fig. 44. Dislocation-induced part of the ^{27}Al relaxation rate $T_{1\rho}^{-1}$ in aluminium as a function of $\dot{\varepsilon}$ for two different temperatures. $H_l = 10$ G [185].

5.3.2. Mean jump distance of moving dislocations in Al

As discussed above, from the magnitude of the slope of the curve R_D^ρ versus $\dot{\varepsilon}$, which has a value of about 30, the mean jump distance L can be determined providing the other parameters in eq. (129) are known. The magnitude of the Burgers vector in Al is 0.286 nm and the Schmid factor ϕ for polycrystalline material has been taken to be 0.33 [186]. Using the nuclear data of ^{27}Al the quadrupole coupling constant δ_Q was calculated to be $2.9 \times 10^{-25}\,\mathrm{G}^2\,\mathrm{dyn}^{-1}\,\mathrm{cm}^4$. The mean-square electric field gradient $\langle V^2 \rangle$ is about 1.1×10^{15} dyn cm^{-2}, which can be derived [188] from the work of Preusser [187]. The substitution of these values into eq. (129) with $g_Q \simeq 0.85$ (see sect. 4) yields a mean jump distance L of about 0.1 μm.

The value of L corresponds roughly with the mean distance between dislocations in deformed aluminium, which is of the order of 10^{-4} cm. The rather low value of L found by NMR will be discussed in sect. 6.3. So far, the agreement would confirm the ideas of dislocation motion in ultra-pure f.c.c. metals impeded by forest or network dislocations (see sect. 2.2). In addition, the slope of the curve in fig. 44 should be roughly independent of temperature, since it is known that for many f.c.c. metals the dislocation activation mechanism remains the same between 77 K and 300 K; this is in agreement with the data depicted in fig. 44.

The gliding dislocations have to cut through a forest of intersecting dislocation lines, which involves the creation of jogs at the cutting points. The energy of a jog in aluminium is about 0.5 eV [189], so that thermal fluctuations enable glide dislocations to cut through the forest at ordinary temperatures. At low temperatures [190] (< 200 K) the obstacles become less "transparent".

This is in sharp contrast with jog formation in NaCl-structured materials, where the activation energy for movement of a jog or the formation of defects at the jog is

much higher, about 3 eV [191]. When two dislocations intersect, each acquires an offset segment of the magnitude of $\boldsymbol{b}$ of the other dislocation; whether the offset is a jog or a kink depends on the orientation of the segment with respect to the Burgers vector and the dislocation line. In NaCl the jogs and kinks can be charged or neutral depending on whether they are one interionic distance or two interionic distances long ([13], p. 397). Because of the rather high energy of a jog in NaCl it is very likely that the forest dislocations act as strong obstacles for dislocation motion. In aluminium, because of the high stacking-fault energy (table 1), a dislocation can easily cross slip onto another {111} plane. The constriction in extended screw dislocations which is needed for cross slip is formed quite readily in metals with a high stacking-fault energy such as aluminium. Therefore the mean free path of moving dislocations in Al will be determined by statistically stored dislocations giving rise to Lomer–Cottrell barriers rather than by forest dislocations.

Based on the early studies by Cottrell and Stokes [190] of the effects of temperature on the plastic properties of aluminium crystals, it appears that the important elastic forces on a glide dislocation are those from its immediate neighbours, rather than long-range stresses from piled-up groups. The elastic forces between dislocations and intersections of dislocation lines can both be ascribed to the presence of nearby dislocations. It should be emphasized that at this stage the interpretation has necessarily a speculative component. Nevertheless, dislocations at various velocities in metals have been studied for the first time by means of the pulsed nuclear magnetic resonance technique. In the next section we discuss the interpretation of the mean jump distance L measured by NMR in terms of the statistical slip distance [Λ_{st}, eq. (6)].

6. *Discussion and conclusions*

6.1. Point defects

Plastic deformation results in the generation of vacancies, interstitial atoms and probably more complicated point-defect clusters also. The question arises whether the change in $T_{1\rho D}$ during plastic deformation can be due to the diffusional jumping of point defects. How can we be sure that we see dislocation motion and not vacancy motion, induced by jog dragging? Quantitative predictions regarding the production rate of point defects are still in a distinctly unsatisfactory state. This rate is determined by the dislocation interaction mechanism of the formation of point defects; the moving jog mechanism, or a more static process such as the combination of two edge dislocation segments of opposite sign on neighbouring slip planes, resulting in a row of point defects [192]. Clearly, the motion and generation of dislocations determine in their turn these interactive processes.

Seeger [193] has pointed out that, depending on the temperature of deformation, differences may exist in the mechanism of defect production, according to the relative importance of thermal activation. The details of the mechanism of generation of point defects during plastic flow are not yet completely clear. Undoubtedly a dependence on stress and strain rate exists. However, it seems to be rather difficult to determine the

exact strain dependence. This is due primarily to the difficulty of interpreting observable data such as resistivity, X-ray patterns and density in terms of the concentration of point defects.

For rocksalt-structure crystals deformed in compression on essentially one slip system, the general conclusion is that vacancies (single and double) are produced. The vacancy concentration increases with dislocation density and with strain rate, but there appears to be a threshold strain for appreciable vacancy generation. At sufficiently high temperatures the vacancies are able to form small clusters.

Below, several arguments will be given leading to the conclusion that the effects on $T_{1\rho D}$ in our experiments are due to dislocation motion.

(1) As has been mentioned before, the concentration of point defects increases with increasing strain. Although it may be questionable to calculate the density of vacancy pairs as a function of strain from the changes in density during plastic deformation, Davidge and Pratt [25] calculated for the change with strain of the density of point defects in stage I: 0.7×10^{17} cm^{-3}, and in stage II: 1.3×10^{17} cm^{-3}. If $R\beta$ should be due to the movement of these defects it should be a function of the plastic strain. From fig. 26 it could be concluded that both parts of the relaxation time, the dynamic part due to dislocations and the stationary part, are independent of the plastic strain. Therefore $R\beta$ depends on the dislocation motion and is not affected by the vacancy motion.

(2) The rate of production of point defects appears to be independent of the strain rate as predicted by the models of Saada [194], Van Bueren [195, 196] and Seeger [193], which have been experimentally confirmed. On the contrary, it was found here that $R\beta$ depends on the strain rate $\dot{\varepsilon}$.

(3) At room temperature the vacancies in NaCl are rather immobile. For that reason it is observed that in the temperature range of the experiments, in the range from 77 K to 293 K, $R\beta$ is not a function of temperature. The cation–vacancy diffusion process actually causes the increase of the mean free path L for $T > 410$ K (fig. 40), since climb of dislocations plays a major role in the deformation behaviour of NaCl crystals in the temperature range above 425 K [152]. Due to the process of diffusion-controlled climbing and more simply by thermal activation allowing the bypassing of obstacles, the mobile dislocations are able to overcome weak obstacles at higher temperatures, which leads to an increase of the mean distance L between the effective obstacles (see also sect. 5.2.4). Moreover, the activation energy of a cation jump into a vacancy pair in NaCl is approximately 1.4 eV [197], so that a local motion by vacancy–cation jumps affecting $T_{1\rho}$ is also not very likely.

The situation in Al is quite different. Vacancies are mobile and can be annealed out in Al between about 200 K and 350 K. From studies of the isochronal annealing peaks observed for Al after quenching, it might be concluded that the divacancy is more mobile than the monovacancy and the trivacancy is at least as mobile as the divacancy. The migration energies are equal to 0.65 eV, 0.50 eV and 0.47 eV for the mono-, di- and tri-vacancy respectively [198]. Nevertheless, according to fig. 44, no dependence of $R\beta$ on the deformation temperature has been found in Al (77 K and 300 K). The vacancies possibly produced are certainly immobile at 77 K and mobile at 300 K, and yet no effect was detected on $R\beta$.

(4) From a theoretical point of view, one might say that the long-range stress fields of mobile dislocations induce a larger quadrupolar relaxation rate than the short-range stress fields of mobile vacancies. The quadrupolar frequency ω_Q^2 [related to $\delta_Q\langle V^2\rangle$ in eq. (129)] varies as r^{-3} with the distance r, whereas the mean strain-induced quadrupolar frequency of a nucleus at a distance r from the dislocation line is proportional to r^{-1} [103]. For that reason the production of an excess concentration of vacancies during plastic deformation has little or no effect on ω_Q^2, which is, according to eq. (136), only linearly proportional to the dislocation density.

6.2. Spin-diffusion limitations

From the experimental results of the measurements of T_1 and T_2 it may be concluded that in the strain rate and temperature region considered, the "sudden" approximation and the "strong" collision, i.e. the assumption of a common spin temperature before each new atomic jump, hold for the materials investigated. The dependence of the NMR relaxation rate R_D^6 on the mean waiting time τ of a dislocation before an obstacle, valid in both weak and strong collisions, based on Wolf's general theory [140], was presented in sect. 4 and experimentally confirmed in sect. 5.2.5.

The experimental sensitivity attainable by employing rotating-frame relaxation can be limited by spin-diffusion rates within the bulk of the measured spin systems. Moran and Lang [199] developed a diffusion kernel solution to the spin-diffusion equation and calculated the suppression of the induced decay rate by spin diffusion for the case where this rate is due to self-diffusion of atoms. They found that the relaxation rate R_D^6 due to slow atomic motion when no spin diffusion is involved is suppressed by a factor which depends on the concentration of atoms jumping. Two cases were obtained:

$$R_D^{6\prime} = R_D^6\, e^{-\alpha}, \qquad \text{(locking time } \tau < T_R\text{)}, \tag{152}$$

$$R_D^{6\prime} = R_D^6 \frac{1}{1+\alpha}, \qquad \text{(locking time } \tau > T_R\text{)}, \tag{153}$$

where T_R is the spin-diffusion time constant, determined by the average distance ΔR between the jumping atoms and by the spin-diffusion constant D: $T_R = (\Delta R)^2/16D$. The factor α is the spin-diffusion parameter which is proportional to the atomic correlation time τ. The results of Moran and Lang show that the spin-diffusion suppression of the induced decay rate depends only upon local parameters, is independent of the concentration of the sources, and in all systems reported so far would produce at most a 10% effect. So at most a 10% effect upon R_D^6 might therefore be expected irrespective of the concentration of the sources. When adapting their results to dislocation motion, α must be taken proportional to the plastic strain rate $\dot\varepsilon$, or

$$\alpha = \text{constant} \times \dot\varepsilon. \tag{154}$$

However, since R_D^6 for the materials under investigation exhibits a linear variation with $\dot\varepsilon$, the spin diffusion parameter $\alpha \ll 1$ [199], $e^{-\alpha} \approx 1$ and $(1+\alpha)^{-1} \approx 1$, or

$$(R_D^{6\prime})_{exp} = R_D^6. \tag{155}$$

82

Apparently in the experiments reported spin diffusion plays no significant role, in agreement with the calculations of Moran and Lang. In the experimental data with a maximum in R_D^6 (reached at $\dot\varepsilon = 20\ s^{-1}$ for ^{23}NaCl, sect. 5.2.5), spin diffusion manifests itself by a decreasing slope of the R_D^6 versus $\dot\varepsilon$ curve with increasing values of $\dot\varepsilon$. Equation (155) can be checked experimentally [107] and the reduction of R_D^6 predicted by eq. (152) can also be determined.

6.3. Dislocation motion and dislocation density

The total dislocation density ρ_t was obtained using eq. (136), the relation between $\langle\omega_Q^2\rangle$ and ρ: $\langle\omega_Q^2\rangle = A\rho_t$. The value $A = 0.13\ cm^2\ s^{-2}$ was taken from Baumhoer's work [200], in which the Monte Carlo method was applied to calculate the quadrupole distortion of the shape of the NMR echo signal caused by randomly placed dislocations using linear anisotropic elasticity theory. A much simpler treatment, using isotropic linear elasticity theory, can be given as follows [103]: A is given by eq. (71) as

$$A = 4\pi^2 A_{S,E}^2 \langle f_{S,E}^2\rangle. \tag{156}$$

For isotropic solids

$$A_{S,E}^2\langle f_{S,E}^2\rangle = \left(\frac{3eQ}{\hbar}\frac{1}{4I(2I-1)}\frac{\mu b}{2\pi}C_{11}\right)^2 (a_S\langle f_S^2(\phi)\rangle + a_E\langle f_E^2(\phi)\rangle), \tag{157}$$

where e is the elementary charge, C_{11} the gradient elastic constant connecting the elastic tensor to the electric field gradient tensor, f_S and f_E represent the orientation functions of screw and edge dislocations, respectively, and a_S and a_E denote the corresponding fractions of the two types of dislocations.

These fractions were experimentally determined by Davidge and Pratt [25] and by Hesse [32] as $a_S \simeq 0.2$ and $a_E \simeq 0.8$. The orientation functions are equal to 0.55 and 0.45 for $\langle f_S^2\rangle$ and $\langle f_E^2\rangle$, respectively, with ϕ, the angle between H_0 and the (100) slip plane, equal to $\frac{1}{4}\pi$.

Taking the intermediate value for $C_{11} = 7.5 \times 10^3\ dyn^{-1/2}$ ([103] p. 34), $A_{S,E}^2$ and A can be calculated for NaCl. The value obtained is $A = 0.18\ cm^2\ s^{-2}$, which is in accordance with the value obtained by Baumhoer et al. [200].

Assuming a proportionality between τ and $\rho^{1/2}$ in both stages I and II, fig. 33 yields a value $A \approx 0.07\ cm\ s^{-2}$, which agrees reasonably well with the value obtained by isotropic linear elasticity theory. Hesse and Hobbs [34] also found a proportionality between τ and $\rho^{1/2}$ in both stages of deformation by means of etch-pit measurements on NaCl.

So far, our results and the NMR theory are consistent. A problem appears to arise, however, if account is taken of the observation that the mean distance covered by a moving dislocation at room temperature, $L \sim 1\ \mu m$ in the case of ^{23}NaCl and $\sim 0.1\ \mu m$ in Al, does not vary significantly with strain as concluded from the strain independence of R_D^6. A small decrease due to the increase of $\langle\omega_Q^2\rangle$ with strain is perhaps hidden in the experimental scatter, but is certainly not significant. At lower values of H_1 an increase of $\langle\omega_Q^2\rangle$ should become more prominent, but no such effect could be observed (fig. 31). However, it should be noted that the nuclear relaxation experiment gives the mean

83

distance covered by an activated dislocation segment of unspecified length. Thus we arrive at the interpretation that in the case of NaCl both in stage I and in stage II decreasing lengths of the dislocation lines are activated to move over a more or less constant distance with increasing strain For Al, based on Ashby's analysis (eqs. (6) and (7) [201]), Thompson et al. [202] found the slip distance almost independent of grain size and strain for grain sizes of 20 and 200 μm and for strains larger than about 5%.

Next we will discuss the mean jump distance L determined by NMR in relation to the actual mean slip distance in NaCl and in Al.

Heidemann [27] and Hesse [32] found that during pre-yield slip and dislocation multiplication had taken place on all four slip systems in ^{23}NaCl. After approximately 0.2% of plastic deformation the distance between the dislocations in the slip plane reaches a minimum value of approximately 1.2 μm.

The number of activated planes increases with increasing strain mainly by multiple cross slip out of the original slip planes. Thus broadening slip bands form, which eventually fill the crystal at the end of stage I. The distance between the slip bands is then of the order of the distance between the dislocations in slip planes. The polygon walls formed early in stage II limit the propagation of the activated dislocation segments in the direction of the Burgers vector. The distance between these walls (actual slip distance) 1.2 μm agrees well with the mean jump distance measured by NMR: $L \sim 1$ μm.

Comparing the results from the nuclear relaxation experiments on Al with those obtained from macroscopic strain-sensitivity and work-hardening curves, the fact has to be stressed again that the first method gives the mean distance covered by activated dislocation segments of unspecified lengths, whereas the latter method gives the mean distance covered by an activated dislocation segment which has the same length as this distance if a random distribution of obstacles is assumed. A comparison will be made between our results on the mean free path in Al and those which can be derived directly from stress–strain curves.

It appears that in the early stage of deformation of a polycrystal some hardening occurs of a type similar to the linear hardening observed in single crystals. Stage I hardening represents essentially uninterrupted slip on the primary slip system and would not be expected to be extensive in polycrystalline Al because the grain boundary restraints lead to multiple slip from the very beginning of the stress-strain curve.

On the other hand, the hardening sequence in single crystals seems to be closely paralleled by the hardening curves in polycrystalline materials. Jaoul [203] found that stage I in polycrystalline stress–strain curves is limited to small strains up to 2% elongation. Polycrystalline aluminium at room temperature showed no stage 2 hardening but essentially a parabolic curve. As has been mentioned in sect. 2.2, in single crystals the extent of stage II hardening is related to the ease with which dislocations cross slip to avoid obstacles on their way. Indeed, on deforming Al at 77 K the extension in stage 2 hardening is limited because of the high stacking-fault energy [204]. According to Diehl and Rebstock [205] the mean path L of successively released dislocations decreases during stage II, according to the formula already written down in eq. (5) (assuming that the slip-line length is proportional to the mean slip distance):

$$L = \lambda/(a - a^*), \tag{158}$$

in which a^* is a parameter slightly smaller than a_{II}, the plastic strain at which region II begins. λ is related to L also through the dislocation density ρ and the Burgers vector b [54]:

$$L = (\lambda/\rho b)^{-1/2}. \tag{159}$$

The work-hardening coefficient can be derived as

$$\theta = \alpha\mu(bn/3\lambda)^{1/2}. \tag{160}$$

Here n represents the number of dislocation loops per source and α is a numerical factor of the order of $\simeq 0.06$. Taking θ equal to 5×10^{-3} μ, $n \simeq 25$ [206] in eqs. (159) and (160), and the dislocation density about 10^{11} cm^{-2} [207], L is found to be of the order of 1 μm, i.e. much larger than the mean jump distance measured by NMR ($\simeq 0.1$ μm). This discrepancy will be discussed later. The constant observed rate of work hardening can be understood by assuming that the number of piled-up dislocations per Frank–Read source varies but insignificantly during stage II. Friedel [192] also assumes the obstruction by Lomer–Cottrell barriers to be the main cause of work hardening. In this theory, however, the barriers are supposed all to be formed at the beginning of stage II. Thus the mean free path of dislocations remains invariant, only n increases continuously, in contrast to Seeger's theory.

Stage 3 of the stress–strain curve shows a certain temperature effect in polycrystalline f.c.c. materials. This temperature dependence points to the influence of obstacles that must be passed by the dislocations with the aid of thermal fluctuations. Such obstacles are predominantly Cottrell–Lomer barriers that must be passed either by cross slip or by sheer force (breakthrough). In our experiments on Al the temperature dependence of R_0^0 was found to be insignificant in the range 77 K–293 K, because of the high stacking-fault energy. The by-passing of the barriers by slip on the cross-slip plane which has a common slip direction with the primary slip plane, depends on the stacking-fault energy. A metal like aluminium will soon exhibit stage 3 hardening because the dislocations are narrow and thus cross slip can occur at low applied stresses. The length of the slip lines does not increase in stage 3 as could be expected if the Lomer–Cottrell barriers were collapsed by recombination of the partial dislocations. Seeger [208] has derived an equation for the shear stress τ_3 necessary to cause partial dislocations of the leading dislocation in such a pile-up to coalesce:

$$\tau_3 = \frac{1}{n}\left(\frac{2^{1/2}}{4\pi}\mu - \frac{2\gamma}{b}\right), \tag{161}$$

where γ is the stacking-fault energy and n the number of dislocations in the pile-up. Taking τ_3 from experiments, n is found to be about 25. The size of the pile-up corresponds closely with that which the Seeger theory postulates for the stage 2 hardening model.

Hirsch [77] developed a general theory of stage II hardening considering that piled-up groups of dislocations are formed but that these then relax by secondary slip to

form the observed tangles which are the main obstacles to further slip. New dislocation sources then operate, and when their dislocations pile up near the obstacles they also relax and contribute to the observed tangles. The number of obstacles is in this way directly related to the number of sources. The model has been proved to be compatible with the empirical relation eq. (158).

So far we have not considered the detailed effect of grain size in polycrystalline Al. The mean free path obtained from NMR (0.1 μm) is far less than the grain diameter ($\sim 150\ \mu$m) and the foil thickness (50 μm).

However, even in the early stages of deformation the grain boundaries limit dislocation movement, resulting in an initial parabolic hardening instead of the easy glide of single crystals. A complicating factor is that the stress system even within one grain is very heterogeneous and depends on the behaviour of the adjacent grains. In general these effects are likely to be more important at small grain sizes. Consequently, we expect that our coarse-grained material will approach more closely the behaviour of single crystals [202, 209].

Further, the mean jump distance L measured by NMR in Al has to be interpreted with care in terms of mean slip distance and statistical slip length [Λ_{sl} in eq. (6)]. As commonly found in annealed f.c.c. metals [210], a cell structure is formed in Al after deformation either at room temperature or at 77 K. In both mechanisms mentioned before, the formation of a cell structure involves easy cross slip of large numbers of screw dislocations, i.e. either cross slip of screw dislocations from pile-ups behind Cottrell–Lomer barriers (Seeger) or cross slip from the original slip planes to form relatively strain-free cell walls (Hirsch). Electron micrographs illustrating the cell structure of deformed Al are shown in fig. 45. The cells are relatively free from dislocations but are separated by walls of high dislocation density. The dislocation aggregates in the cell walls are tangles, jogged, twisted and mixed together in an irregular way. The cell diameter ranges in both degrees of deformation from 1 to 2 μm The speed of the mobile dislocation is reduced in the cell wall compared with that outside the cell wall. As a result, the mean slip distance of dislocations is mainly determined by the cell size when the cell structure is well developed. The statistical slip length Λ_{sl} will be of the same order of magnitude as the cell size (~ 1–$2\ \mu$m) [202, 211], i.e. much larger than the mean jump distance measured by NMR ($\sim 0.1\ \mu$m).

A plausible explanation for this difference is that all moving dislocations, both those present in the cell boundary and those in the interior region of the cell, affect the spin–lattice relaxation rate provided that the conditions of sect. 4.1 are fulfilled. The mean jump distance of dislocations measured by NMR is possibly related to the spacing of the dislocation tangles near the cell boundary, ranging from 0.01 to 0.1 μm.

Another explanation for the difference between the jump distance L measured by NMR and the mean slip distance Λ_{sl} is based on a dislocation mechanism in which the dislocation free path Λ_{sl} depends on the mobile dislocation density ρ_m and the number of dislocation intersections N_c in which a dislocation takes part before it gets stuck. This would lead to $\Lambda_{sl} \simeq N_c \rho_m^{-1/2}$. If the dislocations are delayed at each of these intersections during a period of time $\tau_c > 10^{-4}$ s, spin–lattice relaxation takes place (assuming strong collisions, fig. 19). As a result the spin–lattice relaxation rate $T_{1\rho}^{-1}$

86

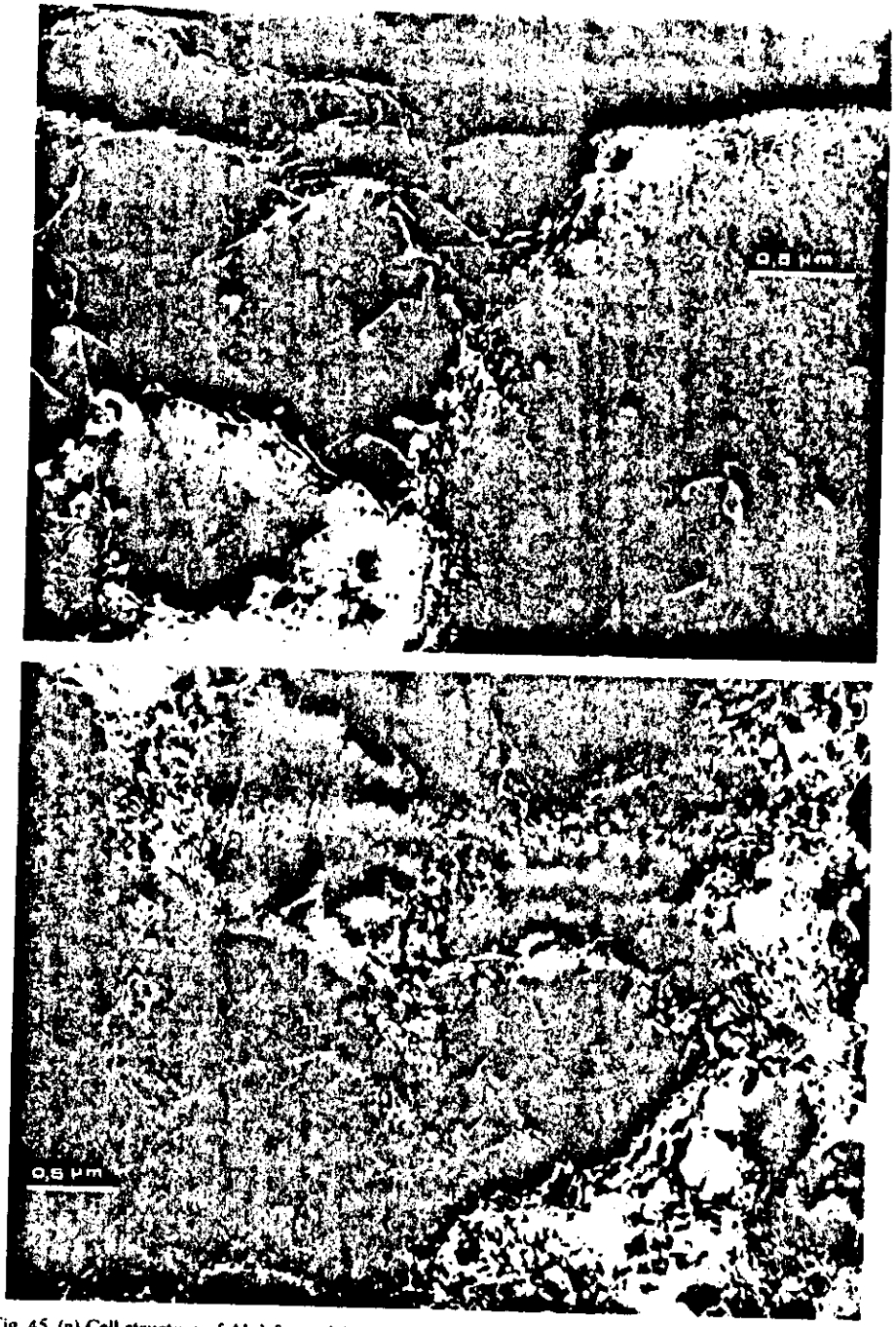

Fig. 45. (a) Cell structure of Al deformed 15% at 77 K. Dark-field strong-beam image, [100] orientation, $g = [002]$, JEM 200 CX [188]. (b) Cell structure of Al deformed 25% at 77 K. Dark-field strong-beam image, [100] orientation, $g = [002]$, JEM 200 CX [188].

87

is determined by the waiting time τ_c at each intersection. The dislocation mean jump distance L thus obtained is much smaller than the actual mean slip distance Λ_{st}. When N_c is about 10 the mean jump distance L measured by NMR would be one order of magnitude smaller than Λ_{st}, as observed. This is according to findings by Verel and Sleeswyk [212]. Further discussion can be found in [188, 213].

At strains larger than 5% (onset of stage 3 hardening, fig. 5) the dislocation cells shrink in size by the subdivision of the largest cells. Such subdivision ceases once the cells have become so small that no new cell walls are being nucleated because chance encounters of glide dislocations have become negligibly frequent [214]. Therefore the shrinking process of the cell pattern cannot go on indefinitely and the cell diameter approaches an asymptotic value of 1–2 μm. It means that for strains larger than $\sim$5% the statistical slip distance Λ_{st} and the mean jump distance L measured by NMR are nearly strain-independent.

In conclusion it may perhaps be said that exploration of NMR effects of moving dislocations has provided valuable information on the intermittent nature of dislocation motion in solids. The method offers much promise for further investigation of the characteristics of dislocation propagation during work hardening under various conditions of strain rate and temperature. Moreover, the NMR technique appears to be an independent and complementary tool to investigate the various theoretical models proposed in the past. In the following section some of our suggestions for new experiments will be presented briefly.

6.4. New experiments

Bearing in mind the results so far obtained, the objective points in the direction of applications of NMR to precipitation hardening in Al alloys. Nuclear magnetic resonance serves as a useful tool for obtaining the Cu concentration in the matrix of Al–Cu alloys in the presence of either coherent or incoherent precipitates. Nakamura et al. [215] determined the change in the copper concentration in the matrix of aluminium–copper alloys during ageing, through which the kinetics of the precipitation sequence of metastable phases is clarified using a curve of resonance intensity versus copper concentration. Studying the quadrupole broadening of NMR lines allows the determination of static dislocation densities in deformed Al. In future we will focus our attention on the *dynamical* aspect of dislocation motion and the mean free paths of moving dislocations in Al alloys such as Al–Cu and Al–Zn. These alloys will be chosen as materials because they can be prepared in different conditions by applying special heat treatments. The NMR study of moving dislocations may answer some questions related to the non-homogeneous plasticity of Al–5wt% Cu. Important parameters in the theory of Ashby [81, 216] for this system are the self-trapping slip distance for dislocations which is equal to the mean slip distance Λ_{st} and the interplate distance Λ_g. If $\Lambda_g < \Lambda_{st}$, hardening is controlled by the microstructure. If, on the other hand, $\Lambda_g > \Lambda_{st}$, cells will be formed, smaller in size than the interplate distance. Harcening is then controlled by the matrix itself. The pulsed nuclear magnetic resonance experiments can make a significant contribution to this field since the dislocation

motion and multiplication are followed during plastic deformation. Already we have performed NMR experiments on Al–1at% Cu containing θ' precipitates [188, 213]. The spin–lattice relaxation $T_{1\rho}$ appears to be sensitive to the microstructure of the alloys. Further experiments need to be carried out in order to obtain more detailed insight into the dislocation dynamics.

Acknowledgements

Discussions with Drs W. Alsem, G. Hut, H. J. Hackelöer and H. Tamler are gratefully acknowledged.

This work is part of the research program of the Foundation for Fundamental Research on Matter (F.O.M.) and has been made possible by financial support from the Netherlands Organization for the Advancement of Pure Research (Z.W.O.–The Hague) and the Deutsche Forschungsgemeinschaft, Fed. Rep. Germany.

References

[1] E. Orowan, Z. Phys. 89 (1934) 634.
[2] M. Polanyi, Z. Phys. 89 (1934) 660.
[3] G. I. Taylor, Proc. Roy. Soc. A145 (1934) 362.
[4] J. M. Hedges and J. W. Mitchell, Phil. Mag. 44 (1953) 223.
[5] J. J. Gilman and W. G. Johnston, in: Dislocations and Mechanical Properties of Crystals (John Wiley, New York, 1957) p. 116.
[6] P. B. Hirsch, R. W. Horne and M. J. Whelan, Phil. Mag. 1 (1956) 677.
[7] W. Bollmann, Phys. Rev. 103 (1956) 1588.
[8] G. D. Watkins, Thesis (Harvard University, 1952).
[9] E. Otsuka and H. Kawamura, J. Phys. Soc. Jap. 12 (1957) 1071.
[10] E. Otsuka, J. Phys. Soc. Jap. 13 (1958) 1155.
[11] E. Otsuka, Y. Oshio, T. Kobayashi and H. Kawamura, J. Phys. Soc. Jap. 14 (1959) 1454.
[12] R. G. Shulman, B. J. Wyluda and P. W. Anderson, Phys. Rev. 107 (1957) 953.
[13] S. Amelinckx, in: Dislocations in Solids, Vol. 2 (F. R. N. Nabarro, ed.) (North-Holland, Amsterdam, 1979) p. 379.
[14] M. T. Sprackling, The Plastic Deformation of Simple Ionic Crystals (Academic Press, London, 1976).
[15] J. J. Gilman, Acta Met. 7 (1959) 608.
[16] H. B. Huntington, J. E. Dickey and R. Thomson, Phys. Rev. 100 (1955) 1117.
[17] H. B. Huntington, J. E. Dickey and R. Thomson, Phys. Rev. 113 (1959) 1696.
[18] T. Kurosawa, J. Appl. Phys. 33, Suppl. 1 (1962) 320.
[19] M. P. Puls and C. B. So, Phys. Stat. Sol. (b)98 (1980) 87.
[20] F. Granzer, G. Wagner and J. Eisenblätter, Phys. Stat. Sol. 30 (1968) 587.
[21] F. Granzer, V. Belzner, M. B. Bücher, P. Petrasch and C. Teodosiu, J. de Physique, Suppl. 11, 34 (1973) C9-359.
[22] V. Belzner and F. Granzer, Phys. Stat. Sol. (a)39 (1977) 183.
[23] D. Kuhlmann-Wilsdorf, Trans. Met. Soc. AIME 224 (1962) 1047.
[24] P. L. Pratt, Acta Met. 1 (1953) 103.
[25] R. W. Davidge and P. L. Pratt, Phys. Stat. Sol. 6 (1964) 759.
[26] S. J. Mendelson, J. Appl. Phys. 33 (1962) 2175.
[27] K. F. Heidemann, Thesis (University of Münster, 1973).

[28] M. P. Shaskol'skaya and Sun Jui-fang, Sov. Phys. Cryst. 4 (1960) 68.
[29] W. G. Johnston and J. J. Gilman, J. Appl. Phys. 31 (1960) 632.
[30] T. V. Samoilova, B. I. Smiznov and E. E. Chernov, Phys. Stat. Sol. 28 (1968) K1.
[31] J. Hesse and K. H. Matucha, Scripta Met. 6 (1972) 865.
[32] J. Hesse, Phys. Stat. Sol. 9 (1965) 209.
[33] A. S. Argon, A. G. Nigam and G. E. Padawer, Phil. Mag. 25 (1972) 1095.
[34] J. Hesse and L. W. Hobbs, Phys. Stat. Sol. (a)14 (1972) 599.
[35] B. H. Kear, C. E. Silverstone and P. L. Pratt, Proc. Brit. Ceram. Soc. 6 (1966) 269.
[36] W. Franzbecker, Phys. Stat. Sol. (b)57 (1973) 545.
[37] H. Strecker and H. Strunk, in: Proc. Vth Int. Conf. High-Voltage Electron Microscopy, Kyoto, 1977 (H. Hashimoto and T. Imura, eds.) J. Electron Microscopy 26 (1977) 645.
[38] E. Yu. Gutmanas and E. M. Nadgornyi, Phys. Stat. Sol. 33 (1970) 777.
[39] O. V. Klyavin, S. G. Shimashko and A. V. Stepanov, Sov. Phys. Sol. St. 15 (1973) 247.
[40] O. V. Klyavin and S. G. Shimashko, Sov. Phys. Sol. St. 16 (1974) 893.
[41] K. H. Matucha, Phys. Stat. Sol. 26 (1968) 291.
[42] P. Haasen, J. de Physique 34 (1973) C9-205.
[43] W. Frank, Mat. Sci. Eng. 6 (1970) 121.
[44] W. Frank, Mat. Sci. Eng. 6 (1970) 132.
[45] J. Washburn, in: Electron Microscopy and Strength of Crystals (G. Thomas and J. Washburn, eds.) (Interscience, New York, 1963) p. 301.
[46] W. Schmitten and P. Haasen, J. Appl. Phys. 32 (1961) 1790.
[47] J. Deputat and Z. Pawlowski, Bull. Acad. Polon. Sci., Ser. Sci. Tech. 41 (1966) 419.
[48] W. G. Johnston and J. J. Gilman, J. Appl. Phys. 30 (1959) 129.
[49] U. Essmann, Phys. Stat. Sol. 17 (1966) 725.
[50] A. Seeger, H. Kronmüller, S. Mader and H. Träuble, Phil. Mag. 6 (1961) 639.
[51] B. Reppich, Phys. Stat. Sol. 35 (1969) 339.
[52] K. H. Matucha, W. Franzbecker and M. Wilkens, Phys. Stat. Sol. 33 (1969) 493.
[53] M. Wilkens and M. O. Bargouth, Acta Met. 16 (1968) 465.
[54] W. Frank and A. Seeger, Comm. Sol. St. Phys. 11 (1969) 133.
[55] I. V. K. Bhagavan Raju and H. Strunk, Phys. Stat. Sol. (a)53 (1979) 211.
[56] A. G. Evans and P. L. Pratt, Phil. Mag. 21 (1970) 951.
[57] A. S. Argon and G. E. Padawer, Phil. Mag. 25 (1972) 1073.
[58] R. Frydman and H. Strunk, Scripta Met. 7 (1973) 471.
[59] A. S. Argon, in: Physics of Strength and Plasticity (A. S. Argon, ed.) (M.I.T. Press, Cambridge, Mass., 1969) p. 217.
[60] A. S. Argon and G. East, in: Proc. Int. Conf. on the Strength of Metals and Alloys, Trans. Jap. Inst. Met. 9 (1968) 756.
[61] A. H. Cottrell, Phil. Mag. 43 (1952) 645.
[62] W. M. Lomer, Phil. Mag. 42 (1951) 1327.
[63] E. Schmid and W. Boas, Kristallplastizität (Springer, Berlin, 1935) p. 55.
[64] J. W. Steeds and P. M. Hazzledine, Disc. Faraday Soc. 38 (1964) 103.
[65] H. P. Karnthaler, Phil. Mag. 38 (1968) 141.
[66] H. P. Karnthaler and A. Korner, in: Proc. 5th Int. Conf. Strength of Metals and Alloys, Aachen 1979 (Pergamon, New York, 1979) p. 35.
[67] P. Lacombe and L. Beaujard, J. Inst. Metals 74 (1948) 1.
[68] A. N. Stroh, Phil. Mag. 1 (1956) 489.
[69] H. Mughrabi, Phil. Mag. 23 (1971) 897.
[70] R. Rodloff and H. Neuhäuser, Phys. Stat. Sol. (a)49 (1978) 445.
[71] S. Mader, Z. Phys. 149 (1957) 73.
[72] H. Mughrabi, Phil. Mag. 23 (1971) 869.
[73] U. Essmann, Phys. Stat. Sol. 3 (1963) 932.
[74] U. Essmann, Phys. Stat. Sol. 12 (1965) 707, 723.
[75] Z. S. Basinski, Disc. Faraday Soc. 38 (1964) 93.

[76] S. J. Basinski and Z. S. Basinski, in: Dislocations in Solids, Vol. 4 (F. R. N. Nabarro, ed.) (North-Holland, Amsterdam, 1979) p. 321.
[77] P. B. Hirsch, in: The Physics of Metals, Vol. 2 (P. B. Hirsch, ed.) (Cambridge University Press, 1975) p. 189.
[78] H. Mughrabi, in: Constitutive Equations in Plasticity (A. S. Argon, ed.) (M.I.T. Press, Cambridge Mass., 1975) p. 199.
[79] A. S. Argon and G. H. East, in: Proc. 5th Int. Conf. Strength of Metals and Alloys, Aachen 1979 (Pergamon, New York, 1979) p. 9.
[80] F. R. N. Nabarro, Z. S. Basinski and D. B. Holt, Adv. Phys. 13 (1964) 193.
[81] M. F. Ashby, Phil. Mag. 21 (1970) 399.
[82] H. Mecking, in: Proc. 5th Int. Conf. Strength of Metals and Alloys, Aachen 1979 (Pergamon, New York, 1979) p. 1573.
[83] H. Mecking, in: Work Hardening in Tension and Fatigue (A. W. Thompson, ed.) (AIME, 1977) p. 67.
[84] G. Hut, A. W. Sleeswyk, H. J. Hackelöer, H. Selbach and O. Kanert, Phys. Rev. B14 (1976) 921.
[85] U. F. Kocks and H. Mecking, AIME meeting Pittsburgh (1974) (Abstr. book).
[86] J. T. Fourie, Can. J. Phys. 45 (1967) 777.
[87] U. Valdrè and P. B. Hirsch, Phil. Mag. 8 (1963) 237.
[88] P. C. J. Gallagher, Metall. Trans. 1 (1970) 2429 and refs. therein.
[89] A. Abragam, Nuclear Magnetism (Oxford University Press, 1962) p. 159ff.
[90] C. P. Slichter, Principles of Magnetic Resonance (Harper and Row, New York, 1964) p. 160ff.
[91] H. Silescu, Kernmagnetische Resonanz (Springer Verlag, Berlin, 1966) p. 69ff.
[92] G. M. Volkoff, Can. J. Phys. 31 (1953) 820.
[93] G. M. Volkoff, H. E. Petch and D. W. L. Smellie, Can. J. Phys. 30 (1952) 270.
[94] V. V. Lemanov, Sov. Phys. JETP 13 (1961) 543.
[95] D. F. Bolef, in: Physical Acoustics, Vol. IVA (Academic, New York, 1966) p. 113ff.
[96] T. Kanashiro, T. Ohno and N. Satoh, J. Phys. Soc. Jap. 38 (1975) 1233.
[97] J. D. Eshelby, W. T. Read and W. Shockley, Acta Met. 1 (1953) 251.
[98] J. W. Steeds, Introduction to Anisotropic Elasticity Theory of Dislocations (Clarendon, Oxford, 1973) p. 15.
[99] A. Seeger and G. Schöck, Acta Met. 1 (1953) 520.
[100] J. P. Hirth and J. Lothe, Theory of Dislocations (McGraw Hill, New York, 1968) p. 424.
[101] J. Th. M. De Hosson, Atomic Configurations and Electronic Structures of Edge Dislocations (Ann Arbor, Mich., 1976) order no. 21.057, p. 5.
[102] A. H. Cottrell, Theory of Crystal Dislocations (Blackie and Son, London, 1964) p. 34ff.
[103] O. Kanert and M. Mehring, Static Quadrupole Effects in Disordered Cubic Solids, NMR, Vol. 3 (Springer Verlag, Berlin, 1971) p. 3.
[104] R. A. Brown, Phys. Rev. 141 (1966) 568.
[105] T. O. Ogurtani and R. A. Huggins, Phys. Rev. 137A (1965) 1736.
[106] O. Kanert, Phys. Stat. Sol. 32 (1969) 667.
[107] W. H. M. Alsem, Dislocation Motion in NaCl Single Crystals Investigated by Means of Nuclear Spin Relaxation, Thesis (Groningen, 1981).
[108] M. H. Cohen and F. Reif, Solid State Physics 5 (1957) 321.
[109] B. A. Greenberg, Phys. Stat. Sol. 17 (1966) 673.
[110] K. Preusser, Diploma work (Münster, 1966).
[111] Y. T. Chou, J. Appl. Phys. 34 (1963) 429.
[112] J. C. M. Li, Acta Met. 8 (1960) 296.
[113] W. Raupach, Phys. Stat. Sol. (a)58 (1980) 435.
[114] J. Butterworth, Proc. Phys. Soc. London 86 (1965) 297.
[115] F. Solomon, Phys. Rev. 110 (1958) 61.
[116] A. Flett and J. Richards, Proc. Phys. Soc. London 86 (1965) 171.
[117] H. Abe, H. Yasuoka and A. Hirai, J. Phys. Soc. Jap. 21 (1966) 77.
[118] G. Bonera and M. Galimberti, Ist. Lombardo Sci. Lettre A100 (1966) 617.
[119] I. S. Donskaya and A. R. Kessel, Sov. Phys. Sol. St. 10 (1968) 694.

[120] I. D. Weisman and L. H. Bennett, Phys. Rev. 181 (1969) 1341.
[121] M. Mehring and O. Kanert, Z. Naturforsch. 24a (1969) 768.
[122] M. Engelberg and I. J. Lowe, Phys. Rev. B10 (1974) 822.
[123] B. T. Gravely and J. D. Memory, Phys. Rev. B3 (1971) 3426.
[124] J. H. Van Vleck, Phys. Rev. 74 (1948) 1168.
[125] O. Kanert, D. Kotzur and M. Mehring, Sol. St. Commun. 13 (1973) 1017.
[126] V. L. Bogdanov and V. V. Lemanov, Sov. Phys. Sol. St. 9 (1967) 357.
[127] A. M. Stoneham, Rev. Mod. Phys. 41 (1969) 82.
[128] J. L. Mash and P. A. Casabella, Phys. Rev. 150 (1968) 546.
[129] M. Hanabasa and T. Yamaguchi, J. Phys. Soc. Jap. 26 (1969) 901.
[130] H. Alloul and C. Froideveaux, J. Phys. Chem. Sol. 29 (1968) 623.
[131] D. Kotzur, Diploma work (Münster, 1968).
[132] S. Grande, V. A. Shutilov and L. N. Sershtat, Phys. Stat. Sol. (b)53 (1972) 127.
[133] H. J. Hackelöer and O. Kanert, Z. Naturforsch. 27a (1972) 1235.
[134] H. J. Hackelöer and O. Kanert, J. Mag. Res. 17 (1975) 367.
[135] O. Kanert and K. Preusser, Sol. St. Commun. 15 (1974) 97.
[136] O. Kanert, D. Kotzur and M. Mehring, Phys. Stat. Sol. 36 (1969) 291.
[137] R. K. Sundfors, T. H. Wang, D. I. Bolef, P. A. Fedders and D. G. Westlake, Phys. Rev. B12 (1975) 26.
[138] J. Pellison and J. Buttet, Phys. Rev. B11 (1975) 48.
[139] F. Fischer, V. Müller, D. Ploumbidis and G. Schanz, Phys. Rev. Lett. 40 (1978) 796.
[140] D. Wolf, Spin Temperature and Nuclear Relaxation in Matter (Clarendon, Oxford, 1979).
[141] M. Goldmann, Spin Temperature and Nuclear Magnetic Resonance in Solids (Clarendon, Oxford, 1970).
[142] N. Bloembergen, E. M. Purcell and R. V. Pound, Phys. Rev. 73 (1948) 679.
[143] A. G. Redfield, Phys. Rev. 98 (1955) 1787.
[144] A. J. Anderson and S. R. Hartmann, Phys. Rev. 128 (1962) 2023.
[145] G. Hut, Thesis (University of Groningen, 1976).
[146] D. Wolf and O. Kanert, Phys. Rev. B16 (1977) 4776.
[147] D. A. McArthur, E. L. Hahn and R. E. Walstedt, Phys. Rev. 188 (1969) 609.
[148] D. Demco, J. Tegenfeldt and J. S. Waugh, Phys. Rev. B11 (1975) 4133.
[149] T. J. Rowland and F. Y. Fradin, Phys. Rev. 182 (1969) 760.
[150] H. C. Torrey, Phys. Rev. 92 (1953) 962.
[151] D. Wolf, J. Mag. Res. 19 (1975) 1.
[152] A. G. Evans and R. D. Rawlings, Phys. Stat. Sol. 34 (1969) 9.
[153] H. J. Hackelöer, H. Selbach, O. Kanert, A. W. Sleeswyk and G. Hut, Phys. Stat. Sol. (b)80 (1977) 235.
[154] F. Appel, H. Bethge and U. Messerschmidt, Phys. Stat. Sol. (a)38 (1976) 103.
[155] H. Neuhäuser and G. Schulz, Phys. Stat. Sol. (a)45 (1978) 89.
[156] J. Jeener and P. Broekaert, Phys. Rev. 157 (1967) 232.
[157] G. Hut, A. W. Sleeswyk, H. J. Hackelöer, H. Selbach and O. Kanert, Sol. St. Commun. 15 (1974) 1115.
[158] J. S. Waugh, Advances in Magnetic Resonance 5 (1971) 147 (Academic, New York, 1971) 147.
[159] G. Hut, H. J. Hackelöer, H. Selbach, O. Kanert and A. W. Sleeswyk, in: 18th Ampère Congr. (North-Holland, Amsterdam, 1974) p. 233.
[160] G. Hut, A. W. Sleeswyk, H. J. Hackelöer, H. Selbach and O. Kanert, Sol. St. Commun. 17 (1975) 85.
[161] C. P. Slichter and D. C. Ailion, Phys. Rev. 135A (1964) 1099.
[162] D. C. Ailion, Advances in Magnetic Resonance 5 (1971) 177.
[163] D. Wolf, Phys. Rev. B14 (1976) 932.
[164] L. C. Hebel, Sol. St. Phys. 15 (1963) 457.
[165] W. H. M. Alsem, J. Th. M. De Hosson, H. Tamler, H. J. Hackelöer and O. Kanert, Recent Developments in Condensed Matter Physics, Vol. 3 (J. Devreese, ed.) (Plenum, New York, 1980) p. 113.
[166] W. H. M. Alsem, J. Th. M. De Hosson, H. Tamler and O. Kanert, Phil. Mag. 46 (1982) 451.
[167] W. H. M. Alsem, J. Th. M. De Hosson, H. Tamler and O. Kanert, Phil. Mag. 46 (1982) 469.
[168] R. B. Schwarz and R. Labusch, J. Appl. Phys. 49 (1978) 5174.
[169] G. Berg, F. Fröhlich and S. Siebenhühner, Phys. Stat. Sol. (a)31 (1975) 385.

[170] W. H. M. Alsem, J. Th. M. De Hosson, H. J. Tamler, H. J. Hackelöer and O. Kanert, in: Nuclear and Electron Resonance Spectroscopies applied to Materials Science (E. N. Kaufmann and G. K. Shenoy, eds.) (North-Holland, Amsterdam, 1981) p. 481.
[171] R. B. Schwarz, Phys. Rev. B21 (1980) 5617.
[172] W. H. M. Alsem, J. Th. M. De Hosson, H. Tamler, H. J. Hackelöer and O. Kanert, in: Proc. Joint Conf. ISMAR-Ampère, Delft, Bull. Magnetic Resonance, 1980, p. 262.
[173] D. Klahn, A. K. Mukherjee and J. E. Dorn, in: Proc. 2nd Int. Conf. Strength of Metals and Alloys (Am. Soc. for Metals, 1970) p. 951.
[174] R. W. Dreyfus and A. S. Nowick, Phys. Rev. 126 (1962) 1367.
[175] Y. Haven, in: [1954] Conf. Defects in Crystalline Solids (Phys. Soc., London, 1955) p. 261.
[176] H. Etzel and R. Maurer, J. Chem. Phys. 18 (1950) 1003.
[177] J. H. Crawford, J. Phys. Chem. Sol. 31 (1970) 399.
[178] J. S. Dryden, J. Phys. Soc. Jap., Suppl. III 18 (1965) 129.
[179] M. Dubiel, G. Berg and F. Fröhlich, Phys. Stat. Sol. (b)89 (1978) 595.
[180] J. Snoek, Physica 8 (1941) 711.
[181] F. Fröhlich, P. Grau and B. Zigan, Crystal Lattice Defects 5 (1974) 215.
[182] W. Frank, Z. Naturforsch. 22a (1967) 377.
[183] A. S. Argon, Phil. Mag. 25 (1972) 1053.
[184] H. J. Hackelöer, Thesis (Dortmund, 1976).
[185] H. Tamler, H. J. Hackelöer, O. Kanert, W. H. M. Alsem and J. Th. M. De Hosson, in: Nuclear and Electron Resonance Spectroscopies applied to Materials Science (E. N. Kaufmann and G. K. Shenoy, eds.) (North-Holland, Amsterdam, 1981) p. 421.
[186] P. Haasen, Physikalische Metallkunde (Springer-Verlag, Berlin, 1974) p. 280.
[187] K. Preusser, Thesis (University of Münster, 1972).
[188] H. Tamler, O. Kanert, W. H. M. Alsem and J. Th. M. De Hosson, Acta Met. 30 (1982) 1523.
[189] A. Seeger, in: [1954] Defects in Crystalline Solids (Phys. Soc., London, 1955) p. 391.
[190] A. H. Cottrell and R. J. Stokes, Proc. Roy. Soc. A233 (1955) 17.
[191] J. Eisenblätter, Phys. Stat. Sol. 31 (1969) 71.
[192] J. Friedel, Dislocations (Pergamon, New York, 1964).
[193] A. Seeger, Z. Naturforsch. 9a (1954) 870.
[194] G. Saada, Thesis (Paris, 1960).
[195] H. G. van Bueren, Acta Met. 3 (1957) 519.
[196] H. G. van Bueren, Philips Research Reports 12 (1955) 1.
[197] L. W. Barr and A. B. Lidiard, Phys. Chem. An Adv. Treatise, Vol. 10 (Academic, New York, 1970) chap. 3.
[198] R. W. Balluffi, J. Nucl. Mat. 69 (1978) 240.
[199] P. R. Moran and D. V. Lang, Phys. Rev. B2 (1970) 2360.
[200] W. Baumhoer, J. Thieman and O. Kanert, Phys. Stat. Sol. (b)73 (1976) 155.
[201] M. F. Ashby, in: Strengthening Methods in Crystals (A. Kelly and R. B. Nicholson, eds.) (Appl. Sci. Publ., London, 1971) p. 137.
[202] A. W. Thompson, M. I. Baskes and W. F. Flanagan, Acta Met. 21 (1973) 1017.
[203] B. Jaoul, J. Mech. Phys. Sol. 5 (1957) 95.
[204] R. W. K. Honeycombe, The Plastic Deformation of Metals (Edward Arnold, London, 1968) p. 129.
[205] J. Diehl and H. Rebstock, Z. Naturforsch. 11a (1956) 169.
[206] H. G. van Bueren, Imperfections in Crystals (North-Holland, Amsterdam, 1961) pp. 170–176.
[207] L. F. Mondolfo, Aluminium Alloys (Butterworths, London, 1979) p. 38.
[208] A. Seeger, in: Dislocations and Mechanical Properties of Crystals (J. C. Fisher, W. G. Johnston, R. Thomson and T. Vreeland, eds.) (John Wiley, New York, 1957) p. 243.
[209] N. Hansen, Acta Met. 25 (1977) 863.
[210] P. R. Swann, in: Electron Microscopy and Strength of Crystals (G. Thomas and J. Washburn, eds.) (Wiley, New York, 1963) p. 131.
[211] H. Fujita and T. Tabata, Acta Met. 21 (1973) 355.
[212] D. J. Verel and A. W. Sleeswyk, Acta Met. 21 (1973) 1087.

[213] H. Tamler, O. Kanert and J. Th. M. De Hosson, in: Strength of Metals and Alloys (R. C. Gifkins, ed.) (Pergamon Press, New York, 1982) p. 101.
[214] D. Kuhlmann-Wilsdorf, in: Work Hardening in Tension and Fatigue (A. W. Thompson, ed.) (AIME, 1977) p. 1.
[215] F. Nakamura, K. Furakawa, T. Ebine and J. Takamura, Phil. Mag. 41 (1980) 307.
[216] K. C. Russell and M. F. Ashby, Acta Met. 18 (1970) 891.
[217] H. J. Hackelöer, O. Kanert, H. Tamler and J. Th. M. De Hosson. Rev. Sci. Instrum. 54(3) (1983).
[218] W. H. M. Alsem and J. Th. M. De Hosson, Phil. Mag. 46 (1982) 327.